INFORMATION TO USERS

The most advanced technology has been used to photograph and reproduce this manuscript from the microfilm master. UMI films the text directly from the original or copy submitted. Thus, some thesis and dissertation copies are in typewriter face, while others may be from any type of computer printer.

The quality of this reproduction is dependent upon the quality of the copy submitted. Broken or indistinct print, colored or poor quality illustrations and photographs, print bleedthrough, substandard margins, and improper alignment can adversely affect reproduction.

In the unlikely event that the author did not send UMI a complete manuscript and there are missing pages, these will be noted. Also, if unauthorized copyright material had to be removed, a note will indicate the deletion.

Oversize materials (e.g., maps, drawings, charts) are reproduced by sectioning the original, beginning at the upper left-hand corner and continuing from left to right in equal sections with small overlaps. Each original is also photographed in one exposure and is included in reduced form at the back of the book. These are also available as one exposure on a standard 35mm slide or as a 17" x 23" black and white photographic print for an additional charge.

Photographs included in the original manuscript have been reproduced xerographically in this copy. Higher quality 6" x 9" black and white photographic prints are available for any photographs or illustrations appearing in this copy for an additional charge. Contact UMI directly to order.

U·M·I

University Microfilms International
A Bell & Howell Information Company
300 North Zeeb Road, Ann Arbor, MI 48106-1346 USA
313/761-4700 800/521-0600

Order Number 8915587

# Picosecond time resolved Raman induced phase conjugation in crystals

Delfyett, Peter John, Jr., Ph.D.

City University of New York, 1988

U·M·I
300 N. Zeeb Rd.
Ann Arbor, MI 48106

# PICOSECOND TIME RESOLVED
# RAMAN INDUCED PHASE CONJUGATION
# IN
# CRYSTALS

by

PETER J. DELFYETT, Jr.

A dissertation submitted to the Graduate Faculty in Engineering in partial fulfillment of the requirements for the degree of Doctor of Philosophy, The City University of New York.

1988

This manuscript has been read and accepted for the Graduate Faculty in Engineering in satisfaction of the dissertation requirement for the degree of Doctor of Philosophy.

9-8-88 Robert R Alfano

Date Chair of Examining Committee

9-8-88 Roger Dorsinville

Date Co-Chair of Examining Committee

9/8/88 Jacques E. Benveniste

Date Executive Officer

Samir Ahmed

Yao Li

Anthony M Johnson

Supervisory Committee

The City University of New York

## Abstract

# PICOSECOND TIME RESOLVED
# RAMAN INDUCED PHASE CONJUGATION
# IN
# CRYSTALS

by

Peter J. Delfyett, Jr.

Advisor: Professor Robert R. Alfano

In this thesis, picosecond laser pulses are used to study the spectral and temporal properties of optical phonons in crystals using Raman Induced Phase-Conjugation Spectroscopy (RIPS). The concepts of RIPS are illustrated using a dynamical grating analysis. A theoretical description of the spectral properties of RIPS relying on the third order nonlinear susceptibility is worked out in detail for $LiNbO_3$. Optical phonon lifetimes are measured directly in real time using a new technique called STRIPS, which uses RIPS in conjunction with streak camera technology. This new technique is used to obtain information about the temperature dependence of phonon-phonon interactions of the 1086 $cm^{-1}$ mode in calcite. Future directions for the use of RIPS in other areas of physics and photonics are suggested.

# ACKNOWLEDGEMENTS

I would like to acknowledge Prof. Robert Alfano for allowing me to have the opportunity to pursue research in ultrafast nonlinear optics. He has constantly provided me with advice and taught me how to "focus and dig in" on a particular problem. I especially wish to thank Prof. Roger Dorsinville, with whom I have worked most closely, for the immediate and never ending guidance he provided throughout my stay at the IUSL.

I wish to mention my family, especially my father and grandparents, who were always supportive of my academic goals throughout my life.

## Table of Contents

## LIST OF ILLUSTRATIONS

# CHAPTER 1

# HISTORICAL BACKGROUND OF OPTICAL PHASE CONJUGATION

## [1.1] Introduction

Over one hundred years ago, communications and information transmission originally relied on mechanical means, such as smoke signals, beating drums, reflecting light from smooth surfaces, etc.. Since that time, communications has progressed into the field of electronics. Now the new era of photonics is on the horizon and it appears that this will be the new standard for a multitude of applications spanning communications, computers, and medical analysis. Today, there is a tremendous demand for having devices which can perform complex procedures, quickly and efficiently. The field of electronics has been able to produce systems based on sophisticated circuitry, which can perform over a billion instructions per second. Technological limits are rapidly approaching in the current state of the art electronics. To circumvent this, photon technology is being developed to assist in the task of transmitting and processing the vast amounts of information. Since the development of the laser, the field of optics has blossomed into the new field of photonics.

The best way to define photonics is to use a simple analogy: Photonics is to photons as electronics is to electrons. Thus photonics will use light to create devices which will transmit and process information in the same way that electricity is used in the electronics industry. These new photonic devics will make use of the fundamental properties of light to develop faster and more efficient systems than the electronic conterparts.

With the laser, the fundamental limits which were encountered with electronics are greatly reduced. The speed of operation of devices is increased because of the increased speed of light as compared to electrons. Less heat generation and power loss are also characteristic of optical devices, which ultimately leads to smaller and more efficient systems. Most important, the bandwidth of photonic devices greatly exceeds electronics, which increases the data transmission capacity.

The most fascinating area of optics lies in the fact that man lives in an optically oriented society. Devices which can receive optical information as input, such as an image to produce an output image without the usual electronic conversion would be highly desirable.

The two main constitiuents which will ultimately be at the heart of any photonic processing system will include light sources with excellent spectral, temporal, and spatial characteristics, and materials which can support ultrafast physical processes.

State of the art optical processing systems, which have been developed for image reconstruction, image transmission, pattern recognition, optical computation, and correcting optical abberations, rely on holographic tehniques. Unfortunately, any system based on present day holographic techniques will have limited applications because of the difficulty of performing a real time holographic record-and-read-out operation. The need for a holographic process which can record, process, and read out information in real time, would be the photonic panacea. New nonlinear optical techniques, using degenerate four wave mixing and Optical Phase Conjugation can accomplish the task of performing the holographic record-and-read-out process in real time.

Optical phase conjugation has become an increasingly important topic in the study of photonics because of its tremendous potential in diverse applications ranging from real time adaptive optics, image processing, optical computing and nonlinear laser spectroscopy [1]. Semiconductors, dielectrics and polymers have become the material of choice in optical phase conjugate processes and devices because of their large nonlinearity. In order to exploit the phase conjugate process to its fullest potential and obtain optimal performance of the new photonic devices, knowledge of the underlying ultrafast phenomena must be obtained. Fundamental information regarding the limits of the size and speed of the optical phase conjugate process must be obtained before a focused effort in creating photonic devices can be undertaken. Probing the dynamics of the phase conjugate process using picosecond light pulses is important to perfect the future generation devices.

Historically, the first experimental observations involving phase conjugation were performed in Russia by Zel'dovich et. al.[2]. Since that time, the field of optical phase conjugation has been expanding at a tremendous rate, with a number of researchers in the U.S. dominating the field. Their investigations include a wide variety of phenomena ranging from molecular reorientation, absorption and refractive index changes, free and bound electron dynamics, impurity dynamics, photorefraction, and phonon dynamics.

It is only recently that the connection between generating conjugate waves and nonlinear wave mixing has been made. Over twenty years ago, one of the first pioneers to use picosecond nonlinear wave mixing techniques to directly probe matter on a picosecond time scale were Alfano and Shapiro [3]. They were the first to make a direct measurement of the optical phonon lifetime in calcite, using time resolved Raman scattering and the new picosecond continuum source which they had discovered.

Some of the limitations and experimental difficulties which were encountered in the earlier time resolved nonlinear spectroscopic techniques are the phase matching conditions which dictate the optical geometry, input frequencies, and conversion efficiencies, and the need to have an ultrafast high power, high repetion rate laser for data collection and averaging to obtain the temporal evolution of the photogenerated excitations. In addition, several input frequencies are needed to tune to a desired resonance. A system which relaxes the above experimental limitations would be highly desirable.

## [1.2] Thesis Statement

The objective of my thesis is to use picosecond time resolved phase conjugation as a spectroscopic tool to study the dynamics of photogenerated optical phonons in wide band gap crystals. The work will be divided into two parts:

[1] Raman induced phase conjugation is used with picosecond laser pulses and a broadband continuum pulse to generate complete Raman spectra in wide bandgap dielectrics [4]. The Raman spectra is phase matched over the bandwidth of the continuum, typically 2000 $cm^{-1}$. Selection rules and shape analysis of the Raman Induced Phase Conjugate scattered spectrum will be performed in $LiNbO_3$. The potential of this technique to be used as a pump probe spectroscopic tool is investigated.

[2] The optical phonon dynamics in calcite is investigated using a new technique which I have developed. The dephasing dynamics is measured as a function of temperature to understand how temperature can effect the dephasing mechanisms of optical phonons. The measured dephasing lifetimes are compared to the theory and measured linewidths [3,5,6,7].

The information obtained from this thesis is important to high speed device operation because the decay dynamics give us basic fundamental information about the energy dissapation mechanisms in matter. The knowledge gained from this thesis may also lead to devices operating on the principles of ultrafast photogenerated excitations and their decay dynamics.

## [1.3] Outline of Thesis

The body of the thesis is be divided into eight main chapters.

The first two chapters introduce the subject of optical phase conjugation and what importance it has in the photonic field. The goals of the thesis are stated and the general experimental techniques which were employed are also described.

The third chapter describes the optical phase conjugate process for degenerate four wave mixing and extends the ideas to nondegenerate four wave mixing and RIPS. These four wave mixing techniques are described in terms of a grating analysis. The potential for using RIPS as a pump-probe tool to investigate the dynamics of the gratings will be discussed. Connections between the derived grating parameters for RIPS and the parameters of the physical excitation, e.g., phonons, are made.

The fourth chapter discusses the spectral properties of RIPS using a theory based on the nonlinear third order susceptibility. This is carried out in detail for the molecular crystal lithium niobate.

The fifth chapter focuses on the white light continuum generation process. Since the RIPS technique uses the white light continuum as one of the pumping pulses, it becomes imperative to know both the temporal and spectral properties of this light source. The chapter discusses both the temporal and spectral properties of the continuun which has been generated from a 5 cm. cell of $D_2O$, using a 30 psec. laser pulse at 532 nm.

The sixth chapter is devoted to describing a new real time technique which measures the molecular vibrational and optical phonon dephasing times, with a single laser pulse. This technique relies on RIPS, which is discussed in Chapter Two and Three, and a pulse shortening effect which occurs in the continuum generation process, which is discussed in Chapter Four. This chapter will focus on testing the technique by measuring the dephasing time of a known substance, such as liquid $CS_2$ [8], and determining the systems temporal limits and its resolution. In addition, a comparison is made between the real time results obtained using the new RIPS technique, with the results one obtains when RIPS is used as a pump-probe tool.

In Chapter Seven, the new real time technique is used to study the optical phonon dephasing of the 1086 $cm^{-1}$ mode in calcite as a function of temperture. Several models using three and four phonon anharmonic interactions are proposed and tested, to determine the relaxation mechanisms, and their relative strengths.

In the eighth chapter, potential applications and future directions are suggested.

## Notes

[1] Fisher, R., Optical Phase Conjugation, Academic Press, N.Y., (1983)

[2] Zel'dovich,B.Y., Popovich,V.I., Ragul'skii,V.V.,and Faizullov, Sov. Phys. JETP, (15), 109, (1972)

[3] Alfano,R.R.,and Shapiro,S.L., Phys. Rev. Lett. (26), 1247, (1971)

[4] Saha,S.K., and Hellwarth,R.W., Phys. Rev. A, (27), 919,

[5] Laubereau,A., Wochner,G., and Kaiser,W., Opt.Comm. (14), 75, (1975)

[6] Lee,C.H., and Ricard,D., Appl. Phys. Lett., (32), 168, (1978)

[7] Park,K., Phys. Rev. Lett. A, (25), 490, (1967) (1983)

[8] Heritage,J.P., Appl. Phys. Lett., (34), 470, (1979)

# CHAPTER 2

# EXPERIMENTAL METHODS

## [2.1] Introduction

In this section, the main equipment which has been used in the experimental parts of thesis is described. The major components are 1) an active-passive mode locked Nd:YAG laser for producing picosecond optical pulses, 2) an optical multichannel analyzer in conjunction with a 1 meter spectrometer, and 3) a streak camera with a temporal resolution of 2 psec. Additional standard support equipment was available, such as photodiodes, photomultipliers, a boxcar averager, and a fast oscilloscope ~250 psec resolution.

## [2.2] The Laser

The laser source which provided all of the optical pulses in the experiments was a Quantel Nd:YAG laser which is both actively and passively mode locked. This laser is comercially available from Quantel Int'l. The operation of the laser is as follows (see Fig. (2.1)). The laser rod, which is situated at Brewsters angle, is pumped by two Xenon flash lamps. Lasing occurs with 'p' type polarization. Mode locking is initiated by a combination of an acoustic optic crystal which is modulated at the round trip time of the cavity. The acoustic optic mode locker modulates the lasing flouresence. This modulated flouresence has random noise bursts and fluxuations which are amplified by the laser rod. As the light passes through the saturable absorber, the largest noise burst bleaches the saturable absorber (located at the end of the cavity). The largest noise burst becomes preferentially selected, while all of the weaker noise bursts become absorbed by the saturable absorber. After a few round trips in the cavity, a well defined single pulse develops with a pulse duration of about 40 psec. at the lasing wavelength of 1.06 $\mu$m.

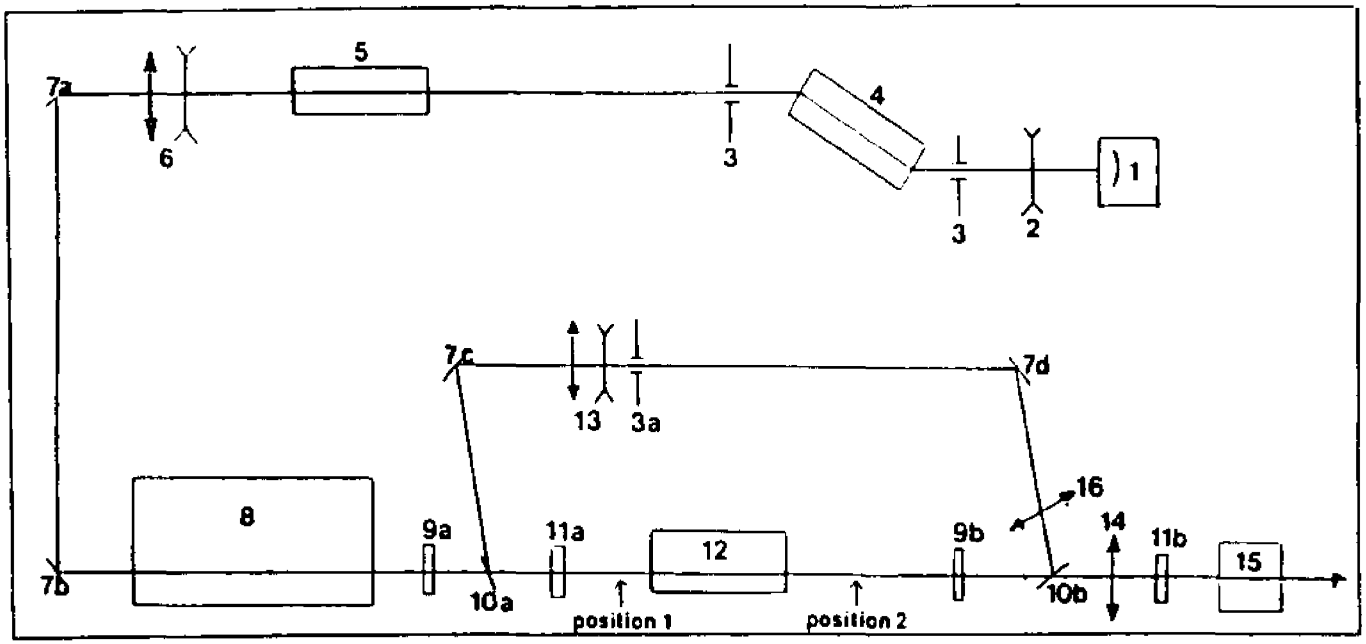

LEGEND

RING FREE MODE

1) MS400 mode-locking dye cell
2) Diverging lens
3) Pinhole
4) SF408-07 Brewster/Brewster oscillator
5) AML-1 (Acousto-optic mode-locker)
6) Beam expanding telescope, +155, -92
7) 45° turning mirror
8) PF302 pulse slicer
9) λ/2 plate
10) Dielectric polarizer
11) λ/4 plate
12) SF410-09 2°/2° amplifier head
13) Beam expanding telescope, +155, -104
14) Converging lens
15) Second Harmonic Generator (SHG)
16) +50cm lens

Fig. (2.1): Layout of the Quantel Nd:YAG laser

The active mode locker is an acoustic optic crystal, and is situated inside the laser cavity. The electrical modulation impressed on the acoustic optic crystal is a radio frequency signal with a modulation frequency equal to the round trip time of the cavity. This creates sidebands or additional frequency components on each side of the allowed longitudinal frequency components of the laser cavity. The saturable absorber and acoustic optic mode locker are coupled in the sense that the newly created sidebands of a particular longitudinal frequency component are exactly equal to the next higher and lower longitudinal cavity frequencies. This action couples all of the allowed longitudinal frequency components of the laser cavity. The combined action of the saturable absorber and the acousto-optic crystal allows the production of ~ 40 psec. pulses at $1.06\mu m$, in a gaussian envelope of about 10-12 pulses in the train. The total energy in the train is about 7 mj. The saturable absorber has the greatest effect on decreasing the pulse duration, while the acousto-optic crystal has the greatest effect on the shot to shot stability.

The stability of the laser with the active and passive modelocking can be checked by using a slow photodetector and a Tektronix 7934 storage oscilloscope. The scope is set for a slow sweep (~ 15 sec/full screen). Long term changes in the intensity of the laser pulse envelope manifests itself as a low frequency amplitude modulation on the storage scope trace. A typical output oscilloscope trace from the storage scope is shown in Fig. (2.2)

The output from the laser cavity is a train of pulses at $1.06\mu m$, where each pulse has a duration of ~ 40 psec. (see Fig (2.3)). A train of pulses is emitted because each time the oscillating pulse hits the output mirror, a portion is transmitted. The envelop impressed upon the train of pulses corresponds to the intensity envelope of the flash lamps during the time a population inversion occurs.

The train of laser pulses is then directed into a Pockels cell pulse slicer. This

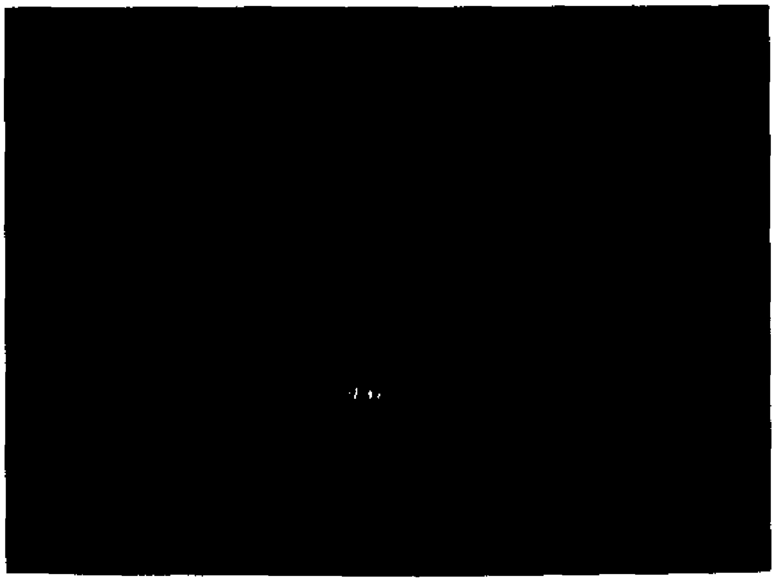

Fig. (2.2): Oscilloscope trace showing the long term stability of the Nd:YAG pulse train.

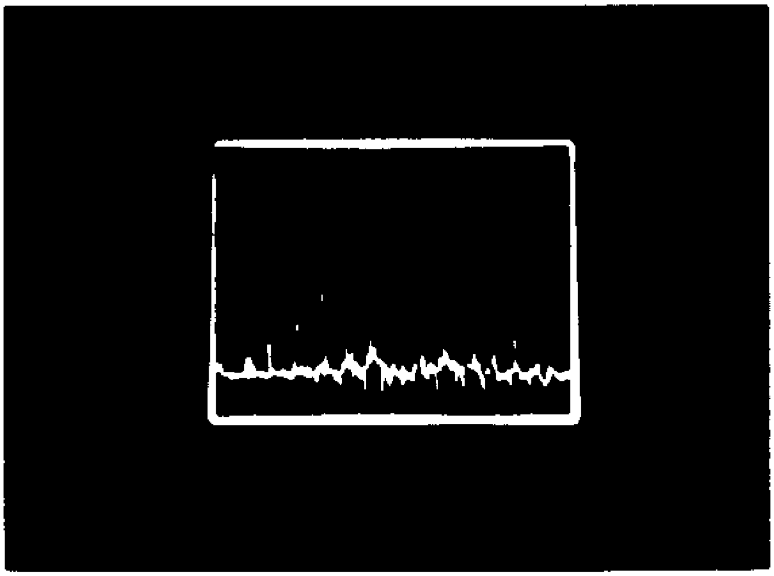

Fig. (2.3): Oscilloscope trace of the pulse train emitted from the Nd:YAG laser.

is esentially an electro-optic crystal which rotates the plane of polarization of one of the optical pulses in the train. By using polarizing optics and a well defined voltage pulse exactly timed with the lasing process, a single laser pulse can be extraced from the pulse train. The rejected or unwanted train of pulses can be monitored by using a fast photodiode connected to a Tektronix 7104 oscilloscope, to monitor the pulse selection process. The two types of photodiodes which were used are 1) an S-1 detector biased with 1.5kV, and 2) a Motorola MRD 510 photodiode connected in an RC circuit biased with 20 volts. The ejected pulse from the pulse slicer is 's' polarized. The single selected pulse is shown in Fig. (2.4).

The alignment of the Pockels cell is obtained by diffusing the incoming 1.06 $\mu$m radiation with lense tissue. The diffused light is then sent into the Pockels cell and through a cross polarizer. This shows the standard Maltese cross pattern which shows the crystaline optic axis. The crystal is then adjusted so that the 1.06 $\mu$m radiation has its optical path in the center of the Maltese cross pattern. Once this accomplished, the Pockek cell is properly aligned.

After the pulse slicer has selected a single laser pulse from the train, it is sent into a double pass ring amplifier. The amplifying laser rod is 9 mm. in diameter. By using half wave plates and polarizing beam splitters, the single laser pulse can be amplified to ~75 mj. The pulse energy is measured with a Scientech calorimeter energy power meter, model number 362. The transverse mode structure after amplification is multimode.

The description of the ring amplifier segment is as follows (see Fig. (2.1)). After the pulse slicer, the laser pulse is sent through a half wave plate to convert the 's' polarized light to 'p' polarized light. The pulse passes through the amplifier rod for the first pass. Upon exiting the amplifier rod, the pulse pass through a second half wave plate. The pulse now becomes 's' polarized and is reflected from a polarizing beam splitter. The amplified pulse is then reflected from the beam

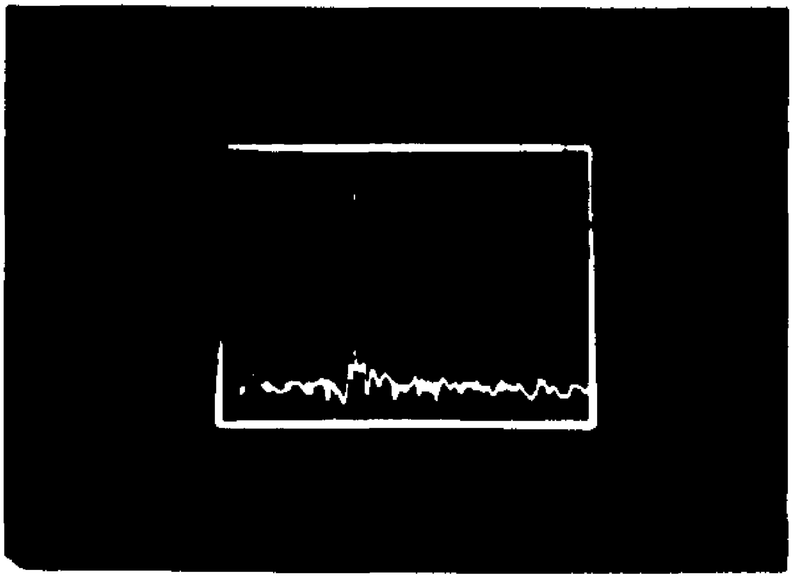

Fig. (2.4): Oscilloscope trace of a single laser pulse.

splitter and is directed back towards the input end of the amplifying laser rod. The laser pulse is then reflected into the amplifying rod by a second polarizing beam splitter. After this second pass through the amplifier rod, the amplified pulse passes through the second half wave plate, converting the polarization of the amplified pulse to the p polarized state. With this polarization, the amplified pulse passes through the polarizing beam splitter. At this point of the laser system, the amplified pulse has can have a maximum energy of ~75 mj. and a pulse duration of ~ 35 psec. The pulse duration of the fundamental can be measured using second harmonic autocorrelation techniques or by two-photon fluoresence in Rhodamine 6G.

The alignment procedures for the Nd:YAG laser use a HeNe laser and several pinholes which reference the optical beam path. The oscillator alignment procedure is to align the back reflections from both the front and rear mirrors to retrace their original beam paths, back into the HeNe laser. The double pass amplifier is aligned using two reference pinholes, one on each side of the amplifying YAG rod. Burn paper is used to make sure that the first pass is properly centered in the amplifiying rod. The amplified pulse (first pass) is then redirected into the YAG rod making sure that the amplified pulse cross section is concentric with the first pass.

The amplified pulse is then sent through a type I second harmonic generator crystal (KDP). This crystal converts thirty percent of the input laser light at 1.06 $\mu$m to the second harmonic frequency at 532 nm. The pulse duration of the second harmonic light is ~25-30 psec., with an 's' polarization state. Similar techniques can be used to measure the temporal duration of the second harmonic pulse. Alternatively, the streak camera can be used to obtain a real time single shot measurement of the pulse (see streak camera section).

## [2.3] The Optical Multichannel Analyzer (OMA) and Spectrometer

The spectral measurements were performed with a 1 meter Jarrell Ash Czerny-Turner spectrometer in conjunction with an optical multichannel analyzer (OMA). The OMA is essentially a 2 dimensional diode array which measures the spatial distribution of light intensity. Using the OMA detector and a computer console, specific regions of the OMA detector array can be accessed or integrated to increase the signal to noise ratio. The OMA has about 500 x 500 pixels in a 1 $cm^2$ active area, and a dynamic range on the order of 1000. Spectra can be recorded on a single shot basis or by collecting and averaging multiple shots. In addition, background scattered light can be recorded and subtracted from the desired signal spectrum, to increase the signal to noise ratio. Each spectra can be recorded and stored on a floppy disk. Hard copy of the sp~~ectra is obtain~~ed by routing the data to an x-y recorder.

Computer analyses of the spectra obtained from the OMA are also performed. The software for the spectral fitting is contained in the Appendix. A detailed example of utilizing the software is contained in Chapter 4.

The spectrometer utilizes a 600 line pairs per mm. grating for spatially dispersing the incoming light. Typical input slit widths used were on the order of 50-100 microns. With these experimental conditions, spectra spanning 700 wavenumbers could be obtained, with a spectral resolution of about 3.5 wavenumbers (HWHM).

## [2.4] The Streak Camera

For performing measurements of optical pulse intensity versus time, a Hamamatsu model 1587 streak camera, with an ultimate temporal resolution of 2 psec, was employed. The streak camera is a device which measures the intensity profile of an optical event versus time. The concept of a streak camera can be thought of as an optical oscilloscope, where the light intensity is measured versus time, as opposed to the voltage which is measured in a conventional oscilloscope. The operating principle of the streak camera is as follows. The light emitted from an optical event is focused onto a photocathode (see Fig. (2.5)). The photocathode emits electrons, where the number of electrons emitted are proportional to the light intensity. These photoelectrons are accelerated and passed through two parallel plates. The photoelectrons are deflected across a phosphor screen by a ramp voltage produced by the sweep generator. The resulting spatial distribution of photoelectrons in the swept direction represents the temporal intensity distribution from the optical event. The spatial distributiion of light emitted from the phosphor screen is detected and measured using a SIT camera and displayed on a T.V. monitor. Specific areas of the T.V. monitor can be windowed or selected and integrated, to eliminate undesirable noise fluctuation in the streak camera output. After obtaining the desired temporal evolution of the optical event, the data is directed to an x-y recorder for hard copy output, or sent to an IBM PC for storage and later data manipulation.

The typical data manipulations which are performed on the streak camera data are 1) averaging several single shot events to eliminate noise fluctuations in the streak camera output, and 2) fitting the pulse shapes obtained from the streak camera using standard convolutional algorithms. The software for these procedures are contained in the Appendix along with a description of its purpose and instructions for its use.

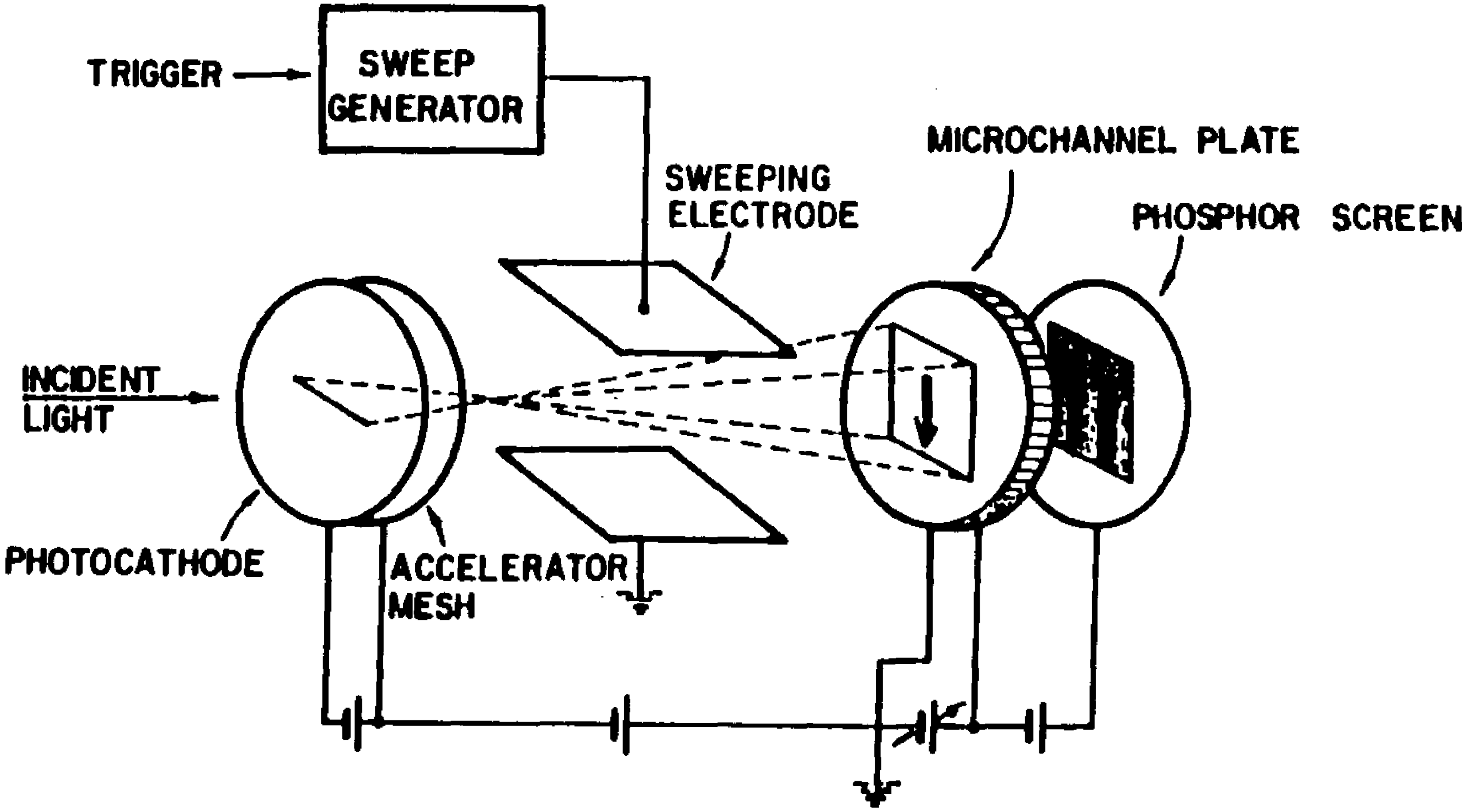

Fig. (2.5): Schematic of a streak camera.

## CHAPTER 3

## DEGENERATE AND NONDEGENERATE OPTICAL PHASE CONJUGATION

### [3.1] Introduction

In this chapter, the phase conjugation method will be described for both the degenerate four wave mixing and nondegenerate Raman Induced Phase-conjugation Spectroscopy technique (RIPS). The potential of the RIPS technique to be used as a time resolved pump probe tool to measure the temporal dynamics of molecular vibrations and optical phonons will be described.

Phase conjugation dates back to the developement of optical diffraction gratings using ultrasonic waves in the early 1960's. With the advent of the laser, interacting light waves became a suitable means of generating a light induced diffraction grating. The first experimental observation of a light induced diffraction was performed by Chaio, Kelley [1], and Garmire and Carmen t [2].

Optical phase conjugation is a nonlinear optical process which exactly reverses the direction and overall phase factor of an arbitrary optical beam [3]. When an optical beam traverses through some static spatially distorting medium and is then incident on a phase conjugate mirror, the optical beam will be reflected back so that all of the $\bar{k}$ vectors are exactly reversed and will retrace the original beam path through the distorting medium. As the phase conjugate optical beam traverses the distorting medium, the phase, which has been reversed in the phase conjugate process, becomes exactly undone. The phase conjugate optical beam emerges from the distorting medium as if no distorting medium was in the original path of the optical beam. This process is depicted schematically in Fig. (3.1). This phenomena has the potential to revolutionize the existing techniques for removing abberations in optical beams and systems [3].

One of the now standard methods of generating phase conjugate waves util-

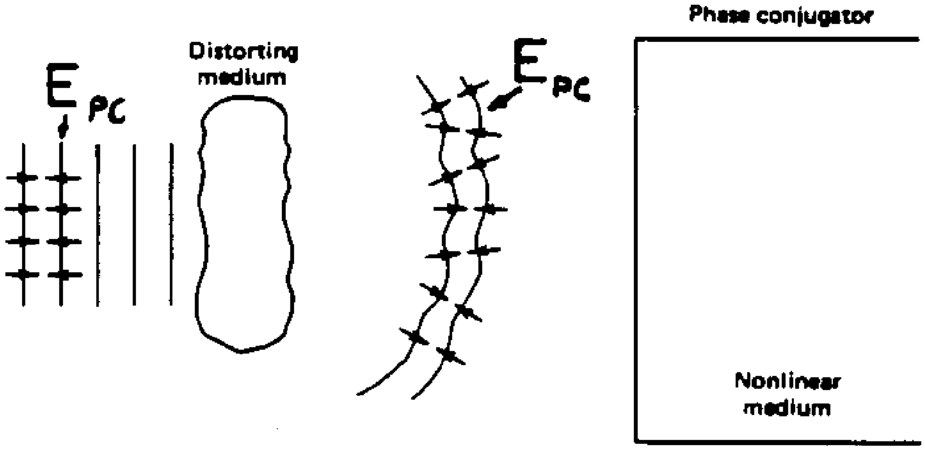

Fig. (3.1): Schematic of the optical phase conjugate process.

izes nonlinear four wave mixing. This method is intimately related to holography, and simple analogies can be made between the two phenomena. The concept of phase conjugation will be illustrated using degenerate four wave mixing techniques. These concepts will be generalized to the nondegenerate four wave mixing scheme and how it relates to Raman Induced Phase-Conjugation Spectroscopy (RIPS).

In the standard nonlinear degenerate four wave mixing scheme, three beams of the same frequency interact in a nonlinear optical material. The optical geometry which is characteristic of this technique has two of the interacting beams propagating exactly opposite to each other. The third beam enters the nonlinear material at an arbitrary angle into the region where the two beams are counterpropagating. These three beams become coupled through the third order nonlinear susceptibility $X^3$, and produce a scattered phase conjugate wave which exits the nonlinear material in a direction opposite to the third probing beam (see schematic in Fig. (3.2). This interaction can be simply viewed as a real time holographic process which occurs through the nonlinear optical properties of the sample under study. In Figure (3.3), three plane waves, $E_1$, $E_2$, and $E_3$, interact in a nonlinear material in the geometry described above. The foward and backward beams are denoted by $E_1$ and $E_2$ respectively, and the third probing beam is given by $E_3$. Assuming plane waves, the coherent superposition of beams $E_1$ and $E_3$ create a static periodic spatial intensity distribution, analogous with the formation of a hologram. This spatial modulation of the intensity distribution can be recorded in the material by affecting the materials intensity dependent index of refraction. This interference pattern, or grating, Bragg scatters a portion of $E_2$ in the direction opposite to $E_3$ to form a part of the phase conjugate signal. Similarly, $E_2$ and $E_3$ form a grating which is read out by $E_1$. The coherent interaction of beams $E_1$ and $E_2$ do not produce a spatially static modulation. Instead, a tem-

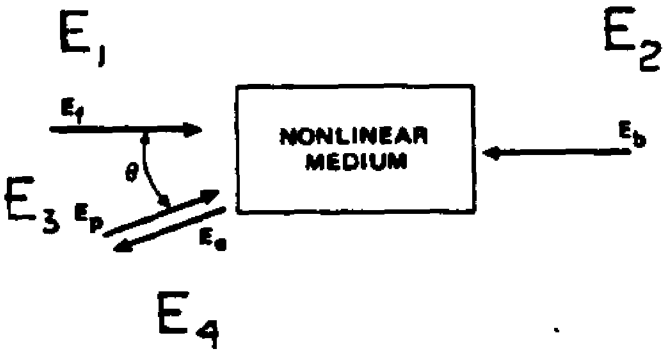

Fig. (3.2): The phase conjugate geometry.

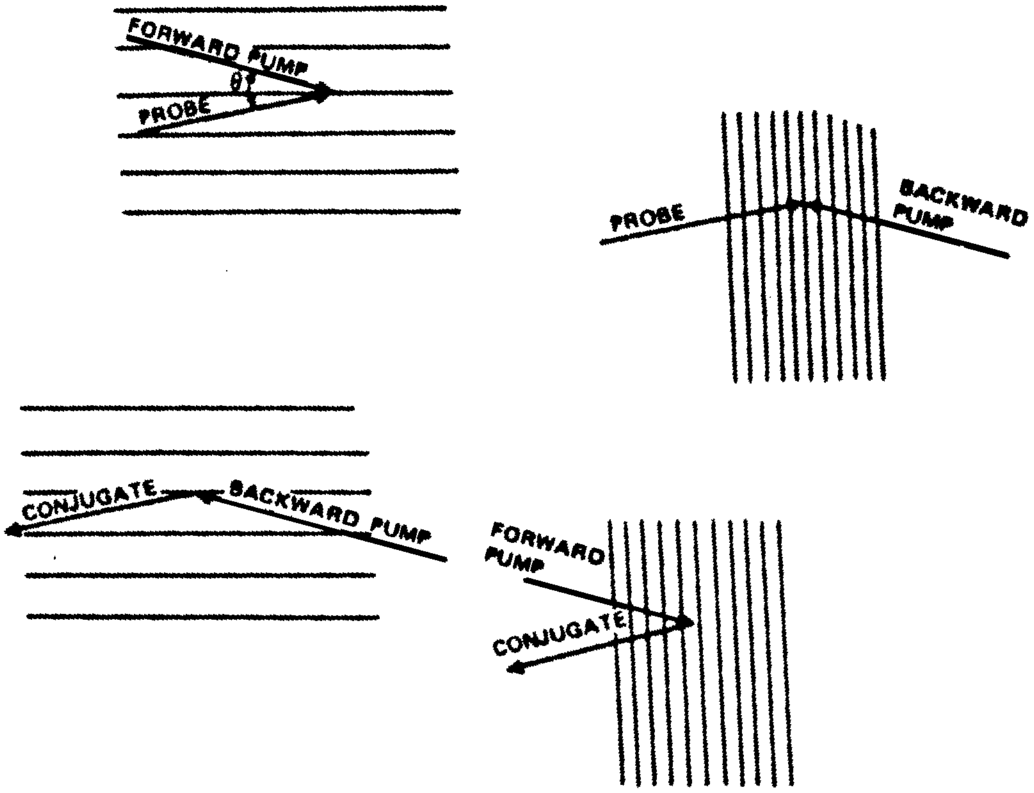

Fig. (3.3): The formation of transient grating during the phase conjugate process.

porally modulated grating is produced, which oscillates at a frequency of 2ω (not shown). This temporally modulated index reflects a portion of the probing beam $E_3$ to form the phase conjugate signal.

The nonlinear polarization for this case is given by [4]

$$P_{NL}^{3} = A\,(E_1E_3^*)E_2 + B\,(E_2E_3^*)E_1 + C\,(E_1E_2)E_3^* + c.c. \tag{3.1}$$

where the A, B, and C are functions of the material and input angles. The first term in this equation corresponds to a spatial modualtion of the index of refraction due to the interaction of beams 1 and 3, which is probed by $E_2$. The second term corresponds to a spatial modulation of the index of refraction due to the interaction of beams 2 and 3, which is probed by $E_1$. The third term does not correspond to any spatial modulation of the index of refraction, however this term corresponds to the temporally modulated index which oscillates at 2ω. By utilizing picosecond optical pulses, the temporal dynamics of the physical mechanisms which give rise to these changes in the optical index, can be studied. A more detailed account of this technique, and the corresponding physics which are measured is given in section [3.2].

In the Raman Induced Phase-conjugation Spectroscopy (RIPS) scheme, the beams no longer have the same frequencies (see Fig. (3.4)). Beam $E_2$ is chosen to have a frequency ω-Ω, where Ω is a molecular vibration or optical phonon frequency. The nonlinear interaction of $E_3$ and $E_2$ produces a spatially modulated index of refraction, however, this grating is no longer stationary, but moves with a velocity which is proportional to the frequency difference and crossing angle. $E_1$ is scattered from this moving grating and is Doppler shifted to the Stokes frequency to form the Raman Induced Phase-conjugate signal. Normally, when the interacting beams have a frequency difference which does not correspond to a vibrational mode of the sample, the resulting scattering efficiency is very low. However, an increase in scattering efficiency is obtained when the input frequency difference is

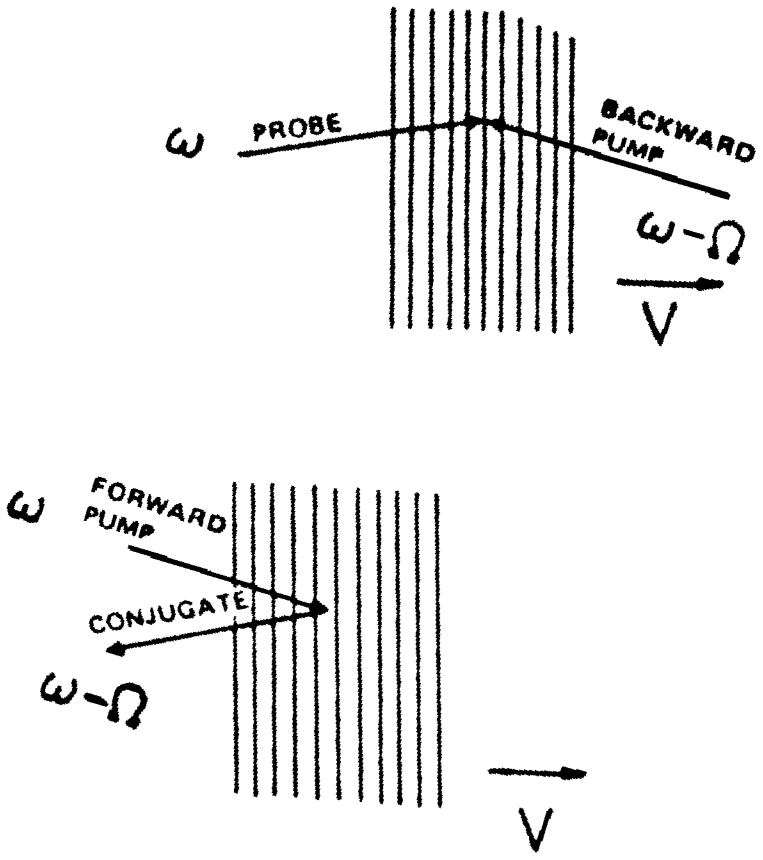

Fig. (3.4): Moving transient gratings in RIPS.

seperated by a vibrational mode frequency. This can easily be seen by the fact that the third order nonlinear susceptibility can be seperated into two main components [4], i.e.,

$$P_{NL} = (X_{NR} + X_R) E_1 E_2 E_3^* \tag{3.2}$$

where $X_{NR}$ is the nonresonant component of the susceptibility and $X_R$ is the Raman resonant component given by

$$X_R = \frac{a}{(\omega_l - \omega_s + \Omega) + i\Gamma} \tag{3.3}$$

One sees immediately that when two input laser beams when seperated in frequency by an amout equal to a vibrational mode $\Omega$ an increase in the value of the third order susceptibilty is obtained, which increases the scattering efficiency of the four wave mixing process.

S.K. Saha and R.W. Hellwarth were the first to use the Raman Induced Phase-conjugation technique as a spectroscopic tool [5]. In their pioneering work, an Nd:YAG nanosecond laser system was used as the source for the input optical pulses. A broadband optical pulse was used as the counterrunning beam for $E_2$. This type of source for beam 2 allows all phonons which have vibrational frequencies within the bandwidth of $E_2$ to couple to the four wave mixing process. The source for the broad band pulse was derived from the fluoresence of a rhodamine dye cell. The typical bandwidth for the dye was ~500 cm$^{-1}$.

In this thesis, I have extended this technique to the picosecond time regime. This type of optical source now allows for the direct measurement of the temporal evolution of the nonlinear polarization produced by the creation of coherent photo-generated optical phonons or molecular vibrations. In addition, I have also extended the tuning range of this technique by using self phase modulated light as the broadband optical source for beam 2. The bandwidth of this broadband or continuua source typically spans ~3000 cm$^{-1}$ on the Stokes side of the pumping laser frequency [6].

### [3.2] Pump-Probe Concept

Picosecond pulses can be used to study the temporal evolution of the photogenerated excitations in both degenerate and nondegenerate phase conjugate schemes. The way this is done is to use the picosecond pump-probe technique. In this technique, picosecond pulse are used to create the change of the optical properties of the sample under study. This type of excitation source is valuable because the temporal evolution of the photogenerated excitations can be monitored by interrogating the sample with an appropriately delayed pico second optical pulse. Measuring the scattered intensity of the interrogating probe pulse versus the delay gives a measure of the temporal evolution of the photogenerated optical excitation.

In all four wave mixing processes, all of the different grating processes occur simultaneously. By properly adjusting the input polarizations, input angles, and input frequencies, different physical mechanisms can be addressed. In addition, by properly delaying the different beams, individual grating mechanisms can be studied.

In the standard degenerate phase conjugate geometry, the interaction of the three beams simultaneous produce three grating processes (see Figs. (3.2) & (3.3)). By delaying beam 2 with respect to beams 1 and 3 measures the grating produced by the interaction of beams 1 and 3 (Fig. (3.2) and first term in Eq. (3.1)). In this case, the input angle is small. This leads to gratings with a wide spatial period. This minimizes effects due to the diffusion of excitations on the measurement. Delaying beam 1 with respect to beams 2 and 3 measures the grating produced by the interaction of beams 2 and 3 (Fig. (3.3) and second term in Eq. (3.1)). Since these two beams interact at a large angle, the grating spacing is small. As a result, diffusion has an increased effect on the measurement. The third term in Eq. (3.1) does not correspond to a spatial modulation of the intensity. As a result, no real spatial modulation of the index of refraction occurs. The temporal modulation at

2ω becomes the dominant mechanism for the light scattering process. As a result, delaying beam 3 with respect to beams 1 and 2 measures either the intensity or electric field correlation between the two counterpropagating pulses. In the case where the material relaxation is longer than the laser pulse duration, the electric field correlation with the material excitation is measured. When the material relaxation is short with respect to the laser pulse duration, the intensity correlation of the laser pulses is measured.

This can be seen by examining these two cases more carefully. The nonlinear polarization can be approximated by [9,10]:

$$P(t)=E_1(t)\int_{-\infty}^{t} E_2(\tau)E_3^*(\tau+\tau_d)A(t-\tau)d\tau dt \tag{3.4}$$

where $\tau_d$ is the probing delay time. When A(t) is short with respect to the laser pulse duration of E(t), i.e., A(t) → δ(t), this becomes

$$P(t)=E_1(t)\int_{-\infty}^{t} E_2(\tau)E_3^*(\tau+\tau_d)\delta(t-\tau)d\tau dt$$

which reduces to

$$E_1(t)E_2(t)E_3^*(t+\tau_d)$$

for the integral. The phase conjugate intensity detected by a slow detector is given by

$$I_{PC}\sim\int_{-\infty}^{\infty} P(t)P^*(t)dt\,,$$

which reduces to

$$I_{PC}(\tau_d)\sim|E_1|^2\int_{-\infty}^{\infty}|E_3(t+\tau_d)|^2|E_2(t)|^2dt. \tag{3.5}$$

This equation becomes

$$I_{PC}(\tau_d)\sim I_1\int_{-\infty}^{\infty} I_3(t+\tau_d)I_2(t)dt\,,$$

which gives the intensity correlation (pulse duration) of the laser pulses [9,10].

In the case where the material relaxation is longer than the laser pulse duration of E(t), i.e. A(t) → u(t) (u(t)-the unit step function=a const.) and E(t) →$\delta(t)$, Eq. (3.4) gives

$$I_{PC}(\tau_d) \sim \int_{-\infty}^{\infty}\int_{-\infty}^{t} | E_3^*(t+\tau_d)E_2(t)|^2 dt. \tag{3.6}$$

For times t much greater than the coherence time of the laser pulse, the upper limit of the inner integral in Eq. (3.6) can go to infinity. Then, Eq. (3.6) gives the electric field correlation (coherence time) of the laser pulses [9,10].

In the RIPS technique, a similar situation occurs. Delaying the Stokes beam (2), with respect to the two input lasers pulses (1,3) and monitoring the intensity of the scattered Stokes wave measures the normal wide spatial grating. Delaying beam 3 with respect to the counterpropagating laser and Stokes beams (1,2) measure the coherence between the two beams. However, the interaction of the Stokes and laser beams (2,3), produce a coherent phonon population at Ω. Delaying beam 1 with respect to the two pumping beams (2,3) measures the lifetime of the phonon population.

## [3.3] Grating Analysis

An excellent way for obtaining a physical picture to describe RIPS which is most closly related to a classical picture utilizes the concepts of diffraction analysis (see Fig. (3.2)). In ordinary degenerate four wave mixing phase conjugation, the coherent superposition of two pulses of the same polarization, $E_1$ and $E_3$ or $E_2$ and $E_3$, produce an interference pattern analogous to a hologram. This hologram is recorded into the material by an alteration of the materials optical index of refraction. The probing beam, $E_2$ or $E_3$ then scatters from the hologram to produce the scattered phase conjugate signal. The coherent superposition of two pulses of orthogonal polarization do not create an intensity grating. This configuration produces a spatial and time varying polarization grating. The instantaneous electric field polarization in space depends upon the relative phase difference between the two interacting pulses and also on the crossing angle of the two pulses. In some regions, the electric field polarization rotates through an angle of 90 degrees at a frequency of $2\omega$, while in other regions the direction of the electric field polarization remains unchanged, but still oscillates at $2\omega$. This oscillation of the electric field vector drives the electronic and atomic motions to produce an electric dipole moment which then radiates in the phase matched direction.

The salient feature of the interaction in the degenerate four wave mixing scheme is that it produces spatial modulations of the index of refraction which has a grating separation given by

$$\Lambda_g = \frac{\lambda}{2\sin(\frac{\theta}{2})} = 3.052\,\mu m \tag{3.7}$$

for the interaction of $E_1$ and $E_3$, and

$$\Lambda_g = \frac{\lambda}{2\cos(\frac{\theta}{2})} = 267\ nm \tag{3.8}$$

for the interaction of $E_2$ and $E_3$. In both of these equations, $\theta$ is the angle between $E_1$ and $E_3$. $E_2$ is counterpropragating to $E_1$.

In the Raman Induced Phase Conjugation scheme, the interacting beams no longer have the same input frequencies, so the situation is expected to be quite different. Consider the interaction of pulses $E_2$ and $E_3$ at frequencies of $\omega - \Omega$ and $\omega$, respectively, interacting at an angle of $180 - \theta$. It is obvious that there will be a new grating spacing and grating orientation due to the frequency difference. In addition, the grating will move with a finite velocity in a direction towards the incoming Stokes pulse. The probing pulse $E_1$ at $\omega$ enters opposite to $E_2$ and is Bragg scattered to form the phase conjugate signal. However, due to the velocity of the grating, the scattered signal is Doppler shifted to the Stokes frequency to form the RIPS signal.

Using a geometrical analysis, the new grating orientation, spacing and velocity can be calculated. The change in grating orientation from the degenerate grating produced by $E_2$ and $E_3$, to the moving grating picture can be calculated from Fig. (3.5) and is given by

$$d\phi = \sin^{-1}\left(\delta\lambda \sin\left(\frac{\theta}{2}\right) \cdot \left[2\sin(\theta)\left[\frac{\lambda^2}{4\sin^2\left(\frac{\theta}{2}\right)} + \frac{\delta\lambda^2}{4\sin^2(\theta)} + \frac{\lambda\delta\lambda}{2\sin(\theta)\tan\left(\frac{\theta}{2}\right)}\right]^{1/2}\right]^{-1}\right) \quad (3.9)$$

The physical interpretation of $d\phi$ is that the grating orientation in the moving grating picture is tilted from the degenerate phase conjugation case. This new orientation has an effect of reflecting the scattered signal in a direction slightly different from the phase conjugate direction. The parameter $d\phi$ gives the change in orientation of the moving grating as compared to the static degenerate grating.

In deriving this equation, plane waves are assumed for the two electric fields. The grating orientation is obtained by simply drawing lines which connect the regions of constructive interference between the planes of constant phase of the two intersecting waves. When $d\lambda$ is zero, i.e., all waves have the same frequency, the equation gives $d\phi=0$. This says that when $d\lambda$ is zero, the grating orientation returns to the DFWM case.

From the same figure, the spacing of the moving grating, $\Lambda_{mg}$, can be calculated. This is given by

$$\Lambda_{mg} = \left[\frac{\lambda}{2\cos\left(\frac{\theta}{2}\right)} + \frac{\lambda\tan(d\phi)}{2\sin\left(\frac{\theta}{2}\right)}\right]\cos(d\phi) \quad (3.10)$$

The first term inside the bracket is the grating spacing in the degenerate phase conjugate case corresponding to Eq. (3.8) and Fig. (3.3). In these equations, $\theta$ is the angle between $E_1$ and $E_3$, and $\delta\lambda$ is the difference between the laser and Stokes wavelengths. It should be noted here that the grating spacing is related to the phonon $\vec{k}$ vector using

$$2\pi/\Lambda = \vec{k}_{phonon} .$$

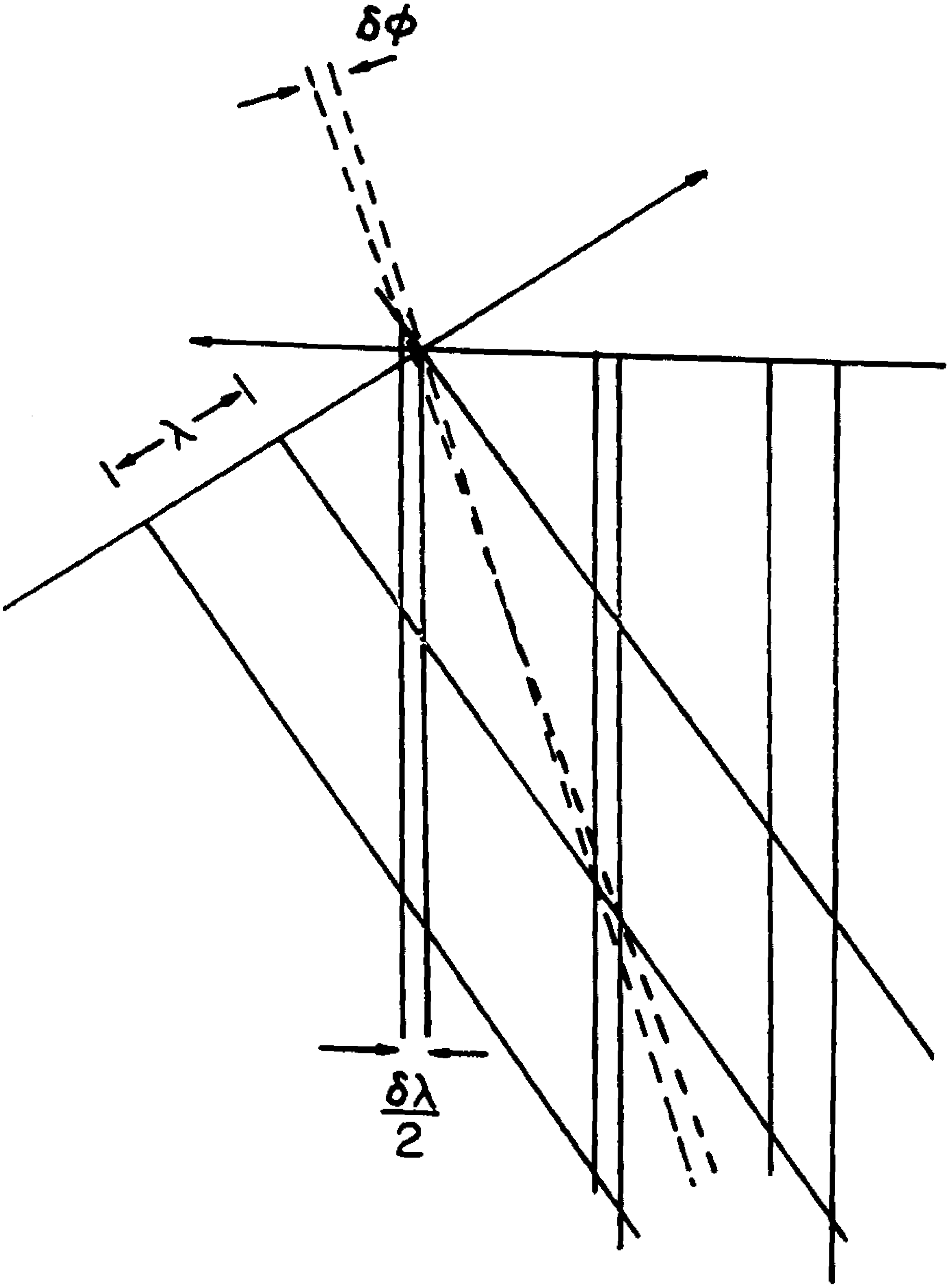

Fig. (3.5): Geometrical construction for deriving the moving grating orientation, and spacing.

A more detailed analysis which relates the grating parameters and the phonon k vector and vibrational frequency $\Omega$ is given in the next section. In the case where $\delta\lambda=0$, all of the above equations reduce to the degenerate four wave mixing case.

The velocity of the moving grating can be obtained by calculating the distance the grating moves when both pulses are allowed to propagate a distance $c\delta t$, where c is the speed of light and $\delta t$ is a time increment (see Fig. (3.6)). For simplicity, we have assumed no dispersion, i.e., $n(\omega)=n(\omega-\Omega)$. The resulting grating velocity excluding dispersion is given by

$$V_g = \frac{2\sin(d\,\phi)c\cos(\frac{\theta}{2})}{\sin(\theta)} \tag{3.11}$$

The generalization to the case which includes dispersion is easily obtained by letting $E_2$ travel a distance $c\delta t/n(\omega)$ and $E_3$ travel $c\delta t/n(\omega-\Omega)$, where $n(\cdot)$ is the frequency dependent index of refraction.

Again, in the degenerate case, $\nu\to0$ as $\delta\lambda\to0$. As an example, let $\lambda=530$ nm. and $\delta\lambda=20$ nm. ( i.e., $\Omega=686\ \mathrm{cm}^{-1}$) with a crossing angle of $180-\theta$, $\theta=10$ degrees. We see that $d\phi=.09282$ degrees, $\Lambda=270.93$ nm., and $v_g=5.57677\times10^6$ m/s. From this we see that the change in grating orientation is small, so the RIPS scattered signal will emerge from the sample in a direction nearly identical to the degenerate phase conjugate signal.

To calculate the wavelength of the RIPS scattered signal from the moving grating, the Doppler formula must be used. One sees that if an observer is in a rest frame of the moving grating, the observed frequency is given by

$$\nu=\nu_0(1-\frac{V_g}{c}\cos(\theta+d\,\phi)) \tag{3.12}$$

where $\cos(\theta+d\phi)$ in this case gives the $\vec{k}$ vector component of the velocity of the moving grating in the direction of $E_1$, and $\nu_0$ is the input frequency. Using the above values give $\lambda=540$ nm. In the rest frame of the moving grating, the light at 540 nm. is Bragg scattered from a conventional periodic grating. However, the

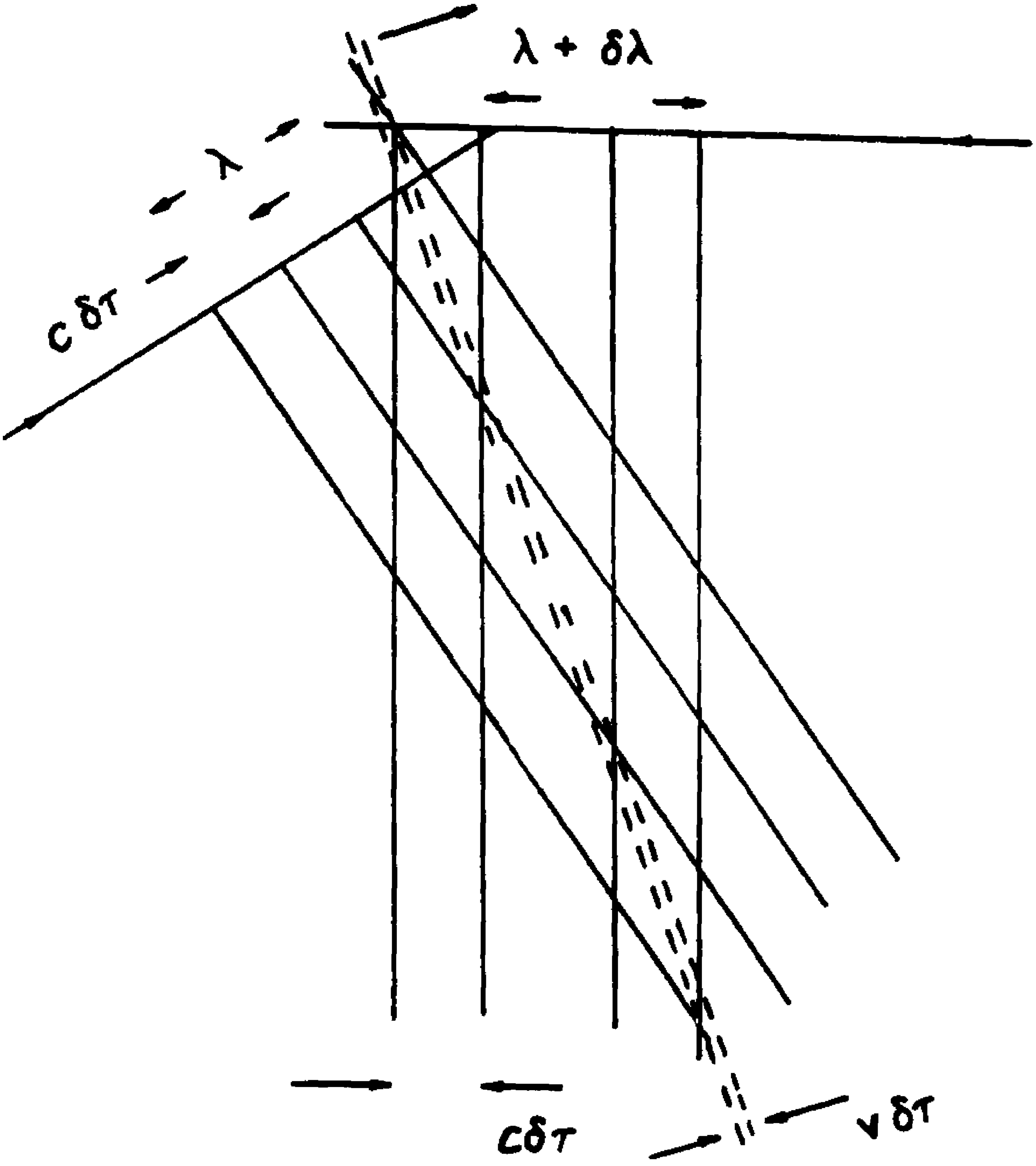

Fig. (3.6): Geometrical construction for deriving the moving grating velocity.

detector is moving relative to the rest frame of the moving grating, and hence detects a signal which is again doppler shifted. This yields a detected wavelength in the laboratory rest frame of 550 nm., which is in excellent agreement with the wavelength of the input Stokes pulse. To check this analysis, we see that the new spatial grating $\Lambda$ is matched to Bragg scatter light at 540 nm., when the input angle is $\theta + d\phi$, i.e., when $E_1$ is counter propagating to $E_2$. The Bragg formula is

$$\lambda = 2\Lambda\cos(\frac{\theta}{2} + d\,\phi) \tag{3.13}$$

The wavelength obtained by using this equation gives exactly the wavelength which detected in the rest frame of the moving grating.

## [3.4] Relationship Between Phonons and Moving Grating Parameters

It is interesting to note that the physical parameters used in the moving grating model are intimately related to the phonon $\vec{k}$ vector and vibrational frequency $\Omega$. The phonon $\vec{k}$ vector is given by

$$\vec{k}_L - \vec{k}_S = \vec{k}_{phonon} \tag{3.14}$$

where the L and S sub scripts denote the laser and Stokes photon $\vec{k}$ vectors. This is just $2\pi/\Lambda_{mg}$. Since the velocity of the grating is known and the wavelength of the grating is also known, we find that the relation $\Omega = v\vec{k}$ holds. This can be verified by a simple numerical example. Using the grating spacing and the velocity of the grating for a 10 degree input angle and a 20 nm wavelength difference, shows that the time it takes for the grating to move one period is equal to 48.58 fsec, which is exactly the time it takes for the vibrational mode to complete one cycle, i.e., $1/\Omega$.

As another example of utilizing the moving grating analysis, we can plot the resulting scattered wavelength $\omega_4 = \omega_{out}$ in wavenumbers versus the input wavelength $\omega_2 = \omega_{in}$ in wavenumbers for a fixed crossing angle of 10 degrees. This gives a measure of the phase mismatch encountered in the four wave mixing process. From energy conservation, the scattered output wave should have a frequency [3]

$$\omega_4=\omega_1+\omega_2-\omega_3 \tag{3.15}$$

With $\omega_1=\omega_3=\omega$ and $\omega_2=\omega-\Omega$ we have from the above equation that

$$\omega_4=\omega-\Omega \tag{3.16}$$

that is, the output scattered phase conjugate Raman signal has a frequency equal to the Raman shifted input wave. Plotting the scattered output shifted frequency $\omega_4$versus the input frequency $\omega_2$ for a fixed crossing angle using the moving grating analysis, in Fig. (3.7), shows that the scattered output wavelength is nearly equal to the input detuned wavelength for a wide range of input wavelengths (dotted line). This shows that the phase mismatch for this mixing process is very small for large input frequency shifts. As a reference for perfect phase matching, a line corresponding the case where the scattered Stokes frequency is identical to the input Stokes frequency is also plotted and is shown by the solid line.

An alternate way of determining the phase matching region is to plot the difference between the input Stokes frequency and the scattered Stokes frequency, i.e., $\omega_2-\omega_{34}=\Delta\Omega$ versus $\omega_1-\omega_2=\Omega$. This is shown in Fig. (3.8). From this figure, the phase mismatch at a vibrational frequency of $\sim 1000$ cm$^{-1}$ is $\sim 13$ cm$^{-1}$, giving a ratio of .013. This small number is an indication that good phase matching is obtained over a wide spectral bandwidth.

The $\vec{k}$ vector of the excited phonon depends on the crossing angle of the laser and Stokes beams. Thus, changing the crossing angle will drive phonons at different points on the phonon dispersion curve. This can be seen by plotting the dependence of the phonon $\vec{K}$ vector versus the input angle $\theta$. This is plotted in Fig. (3.8a).

The moving grating has its own dispersion relation which is a function of the input frequencies and input angles. This dispersion relation can be obtained by

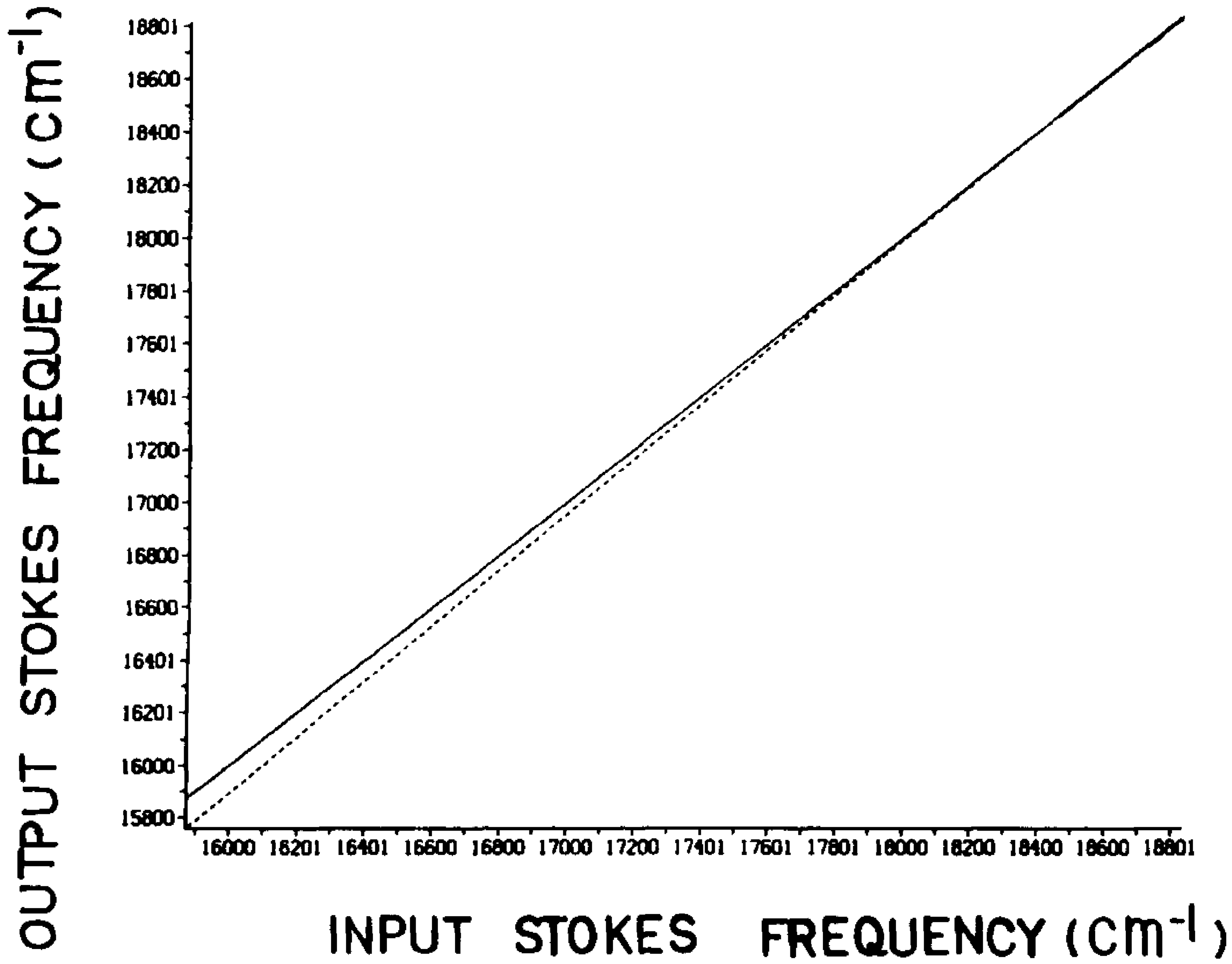

Fig. (3.7): Output scattered Stokes frequency plotted versus the input Stokes frequency.

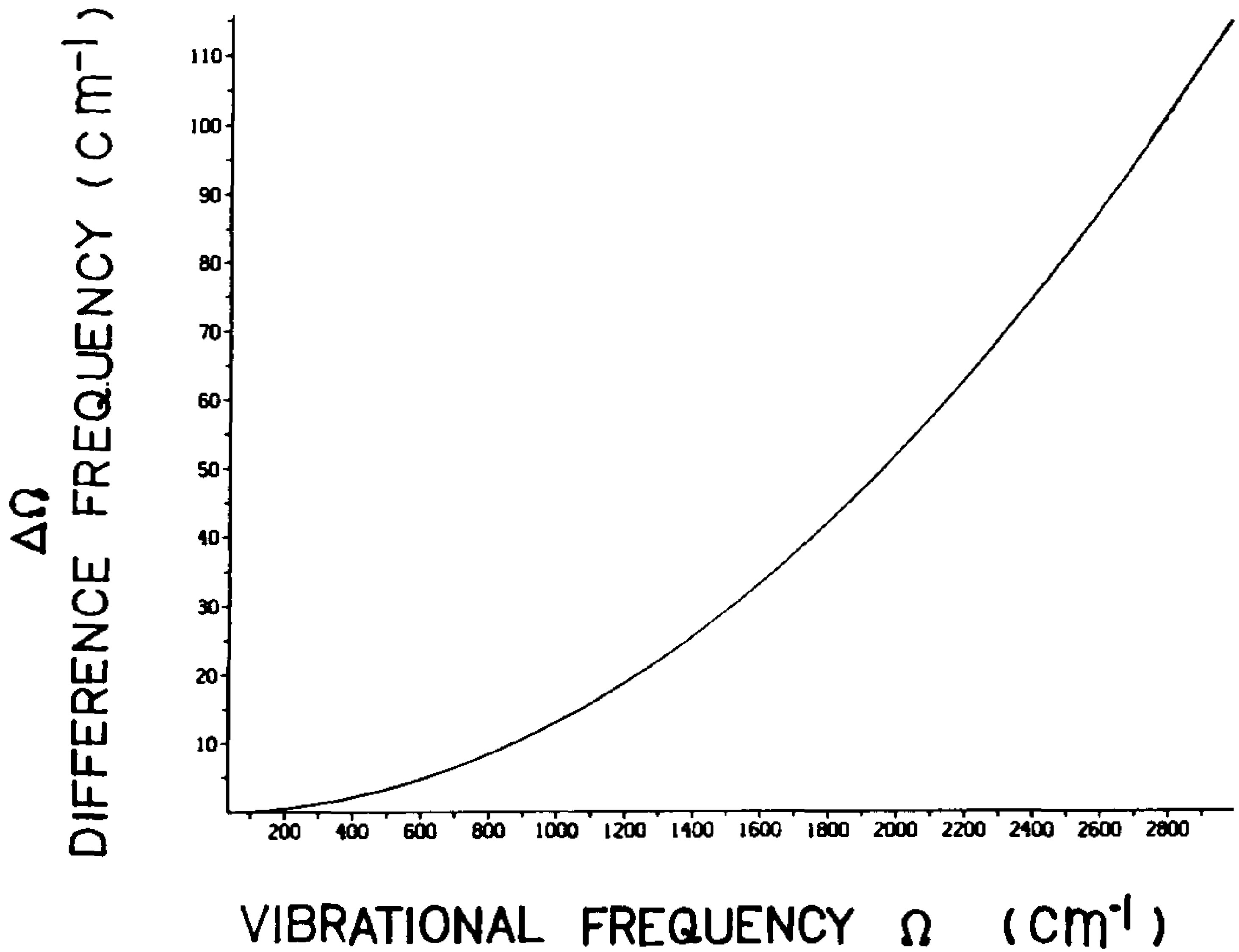

Fig. (3.8): The difference between the input Stokes frequency and the output scattered Stokes frequency plotted versus the excited vibrational frequency Ω

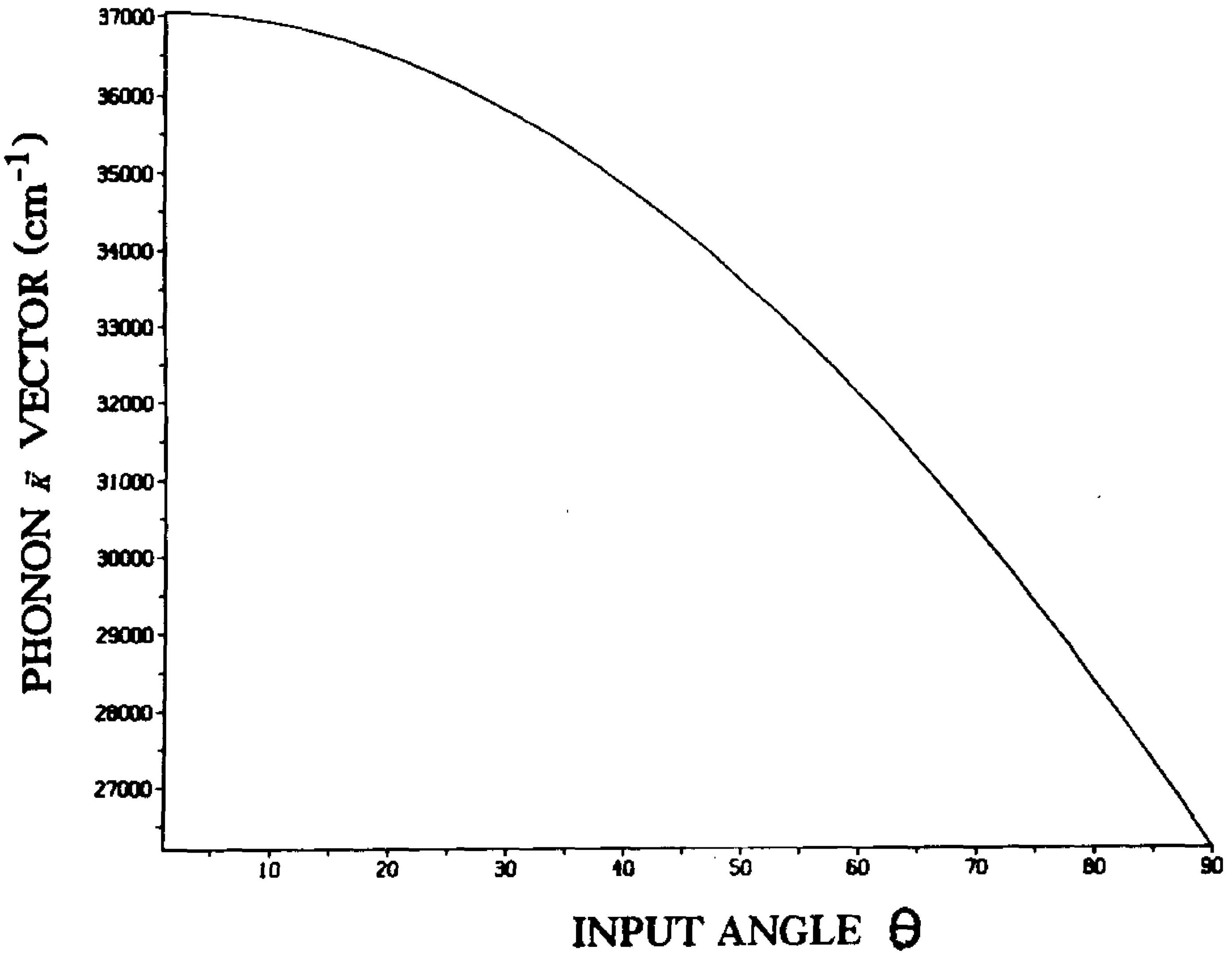

Fig. (3.8a): The phonon $\vec{k}$ vector dependence on the input angle $\theta$ (for constant excited vibrational frequency $\Omega$=686 cm$^{-1}$. The actual crossing angle of the laser and Stokes beams is 180-$\theta$.

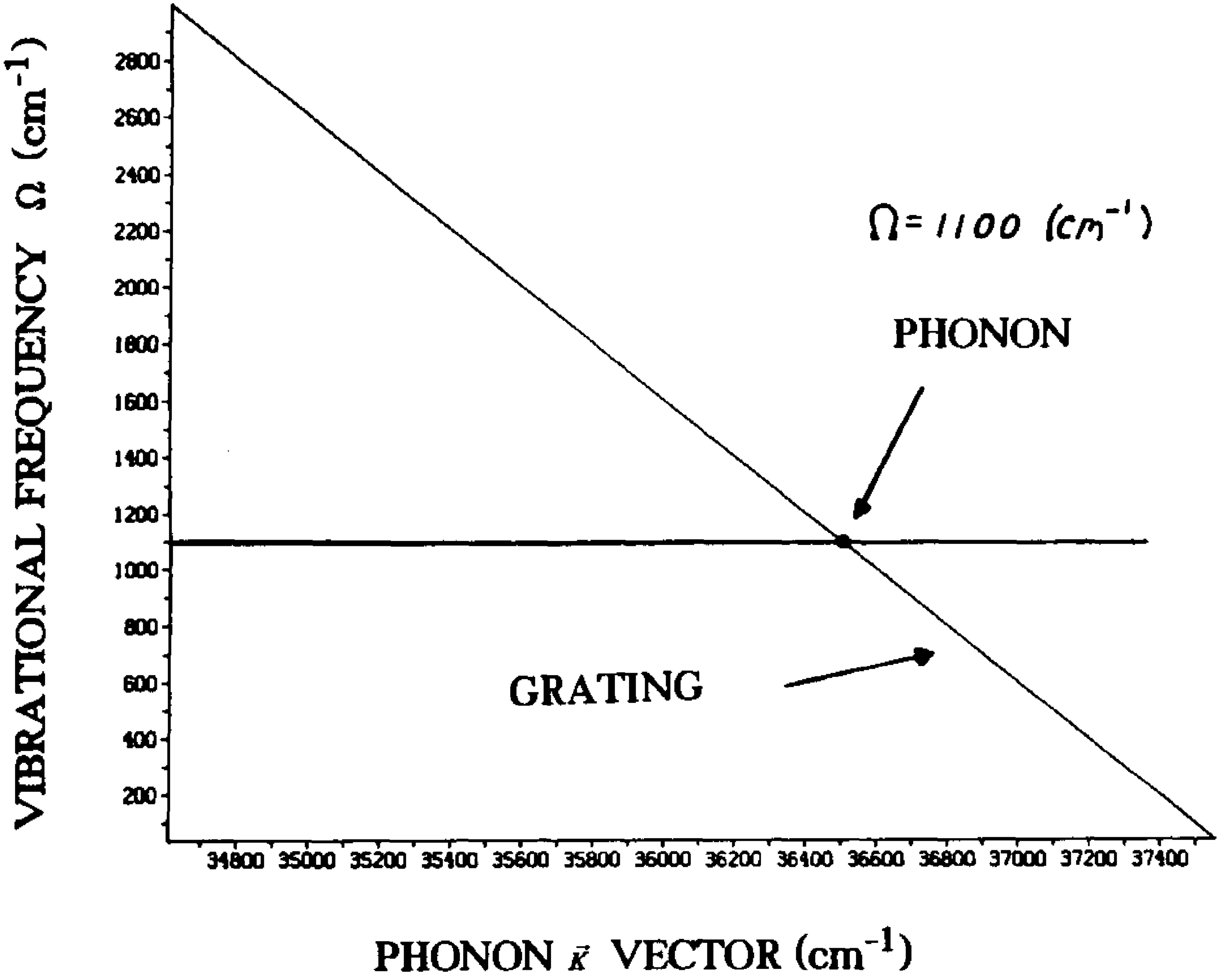

Fig. (3.9): The moving grating dispersion curve.

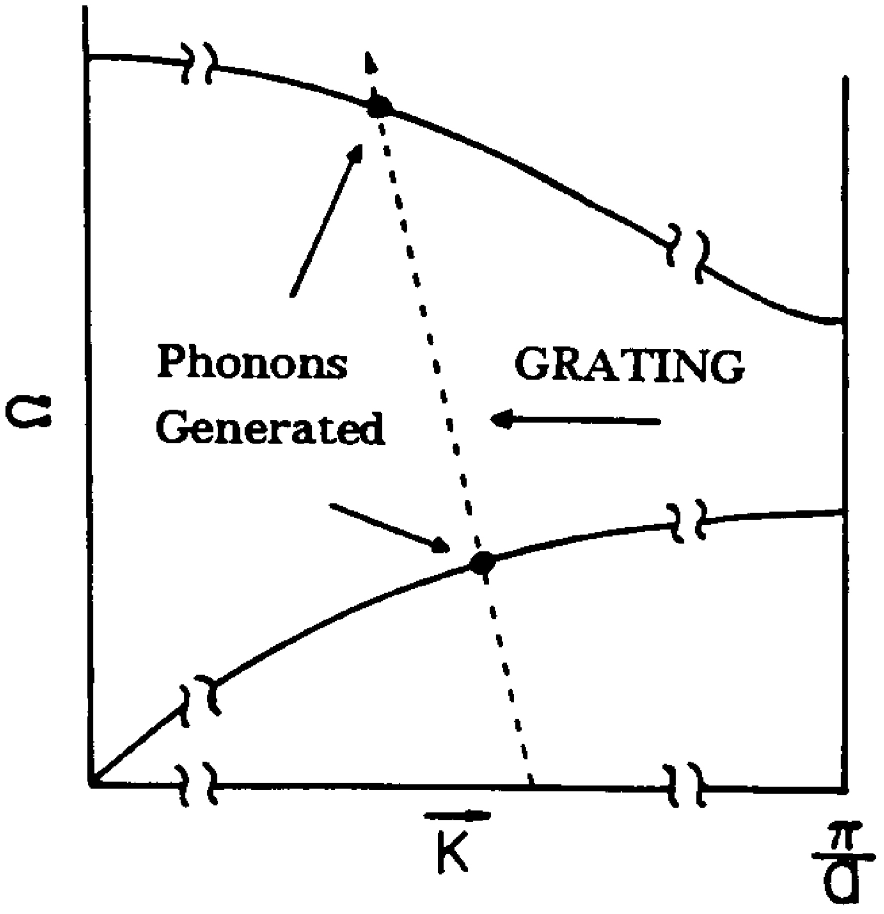

Fig. (3.10): Schematic of how the moving grating dispersion curve interacts with the normal phonon dispersion curve.

expressing the excited vibrational frequency $\Omega$ as a function of the $\vec{k}$ vector of the moving grating. It is important to remember that the $\vec{k}$ vector of the excited phonon is identical to the $\vec{k}$ vector of the moving grating. The dispersion curve for the moving grating is plotted in Fig. (3.9), for an input angle of 10 degrees. The range of $\vec{k}$ vectors obtainable by the excited phonon are limited to a small regime in the Brillouin zone. The relation between the phonon dispersion curve and the moving grating dispersion curve can be seen if they are plotted on top of each other (see Fig. (3.10). The intersection points of the two dispersion curves gives the exact values of the $\vec{k}$ vectors which can participate in the light scattering process. Obviously, by tuning the input Stokes frequency (beam 2), phonons with well defined frequency and k vector can be excited. More importantly, changing the input angle moves the grating dispersion curve along the phonon dispersion curve. Thus with a constant input Stokes frequency, the dispersion of the phonon mode can be obtained by changing the input angle. Another way of measuring the phonon dispersion curves for the sample under study is to tune the carrier frequency, $\omega_L$, while keeping the frequency difference $\Omega$ constant. This changes the phonon $\vec{k}$ vector which is determined by $k_L - k_S$. Thus the frequency difference is constant and the $\vec{k}$ vector of the phonon is changing, giving the phonon dispersion curves.

It should be noted that the above analysis should be used as a tool to obtain a feel for the physical process, and to offer a model which appeals to classical models, not to definitively and completely describe the RIPS phenomena. A more exact treatment relies on the nonlinear third order susceptibility, and will be discussed in the next chapter. In order to exemplify the analysis of the RIPS process, it will facilitate matters if a specific experimental case is considered. In the following chapter, $LiNbO_3$ will be used as the sample under study.

## [3.5] Experimental Spectra in Selected Samples

Before a detailed spectral analysis is performed, some typical RIPS spectra obtained are shown. The RIPS technique was sucessfully used to measure vibrational spectra of several liquids and crystaline solids. The typical RIPS spectra obtained in a 1 cm cell of nitrobenzene is shown in Fig. (3.11). Three strong Raman vibrational modes are observed between 1000 $cm^{-1}$ and 1600 $cm^{-1}$. These modes correspond to the strongest vibrational modes of nitrobenzene in this wavelength region [7]. Other liquids samples which yielded strong RIPS spectra are $CS_2$ benzene, bromobenze, and toluene.

The RIPS technique was also used to measure the Raman spectra due to optical phonons in the molecular crystal calcite. The typical Raman spectra in the region of the strongest $A_{1g}$ mode at 1086 $cm^{-1}$ is shown in Fig. (3.12). In this spectra, a slight asymmetry is observed in the output. This has previously been reported for calcite, using standard CARS techniques [8]. The asymmetry is attributed to an interference between resonant and nonresonant components of the third order susceptibility. A more detailed account of this phenomena is presented in the next chapter.

The potential for using this technique as a time resolved spectroscopic tool is discussed in Chapter 6. A complete analysis performed, considering the spatial and temporal overlap of the interacting pulses, and what effect this has on the experimental temporal resolution.

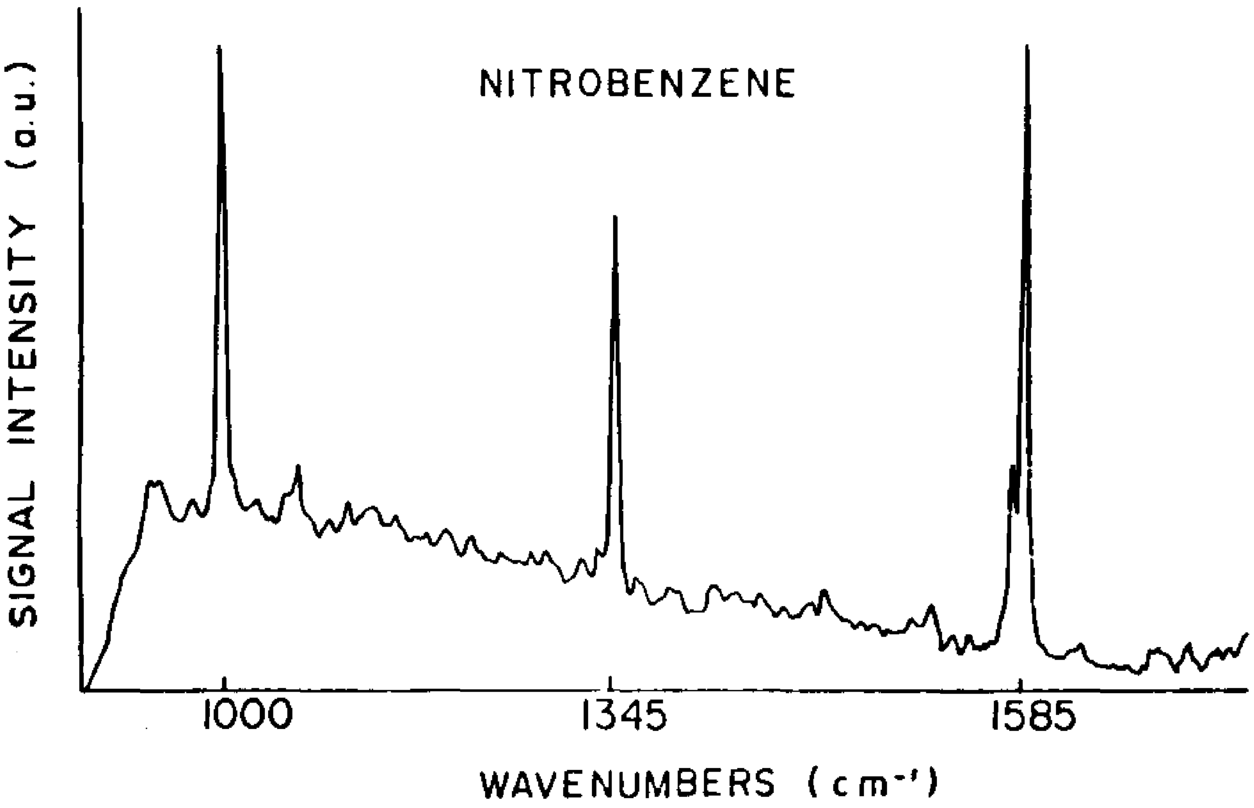

Fig. (3.11): RIPS spectra in nitrobenzene.

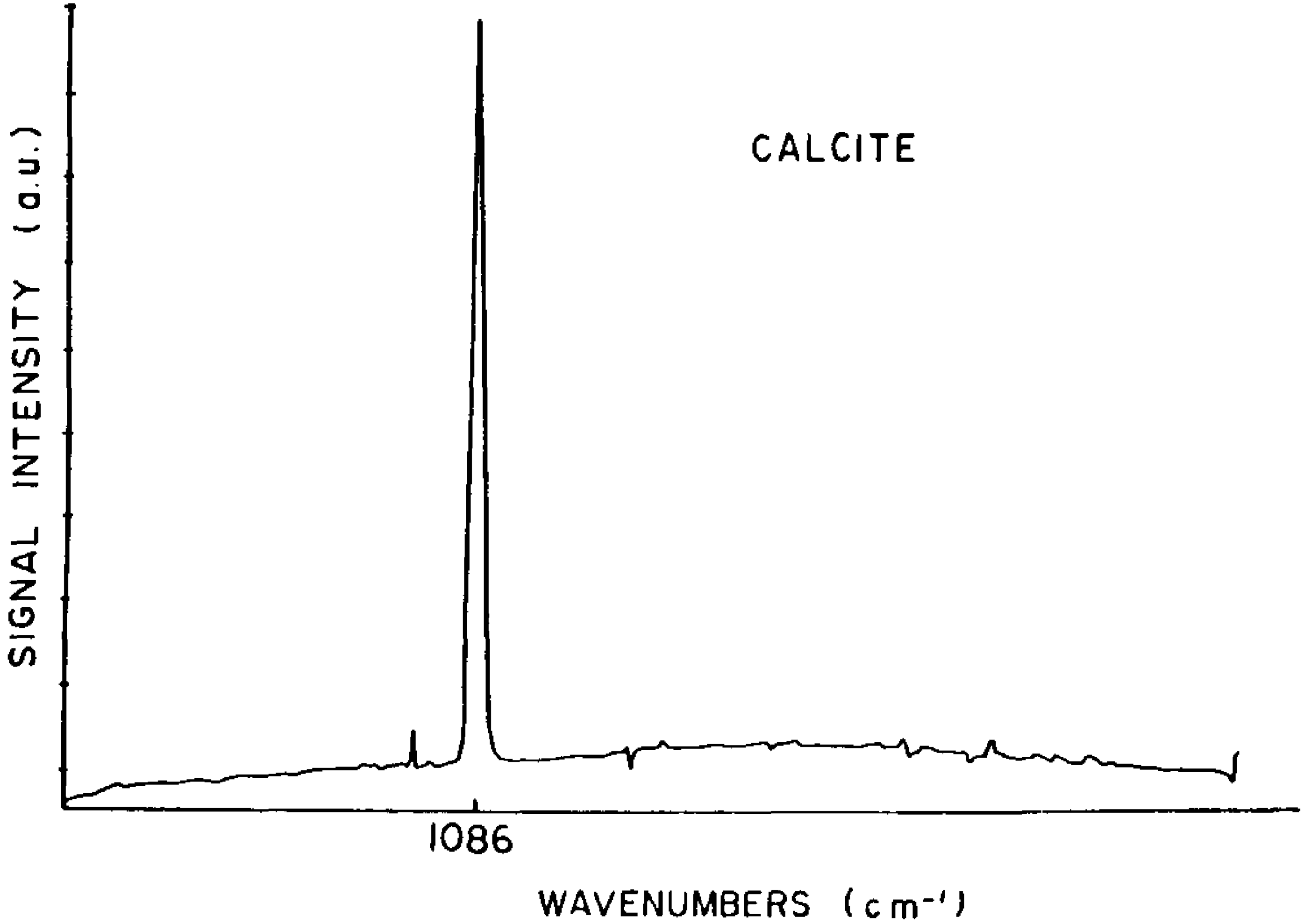

Fig. (3.12): RIPS spectra in calcite.

## Notes

[1] Chiao, R. Y., Kelly, P. L., and Garmire, E., Phys. Rev. Lett., Vol. 17, 1158, (1966)

[2] Carmen, R. L., Chaio, R. Y., and Kelly, P. L., Phys. Rev. Lett. Vol. 12, 1281, (1966)

[3] Fisher, R., Optical Phase Conjugation, Academic Press, N.Y., (1983)

[4] Shen, Y. R., Principles of Nonlinear Optics, Wiley Interscience, N.Y., (1985)

[5] Saha, S. K., and Hellwarth, R. W., Raman Induced Phase Conjugation Spectroscopy, Phys. Rev. A., Vol 27, No. 2, 919, (1983)

[6] Alfano, R. R., and Shapiro, S. L., Phys. Rev. Lett., Vol. 24,584, 592, (1970)

[7] Raman Spectral Data, Thermodynamics Research Center Data Project, Serial No. 109, Texas A&M Univ., College Station, Texas, (1974)

[8] Levenson, M. D., IEEE J. Quant. Electron. QE-10, 110, (1974)

[9] Buchert, J., Dorsinville, R., Delfyett, P. J., Krimchansky, S., and Alfano, R. R., Optics Comm., Vol. 52, No. 6, 433, (1985)

[10] Alfano, R. R., Semiconductors Probed by Ultrafast Laser Spectroscopy, Academic Press, N.Y., (1984)

# CHAPTER 4

# RAMAN INDUCED PHASE CONJUGATION SPECTROSCOPY (RIPS) in $LiNbO_3$.

## [4.1] Introduction to RIPS in $LiNbO_3$.

Nonlinear optical four wave mixing techniques are becoming the preferred method for isolating specific optical phenomena and obtaining information about fundamental processes and their response times in condensed matter. A multitude of nonlinear optical techniques exist which give information about the vibrational linewidths and lifetimes, and relative strength between the resonant and non-resonant components of the third order nonlinear susceptibility, such as coherent anti-Stokes Raman spectroscopy and Raman Induced Kerr Effect spectroscopy [1]. The reasons for utilizing the Raman Induced Phase-Conjugation Spectroscopy (RIPS) technique in this study as opposed to the older four wave mixing spectroscopic techniques are numerous:

1) The geometrical configuration of RIPS relaxes the phase matching requirements so that broadband phase matched Raman spectra can be obtained in isotropic or anisotropic materials with a single laser pulse.

2) The RIPS technique utilizes the phase conjugate geometry which allows the production of a time reversed or conjugate optical beam. This feature has tremendous potential in areas spanning real time adaptive optics, optical computing, pattern recognition and image processing.

Lithium niobate has the potential to be the nonlinear optical material at the heart of an all optical multispectral real time optical processor which requires large and fast nonlinearities and uses Raman Induced Phase-conjugation. In this chapter, time resolved Raman Induced Phase-conjugation Spectroscopy (RIPS) [2,3] is used as the nonlinear four wave mixing technique to measure the components of the nonlinear third order susceptibility as a function of frequency from 100 to 700 $cm^{-1}$ in $LiNbO_3$.

It is the purpose of this section of the Thesis to show that $LiNbO_3$ exhibits several resonantly enhanced peaks in the phase conjugate spectrum which, from the extracted linewidths, have subpicosecond relaxation times.

## [4.2] Experimental Method

The experimental configuration utilizes nondegenerate four wave mixing in the phase conjugate geometry. The main concept of this technique is to use two laser pulses at frequency $\omega$ (beams 1 and 3) and a third laser pulse at $\omega$-$\Omega$ (beam 2), where $\Omega$ is a molecular or optical phonon vibration, interacting at a large angle ~ 170 degrees in $LiNbO_3$. Beams 3 and 2 create a nonlinear polarization at the difference frequency $\Omega$. Beam 1, at frequency $\omega$, enters the sample in a direction counterpropagating to $\omega$-$\Omega$. A portion of this beam is scattered into the phase conjugate direction however its frequency is shifted to the Stokes frequency $\omega$-$\Omega$. For vibrational frequencies ranging from 0 to 3000 wavenumbers, the corresponding phonon $\vec{K}$ vectors range between 37,500 $cm^{-1}$ to 34,500 $cm^{-1}$. Normally this type of interaction is weak, however, due to the resonant enhancement of the third order susceptibility at the vibrational frequency, a large scattering efficiency is obtained.

The experimental set-up is shown in Fig. (4.1). The laser pulses were obtained from a Quantel Nd:YAG laser. The temporal duration of the laser pulses are ~30 psec. at the second harmonic frequency. The maximum pulse energy used in the experiment is 10 mj. at 532 nm. Thirty percent of the laser was split to create two 532 nm laser pulses. The remaining energy was used to pump a 5 cm. continuum cell containing $H_2O$ . The resulting white light generated from the continuum cell spanned the entire visible spectrum [4]. The advantage of using

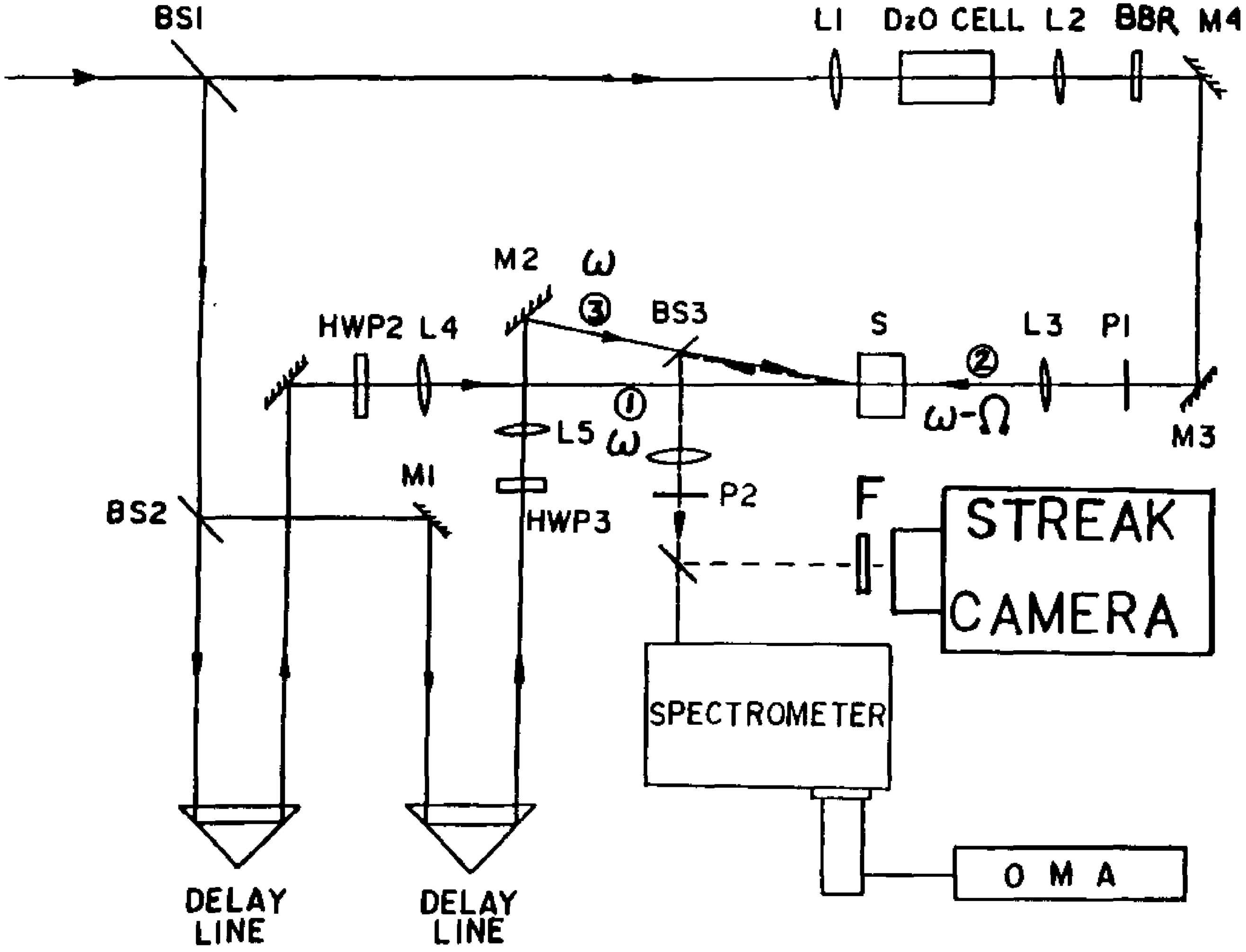

Fig. (4.1): Experimental set-up used for measuring the Raman Induced Phase-Conjugate spectrum and the temporal response of individually selected modes. BS-beam splitter, M-mirror, HWP-half wave rotator, P-polarizer, L-lense, S-sample, OMA-optical multichannel analyzer, BBR-broad band rotator, F-filter.

this continuum light source is that it will couple to all Raman active phonon modes which lie within the bandwidth of the continuum.

The two 532 nm pulses entered the $LiNbO_3$ at an angle of 10 degrees. The continuum was directed counter propagating to one of the 532 nm laser pulses. Half wave plates were inserted into the beam paths of the 532 nm pulses to control the polarizations. A broadband rotator and polarizer was inserted in the beam path of the continuum when different continuum polarizations were desired. A portion of the phase conjugate signal was directed through an analyzer and into a 1m spectrometer (~600 line/mm grating spacing) coupled with an OMA II detector system. By properly adjusting the input and output polarizations and the crystal orientation, the frequency dependence of the individual components of the nonlinear susceptibility can be measured.

## [4.3] Experimental Results

The RIPS signal was measured for various combinations of input polarization and crystal orientations. Several single shot spectra were recorded and averaged to eliminate spectral fluxuations in the continuum generation process.

A typical RIPS spectra for the condition where all three input laser pulse polarization are vertical and parallel to the crystal optic axis, or z axis, is shown in Fig. (4.2). The RIPS scattered spectra is also z polarized. The nonlinear third order susceptibility responsible for this spectra is $X^{(3)}_{zzzz}$. This spectra shows three resonantly enhanced peaks in the output spectrum, which will be shown to correspond to the three strongest Raman active $A_1(z)$ modes. The spectral asymmetry observed in the lineshapes is attributed to an interaction between the resonant and the nonresonant electronic and nuclear background cxomponents of $X^{(3)}$.

In Fig. (4.3), the input polarization of the two 532 nm. laser pulses are

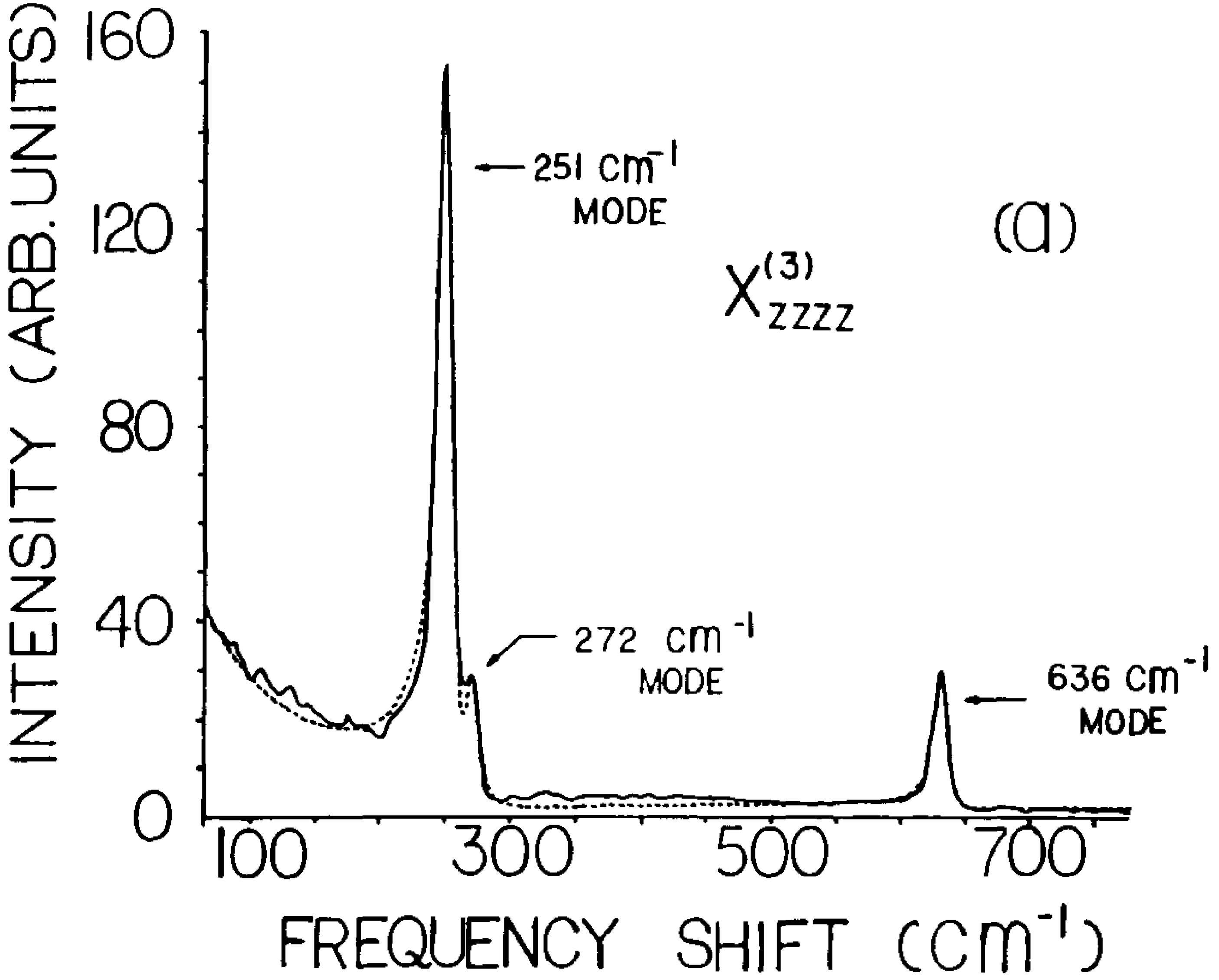

Fig. (4.2): RIPS third order susceptibility spectra for the zzzz component. The linewidths, vibrational frequencies, and oscillator strengths used in the calculation are listed in Table (4.1). The parameters used to model the continuum background are given in the text.

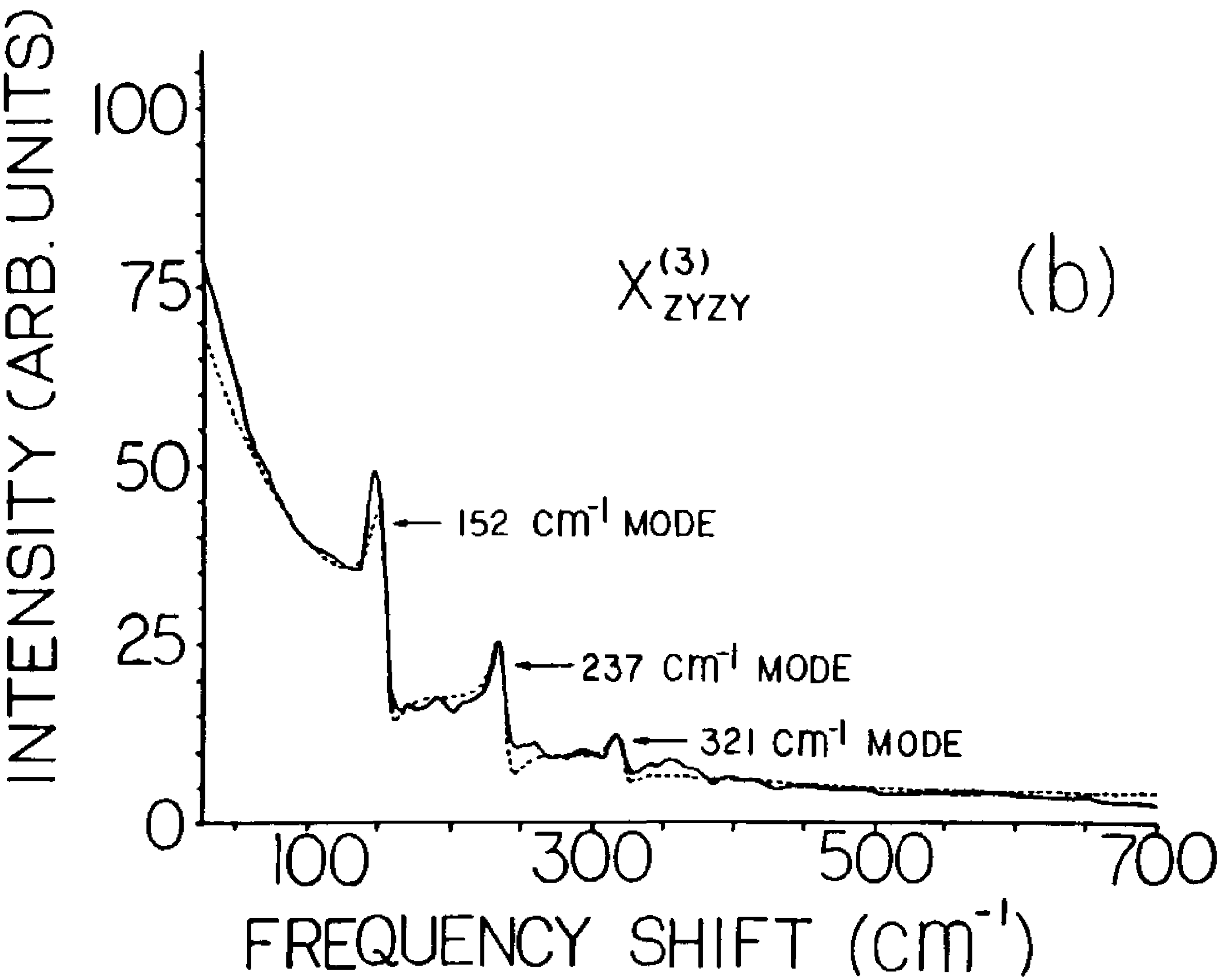

Fig. (4.3): RIPS third order susceptibility spectra for the zyzy component. The linewidths, vibrational frequencies, and oscillator strengths used in the computer calculation are tabulated in Table (4.1). The parameters used to model the continuum background are given in the text.

oriented perpendicular to the z axis. The continuum pulse and phase conjugate signal are vertically polarized along z. The third order susceptibility for this configuration corresponds to $X^{(3)}_{zyzy}$. Three Raman peaks are observable which will be shown to correspond to the strongest E type Raman active modes. The asymmetry of the lineshapes in this spectra is more pronounced. It will be shown that this is due to a decrease of the relative strengths of the Raman active modes with respect to the nonresonant electronic and nuclear background of $X^{(3)}$.

In Fig. (4.4), all three input pulses are vertically polarized, however the crystal was rotated so that the polarization vectors are parallel to the x or y axis. The output spectrum is also vertically polarized. This configuration corresponds to a scattered spectrum which is due to $X^{(3)}_{xxxx} = X^{(3)}_{yyyy}$. In this spectra, no noticible Raman lines are observed and the scatter~~ed spectrum~~ is primarily due to the nonresonant electronic and nuclear terms. The measured intensity variation of the scattered signal versus wavelength is due to the intensity variation of the continuum versus wavelength.

Other combinations of input polarization were also employed, however no additional Raman lines were observed. The salient features of these spectra showed either a flat background or a continuum background similar to the spectra shown in Fig. (4.3).

## [4.4] Theory

The third order nonlinear polarization is given by

$$P_i^{(3)} = X_{ijkl}^{(3)} E_j E_k E_l^* \tag{4.1}$$

where $X_{ijkl}^{(3)}$ is the third order susceptibility. For anisotopic materials, there are 81 elements implied by Eq. 1 which can be reduced by considering the specific crystal class. Lithium niobate belongs to the $C_{3v}$ trigonal crystal class. The number of non zero elements in $X^{(3)}_{ijkl}$ reduces to 37, with 14 independent components. These are given by:

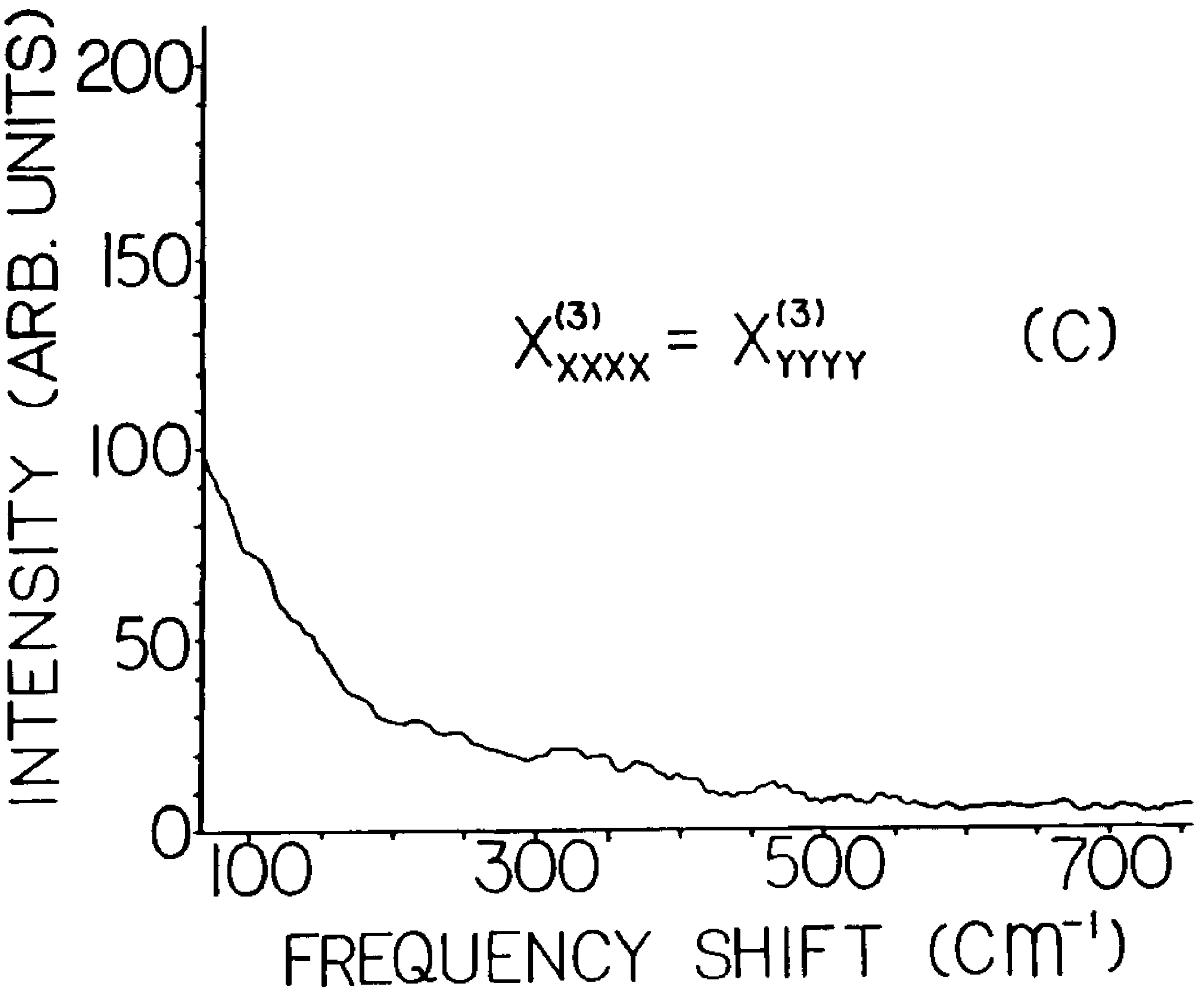

Fig. (4.4): RIPS third order susceptibility spectra for the xxxx=yyyy component. No observable resonant enhancement due to Raman vibrations is obtained with this polarization configuration.

$$zzzz, xxyy, xyyx, xyxy, yyzz, zzyy, zyzy, yzzy, yzyz, zyzy, yyyz, yyzy, yzyy, zyyy.$$

Following the notation of Hellwarth [5], the reduced form of the susceptibility, $h_{ijkl}$, can be employed. The symmetry properties of the reduced susceptibility obey the relations

$$h_{ijkl} = h_{jikl} = h_{ijlk} = h_{jilk} = h_{klij} \tag{4.2}$$

Using these relations, the fourteen independent components of $X_{ijkl}$ can be reduced to six independent components of $h_{ijkl}$. They are

$$\begin{gathered} zzzz = a, xxyy = yyxx = b, xyyx = xyxy = c, yyzz = zzyy = d \\ zyyz = yzzy = yzyz = zyzy = e, yyyz = yyzy = yzyy = zyyy = f. \end{gathered} \tag{4.3}$$

Also $xxxx = yyyy = xxyy + xyyx + xyxy$. Each of these six independent components of $h_{ijkl}$ has an associated impulse response, $h_{ijkl}(t)$, which is essentially the impulse response of the nucleus to an applied external electric field. These nuclear impulse response functions for the six $h_{ijkl}(t)$ are denoted as a(t), b(t),..., f(t).

The third order susceptibility $X_{ijkl}$ can now be given as a function of frequency in terms of the electronic, and nonresonant and resonant nuclear components, such that

$$X_{ijkl}^{(3)}(\omega_L - \omega_S) = \sigma_{ijkl} + H_{ijkl}(0) + H_{ikjl}(\omega_L - \omega_S) \tag{4.4}$$

Here, $\sigma$ is the electronic contribution, and H(0) and H( $\omega_L - \omega_S$ ) are related to the Fourier transforms of the reduced susceptibility response functions, $h_{ijkl}(t)$,

$$H_{ijkl}(\Delta) = \frac{1}{2\pi} \int_0^{\infty} h_{ijkl}(t) \exp(-i \Delta t) dt \quad where \quad \Delta = \omega_L - \omega_S \tag{4.5}$$

Here, H(0) is the frequency independent nuclear component, while $H(\omega_L - \omega_S)$ is the resonant nuclear component.

Using the above relation for $X^3$ in Eq. 2, the 14 independent third order susceptibilty components vs. frequency can be given as

$$X_{zzzz} =(\sigma+A\,(0)+A\,(\Delta)) \tag{4.6a}$$

$$X_{xxyy} =(\sigma+B\,(0)+C\,(\Delta)) \tag{4.6b}$$

$$X_{xyxy} =(\sigma+C\,(0)+B\,(\Delta)) \tag{4.6c}$$

$$X_{xyyx} =(\sigma+C\,(0)+C\,(\Delta)) \tag{4.6d}$$

$$X_{yyzz} =X_{zzyy} =(\sigma+D\,(0)+E\,(\Delta)) \tag{4.6e}$$

$$X_{zyyz} =X_{yzzy} =(\sigma+E\,(0)+E\,(\Delta)) \tag{4.6f}$$

$$X_{yzyz} =X_{zyzy} =(\sigma+E\,(0)+D\,(\Delta)) \tag{4.6g}$$

$$X_{yyyz} =X_{yyzy} =X_{yzyy} =X_{zyyy} =(\sigma+F\,(0)+F\,(\Delta)) \tag{4.6h}$$

In these equations $\sigma$ is the electronic contribution and the quantities A,B,..F, are the Fourier transforms of the nuclear response functions for the six independent components of the reduced susceptibility $h_{ijkl}$, with 0 and $\Delta$ as the frequency independant and dependant components, respectively. By measuring the RIPS spectra versus frequency with properly aligned input and output polarizations, specific components of the third order susceptibility can be measured. Vibrational frequencies, linewidths, and relative strengths of the resonant and nonresonant components can also be determined.

## [4.5] Discussion

The expressions in the above equations can be related to the standard Raman tensor $R_{\sigma\rho}$, to verify the selection rules and determine the symmetry type of the optical phonon modes which are being coherently driven in the RIPS technique. For LiNbO$_3$, the Raman tensor $R_{\sigma\rho}$ are [6]

$$A_1(z) = \begin{bmatrix} a & & \\ & a & \\ & & b \end{bmatrix} \quad E(-x) = \begin{bmatrix} & -c & -d \\ -c & & \\ -d & & \end{bmatrix} \quad E(y) = \begin{bmatrix} c & & \\ & -c & d \\ & d & \end{bmatrix} \tag{4.7}$$

The A and E matricies denote the symmetry type of the excited phonon mode. The x,y, and z correspond to the polarization of the phonon and the coefficients a,b,c and d are the coupling coefficients between the incident electric field with polarization $\sigma$ and the scattered Stokes wave with polarization $\rho$. The scattering efficiency can be written as

$$S = \sum_{\sigma\rho} |A e^{i}_{\sigma} R_{\sigma\rho} e^{s}_{\rho}|^{2}. \tag{4.8}$$

In Fig (4.2), the input polarizations for all three input pulses are polarized parallel to the crystal optic axis, i.e., z polarized. The output polarization is also z polarized. By examining the above scattering matricies, the only term which can contribute an incident $z$ polarized wave to scatter into a z polarized Stokes wave is an $A_1(z)$ mode with coupling coefficient b.

Physically, this case corresponds to the creation of a coherent phonon population by the production of an intensity grating due to the interference of $\omega_L$ and $\omega_S$. The phonon $\vec{k}$ vector is identical to the grating $\vec{k}$ vector, i.e.,

$$\vec{k}_{grating} = \vec{k}_{phonon} = +(\vec{k}_{laser} - \vec{k}_{stokes}) \tag{4.9}$$

This intensity grating is not static as in the conventional degenerate phase conjugation scheme. It drifts with a velocity, $\vec{v}$, which is a function of the frequency difference $\omega_L - \omega_S = \Omega$, and the crossing angle of the two beams. However, the grating $\vec{k}$ vector and the velocity adjust itself so that the product equals the phonon frequency, i.e., $\Omega = \vec{v}\vec{k}$. For a crossing angle of 170 degrees in the sample, and pumping wavelengths of $\lambda_L = 530$ and $\lambda_S = 550$ nm., ($\Omega = 686$ cm$^{-1}$) typical grating wavelengths $\Lambda = 2\pi/\vec{k}$ and velocities are 271 nm. and $5.5\text{x}10^6$ m/s, respectively. The phonon polarization for this situation is also z polarized due to the polarization of the interfering laser pulses and the moving intensity grating.

In the four wave mixing terminology, this scattering takes place through

$$X^{(3)}_{zzzz} = (\sigma + A(0) + A(\Delta))$$

where $\sigma$ and A(0) are the nonresonant components of the susceptibility, $X^3_{NR}$, and A($\Delta$) is the resonant component, $X^3_{RES}$. In Fig. (4.2), the resonances due to A($\Delta$) are clearly observable. In addition, an interference between $\sigma$, A(0), and A($\Delta$) is observed, which gives rise to the asymmetric line shapes in the scattered spectra. The variation of the nonresonant background is due to the variation of the continuum pulse, $E_2$ versus wavelength. The fitting to the spectra will be described in the next section to determine the values of $\sigma$, A(0), and A($\Delta$).

The spectra in Fig (4.3) utilizes input polarizations of of $E_1$=y, $E_2$=z, $E_3$=y, with an output polarization $E_4$=z. The only possible modes which can scatter a y polarized laser wave to a z polarized stokes wave are the E type phonon modes, with a coupling coefficient $R_{yz}$=d. The E modes have polarizations which lie in the x,y plane. This can be understood by examining the instantaneous electric field which is produced by the interference of the pumping stokes and laser waves. Since these two pulses are orthogonally polarized, no real intensity modulation is created. The intensity distribution is uniform, however the instantaneous electric field polarization created by $E_L$ and$E_S$ rotates in a plane perpendicular to $\vec{k}_L - \vec{k}_S$. This rotating motion occurs at a frequency $\omega_L+\omega_S$. However, there is a low frequency modulation im~~pressed on~~ this motion at $\omega_L - \omega_S = \Omega$ This low frequency modulation is responsible for the displacement of the atoms in the plane perpendicular to the z axis. This motion creates phonons polarized in the x,y plane. The spectra in Fig. (4.3) are due to E type phonon modes. This orthogonal polarization scheme becomes a way for selectively driving E type phonon modes. The motion of the displaced atoms induces a change in the nonlinear refractive index. Once there is a periodic modulation of the refractive index established, the concept of the dynamical moving grating can then be used as a physical description for the light scattering process.

Relating the spectra of Fig. (4.3), to the nonlinear third order susceptibility shows that terms similar to yzyz= zyzy are responsible for the scattered spectrum. This component is related to $\sigma$ + E(0)+D($\Delta$). The resonant terms are clearly observable, and are superimposed on a nonresonant background. The intereference between the resonant and nonresonant components are also observable and the interference effect is more pronounced.

In Fig (4.4), the crystal was rotated by 90 degrees, with the input polarizations oriented in the same fashion as in the spectra of Fig (4.2), i.e., vertically polarized. The scattered spectra is also vertically polarized. This polarization configuration couples the scattered wave to the input laser pulses through xxxx=yyyy.

With this input and output polarization configuration, no noticible resonantly enhanced vibrational lines are observed. In the four wave mixing notation, this spectrum is produced through the coupling coefficient of $X^3_{xxxx}=X^3_{yyyy}$. Since

$$X_{xxxx}=X_{yyyy}=X_{xxyy}+X_{xyyx}+X_{xyxy}$$

we see that the spectra in Fig (4.4) corresponds to $3\sigma + B(0) + B(\Delta) + 2C(0) + 2C(\Delta)$. Since there is no resonantly enhanced vibrational lines in the observed spectrum, we can conclude that the frequency dependent components, $B(\Delta)$ and $C(\Delta)$, which give rise to the resonant~~ly enhanced~~ vibrational lines are small. The scattered spectrum is just due to $3\sigma + B(0) + 2C(0)$, the nonresonant background terms. This spectra, since it only envolves nonresonant terms, gives a measure of the spectral distribution of the continuum. This spectra can then be used as a measure of the nonresonant background spectra which is present in both spectra of Fig (4.2) and (4.3). In this case, since $X^3_{xxxx}=X^3_{yyyy}$, the resulting scattered spectrum are identical for a 90 degree rotation in a plane perpendicular to the z axis. However, when comparing the xxxx and yyyy spectra to the standard Raman tensor, some difficulty arises in determining the standard Raman coupling coefficient. This is easily seen by the fact that the xxxx spectrum gives information about phonons which are $\hat{x}$ polarized, i.e., E(-x) modes, where the incident and scattered light is also x polarized. This type of interaction is not allow by the selection rules as seen from Eq. (4.7). However, the yyyy spectrum gives information about phonons which are y polarized, i.e., E(y) modes, where the incident and scattered light is y polarized. This type of interaction is allowed by the selection rules in Eq. (4.7), where the coupling coefficient $R_{\sigma\rho}$ is 'c'. In order to obtain a better understanding and interpret the experimentally measured spectrum, the previously measured spontaneous Raman spectrum can be consulted [7]. The spectra in [7] show two weak modes at 610 $cm^{-1}$ and 878 $cm^{-1}$ for a polarization configuration which allows Raman scattering through E(y) type phonon modes with coupling coefficient $R_{\sigma\rho}=c$. Both of these modes have been identified by [7] as mixed phonon mode. These modes are most likely not observed in our spectrum due to the small signal intensity produced by these modes and the weak continuum pulse which is used to drive these modes. In addition, the mixed modes are probably less effective than the pure TO modes which are excited in this experiment. These arguements offer a possible explanation why no vibrational lines are observed in our spectrum as compared to the results of [7]. A definitive explanation however requires more depth in theory.

## [4.6] Spectral Analysis

In order to extract physical parameters from the observed experimental spectra, a suitable model is proposed for the nonlinear third order susceptibility. Since the experiment measures the resonant enhancement due to nuclear motions, a sum of Raman lorentzian lineshapes is assumed:

$$X_{RIPS}^{(3)}(\omega_L-\omega_S)=X_{NR}^{(3)}+\sum_{i=1}^{N}\frac{a_i}{(\omega_L-\omega_S-\Omega_i)+i\Gamma_i} \tag{4.10}$$

where

$$X_{NR_{ijkl}}^{(3)}=\sigma_{ijkl}(0)+H_{ijkl}(0) \tag{4.11}$$

and

$$H_{ijkl}(\omega_L-\omega_S)=\sum_{i=1}^{N}\frac{a_i}{(\omega_L-\omega_S-\Omega_i)+i\Gamma_i}. \tag{4.12}$$

In these equations, $a_i$, $\Omega_i$, and $\Gamma_i$ are the oscillator strength, vibrational frequency and linewidth (HWHM) of the ith mode, and $X^3_{NR}$ is the nonresonant background contribution which is composed of both electronic and nuclear contributions. The scattered signal is proportional to $|X^{(3)}|^2$.

It is interesting to note the different contributions which give rise to the scattered spectra. The first type of contribution occurs from the purely nonresonant background terms, i.e., $X_{NR}^{(3)}$. The second type of processes contributes an interference term which is due to the interaction between the nonresonant background and individual vibrational resonant terms, i.e., $X_{NR}^{(3)}$ and $a_i$. The third type of contribution comes from individual resonances, $a_i$, and the fourth type of term comes from an interference between two different resonant modes, $a_i$ and $a_j$.

Using the spectra of Fig. (4.4) as a measure of the frequency variation of the nonresonant background and continuum variation for $X_{NR}^{(3)}$ in Eq. (4.10), the spectra of Fig. (4.2),(4.3), can modeled by varying the relative oscillator strengths, vibrational frequencies, and linewidths.

The resulting theoretical spectra using the above model is shown as the dotted curves in Figs. (4.2),(4.3). The nonresonant background due to the continuum variation versus wavelength was modeled as exponential "wings", after the spectra in Fig. (4.4). An additional D.C. background component was also added to the nonresonant background.

In Fig. (4.2), the vibrational frequencies which were used in the calculation were $\Omega$=251 $cm^{-1}$, 272 $cm^{-1}$, and 636 $cm^{-1}$. These frequencies are in excellent agreement with previously measured values [7,8]. The relative strengths of these three vibrational frequencies are $|a_1|$=64, $|a_2|$=30, and $|a_3|$=32. The value of the exponentially varying spectra was ~4.75 at $\Omega$=100 cm$^{-1}$ and the d.c. term was 1.0. The value of the continuum linewidth is 165 cm$^{-1}$. The linewidths used are $\Gamma_1$=6 $cm^{-1}$, $\Gamma_2$=7.5 $cm^{-1}$, and $\Gamma_3$=6 $cm^{-1}$. The extracted values for the linewidth and vibrational frequencies are in good agreement with previously measured values [7,8]. The extracted values from the computer fit are tabulated along with the previously measured values in Table (4.1), for comparison.

From these linewidths, the dephasing times for these vibrations can be obtained, assuming a homogeneously broadened Lorentzian linewidth, i.e.,

$$\pi c\,\tau=(\delta\nu)^{-1}$$

where $\delta\nu$ is the linewidth (FWHM, i.e., $2\Gamma$) in units of wavenumbers and c is the speed of light, and $\tau$ is the dephasing time. For the 636 cm$^{-1}$ mode, a $\delta\nu$ of 6 cm$^{-1}$ gives a dephasing time of ~440 fsec.

The spectra in Fig. (4.3) was also modeled in the same fashion. The vibrational frequencies used in this model are $\Omega_1=153cm^{-1}$,$\Omega_2=237cm^{-1}$, and $\Omega_3=321cm^{-1}$. These values of $\Omega$ are in excellent agreement with previously measured values [7,8]. The relative strengths of these modes are $|a_1|=14|a_2|=12$, and $|a_3|=5$. The nonresonant background was modeled with a d.c. term of 1.97, a continuum linewidth of 170 $cm^{-1}$, and a value of 6.15 at $\Omega=25$. The linewidths used in this calculation were $\Gamma_1=5cm^{-1}$,$\Gamma_2=5cm^{-1}$, and $\Gamma_3=4cm^{-1}$. These linewidths imply dephasing times of 500 fsec for the 152 and 237 modes, and 650 fsec for the 321 mode.

The values of $a_i$ used in the calculation represent the oscillator strengths and are related to the spontaneous Raman scattering cross section. If the extracted values of $a_i$ from the computer fit are normalized to a standard reference value, then a comparison can be made to the previously measured values of the spontaneous Raman scattering cross section. The extracted $a_i$'s and the previously measured spontaneous Raman scattering cross section $\sigma$ were normalized to the weakest E mode at 321 cm$^{-1}$. Comparing the extracted and normalized $\bar{a}_i$'s from the computer fit with the normalized values of the spontaneous Raman scattering cross section $\bar{\sigma}$ from Ref. 8 shows good agreement between the two measurements. These results are listed in Table (4.1) for comparison.

| Vibrational Frequencies, Linewidths, and Relative Strengths | | | | | | | | |
|---|---|---|---|---|---|---|---|---|
| This work | | | | | After Ref. 8,9 | | | |
| $\Omega(cm^{-1})$ | $\Gamma(cm^{-1})$ | $\lvert a_i \rvert$ | $\lvert \bar{a}_i \rvert$ | $\lvert a_i/X_{NR} \rvert$ | $\Omega(cm^{-1})$ | $\Gamma(cm^{-1})$ | $\sigma$ | $\bar{\sigma}$ |
| 152(E) | 5 | 14 | 2.8 | 2.8 | 151 | 4 | 3.8 | 3.95 |
| 237(E) | 5 | 12 | 2.4 | 3.2 | 237 | 4 | 2.9 | 3.02 |
| 251($A_1$) | 6 | 64 | 12.8 | 22 | 253 | 7.5 | 16 | 16.66 |
| 272($A_1$) | 7.5 | 30 | 6 | 11 | 278 | 4 | 4.0 | 4.1 |
| 321(E) | 4 | 5 | 1 | 1.6 | 321 | 3 | .96 | 1 |
| 636($A_1$) | 6 | 32 | 6.4 | 27 | 637 | 7.5 | 10 | 10.4 |

$\Omega$: Vibrational Frequency

$\Gamma$: Linewidth

$\lvert a_i \rvert$ Vibrational Oscillator Strength

$\bar{a}_i$ Normalized Vibrational Oscillator Strength

$X^{NR}$ Nonresonant Third Order Susceptibility

$\sigma$: Raman Cross Section

$\bar{\sigma}$: Normalized Raman Cross Section

Table (4.1): Table of the linewidths, vibrational frequencies, and oscillator strengths used to fit the experimentally observed Raman Induced Phase-Conjugate spectrum. Previously measured values are also listed and are in good agreement with the extracted parameters from the computer analysis. $\sigma$ is the Raman scattering cross section and $\bar{a}_i$ and $\bar{\sigma}$ have been normalized to the E mode at 321 $cm^{-1}$.

To obtain values of the nonresonant third order susceptibility, the ratio $a_i/X_{NR}$ is calculated from the computer fit. Absolute measurements of the intensities used in the experiment are difficult to obtain. However, the relative values of the resonant and nonresonant components are easily extracted from the computer fit. Typical relative values between $a_i$ and $X_{NR}$ varied between 1.6 and 27. Once the ratio of $a_i/X_{NR}$ is known, the nonresonant third order susceptibility is calculated by using the values of the spontaneous Raman cross section $\sigma$ for $a_i$.

The slight differences between the linewidths measured with this technique compared with other works can be attributed to the linewidths dependance on phonon $\vec{k}$ vector, which is due to phonon dispersion. In the previous investigations [7,8], the typical phonon wavevector is roughly equal to the incident and scattered photon wavevector, for 90 degree Raman scattering. In our investigation, the typical phonon wavevector is close to twice the photon wavevector, because the pumping pulses interact in an almost counterrunning geometry. This difference in phonon $\vec{k}$ vector puts the interaction at different points on the dispersion curve, thus giving slightly different values of the linewidths and vibrational frequencies.

## [4.7] Summary

From these experimental findings we see that $LiNbO_3$ exhibits several vibrational frequencies which couple efficiently to the third order nonlinear susceptibility. These modes can be selectively driven with proper input pulse polarizations. The resulting linewidths are relatively narrow, and exhibit subpicosecond dephasing times. Since this experiment was carried out using the phase conjugate geometry, the same concepts which are used for optical computing, image processing and pattern recognition using degenerate phase conjugation[9], can now be extended to include multispectral optical processing. Information such as images, logical data, and intensity modulated information, can now be processed with given input frequencies and polarizations, and transfered to new output frequencies and polarizations. In addition, since the physics behind the production of the dynamic transient grating relies on the creation and decay of optical phonons, which exhibit subpicosecond dephasing times, shows that $LiNbO_3$ can be used as a suitable material for performing multispectral optical processing tasks, with repetition rates in excess of one terahertz.

We have measured the nonlinear third order susceptibility of $LiNbO_3$ as a function of frequency from $\sim 75\ cm^{-1}$ to $\sim 700\ \mathrm{cm}^{-1}$, using RIPS. Six resonantly enhanced peaks were observed in the phase conjugate output spectrum. Typical enhancement factors ranged from 5 to 30 times. The signal peaks were consistant with previously measured vibrational spectra. Raman selection rules were verified, and specific components of the third order susceptibilty were identified with the corresponding Raman spectrum. The output spectrum was modeled using a sum of Raman oscillators along with a nonresonant background term. Relative strengths of the individual components were obtained, along with the vibrational frequencies and the linewidths by fitting the experimental spectra. Values of the nonresonant component of the third order susceptibility are extracted from the analysis. The extracted linewidths imply subpicosecond dephasing times. This shows that $LiNbO_3$ has the potential to be used as a multispectral optical processor with large nonlinearities, $\sim 30$ times $\chi_{NR}^{(3)}$, with an ultrafast response time less than a picosecond.

## Notes

[1] Shen, Y. R., Principles of Nonlinear Optics, Wiley Interscience, N.Y., (1985)

[2] Saha, S. K., and Hellwarth, R. W., Raman Induced Phase Conjugation Spectroscopy, Phys. Rev. A., Vol. 27, No. 2, 919, (1983)

[3] Dorsinville, R., Delfyett, P. J., and Alfano, R. R., Picosecond Raman Induced Phase Conjugation in Liquids and Solids, Appl. Optics, Vol. 26, No. 17, (1987)

[4] Dorsinville, R., Delfyett, P. J., and Alfano, R. R., Generation of 3 psec Pulses by Spectral Selection of the Continuum Generated by a 25 psec Second Sarmonic Nd:YAG Laser Pulse in a Liquid, Appl. Optics, Vol 27, No. 1, 16, (1988)

[5] Hellwarth, R. W., Third Order Optical Susceptibilities of Liquids and Solids, Prog. Quant. Electr., Vol 5, (1977)

[6] Loudon, R., The Raman Effect in Crystals, Adv in Phys., Vol 13, 423, (1964)

[7] Barker A. S., and Loudon, R., Dielectric Properties and Optical Phonons in $LiNbO_3$, Phys Rev Vol 158 No 2 433, (1967)

[8] Kaminow, I. P., and Johnston, W. D., Jr., Quantitative Determination of Sources of the Electro-Optic Effect in $LiNbO_3$ and $LiTaO_3$, Phys. Rev., Vol. 160, No. 3, 519, (1967)

[9] Fisher, R., Optical Phase Conjugation, Academic Press, N.Y., (1983)

# CHAPTER 5

# PULSE SHORTENING USING CONTINUUM GENERATION

## [5.1] Introduction

The broadband optical source which is used as the input Stokes radiation as beam 2 in the RIPS technique, is the key element for obtaining phase matched Raman spectra spanning thousands of wavenumbers. This unique source has been studied to determine its spectral and temporal characteristics. This information is important because the propteries of the broadband source effects the experimentally measured spectrum and time resolved measurement. It is the purpose of this chapter of the thesis to show that the resulting white light spectrum used as beam 2 also has a dramatically decreased pulse duration. This can lead to complicated results when performing the pump-probe convolutional technique.

## [5.2] History

High power ultrashort light pulses propagating in a condensed medium can experience self-phase modulation (SPM) and parametric mixing, leading to the generation of a broadband light continuum [1]. Recent theoretical analyses have concluded that the Stokes and anti-Stokes shifts should appear in the leading and trailing edge of the pump pulse, respectively [2,3,4]. This result was supported by experimental studies where the temporal location of various parts of the continum was determined using the autocorrelation [5] and streak camera [6,7] methods in both the femtosecond and picoseconnd regimes. Gomes et al. [8] demonstrated a pulse compression technique based on the spectral and temporal distribution of an SPM broadened pulse in a fiber. According to their analysis, since the Stokes and anti-Stokes shifts are proportional to the intensity gradients on the sides of the pulse. A window within the broadened spectral profile should eliminate the wings of the generated pulse where the high and low frequency components are located. They obtained a threefold shortening from 80 psec pulses to 30 psec utilizing an Nd:YAG laser broadened from 0.3 to 4 A after propagation through 125 meters of optical fiber with a monochromator as a spectral window. Recently, the continuum generated in $CCl_4$ by a weakly focused 8 psec laser pulse was measured by a 2 psec resoultion streak camera at several wavelengths [9]. The continuum was found to have a shorter duration than the pump (~ 6 psec) and to be generated over a local spatial domain in the liquid cell.

In this chapter, a method is demonstrated to generate pulses down to 3 psec using a continuum spanning 140 nm generated in $D_2O$ by an intense 25 psec Nd:YAG second harmonic laser pulse. This achieves both pulse shortening and wide tunability. The duration of the compressed pulse was measured using a 2 psec streak camera system.

## [5.3] General Theory of Self-Phase-Modulation

One of the principle physical mechanisms for the continuum generation is self-phase modulation (SPM). This effect was discovered by Alfano and Shapiro in 1970. Other nonlinear processes occur simultaneously and contribute to the continuum generation. These process are four wave parametric mixing, self focusing, and avalanche ionization. Each of these processes have distinct features which are characteristic to the individual processes.

The technical importance for self phase modulation is that it is the key mechanism which is required for ultrashort pulse generation by optical pulse compression techniques [10]. The SPM mechanism provides the frequency sweep and bandwidth which is necessary for pulse compression.

In the SPM effect, the modulation of the phase of the laser pulse occurs through the intensity dependent index of refraction. As an intense laser pulse propagates through a nonlinear material, the electric field distorts the atomic configuration of the material, which results in a change in the optical index of refraction via the nonlinear third order susceptibility. The electric field of the laser beam in the time domain after traveling a distance z in the medium is given by

$$E(t)=\tfrac{1}{2}E_0\exp[-i(\omega_L t-n(t)z\,\omega_L/c)]+c.c. \tag{5.1}$$

where $E_0(t)$ is the electric field envelope of the laser pulse, $\omega_L$ is the laser frequency, and $n(t)$ is the time varying index of refraction. For istropic materials, the index of refraction becomes intensity dependent [11], i.e.,

$$n(t)=n_0+n_2E(t)^2 \tag{5.2}$$

The intensity dependent term in the index of refraction modulates the spectral intensity by modulating the instantaneous phase of the laser pulse.

In the SPM effect, the spectrum which is generated is proportional to the derivative of the phase of the input laser pulse. The instantaneous frequency dictates that different spectral components are produced at different times according to the equation [11]

$$\omega_{inst}(t)=-\frac{\partial\phi}{\partial t} \tag{5.3}$$

with $\phi$ given as

$$\phi(t)=\omega_L t-n(t)\omega_L z/c \tag{5.4}$$

where z is the interaction length, $\omega_L$ is the input laser frequency, and c is the speed of light. With n(t) given as

$$n(t)=n_0+n_2I(t) \tag{5.5}$$

where $n_0$ and $n_2$ are the linear and nonlinear indices of refraction, respectively, and substituting into Eqs. (5.4) and (5.5), gives

$$\omega_{inst}(t)=\omega_L-n_2\omega_L\frac{z\,dI(t)}{c\,dt} \tag{5.6}$$

This equation shows that if frequency filters are used to select a portion of the generated white light, a shorten pulse results, where the temporal duration of the shortened pulse depends on the derivitive of the input laser intensity and the bandwidth of the spectral filter.

The salient features of the SPM process can be summarized by Fig. (5.1).

## [5.3] Experimental Apparatus

The experimental arrangement used to generate and measure the continuum pulse is shown in Fig. (5.2). The setup consists of the active-passive Nd:YAG laser system, the continuum generator, an optical delay, a streak camera and a temporal analyzer. The second harmonic 25 psec (~5 mJ) laser pulse was divided by a 5% reflecting beam splitter into two beams. The stronger beam was used to generate the continuum pulses. The weaker one was used as a prepulse to provide a relative time scale for the continuum pulse and to determine the pulse duration of the second harmonic pulse. The continuum was generated by focusing the laser beam with a 20 cm focal length lens into a 5 cm cell filled with $D_2O$. The continuum spanned from 450 to over 600 nm with a minimum average energy of at least 20 nJ/ nm across the spectrum. Narrowband filters were inserted after the $D_2O$ cell to select a particular spectral region. Measurements were made with 10 nm bandwidth filters at several wavelengths. The pump and prepulse beams were then combined, optically delayed, and directed into a Hamamatsu model C1587 streak camera, where the temporal delay between the two pulses was measured. The streak camera was set at a 300 psec/15 mm full sweep range. The minimum resolution of the camera is 2 psec when the streak trace is imaged with a 2.1:1 lense across a 256 channel 1 cm active area detector ( focused resolution ~4 channels ).

Figure (5.3) gives a temporal display of both the second harmonic laser pulse and the part of the continuum pulse selected by a 10 nm bandwidth narrowband filter centered at 580 nm. The pulse duration at 530 nm is ~24 psec, while the pulse derived from the continuum is clearly much shorter. The measured pulse duration (FWHM) is ~3 psec and is almost limited by the resolution of the streak

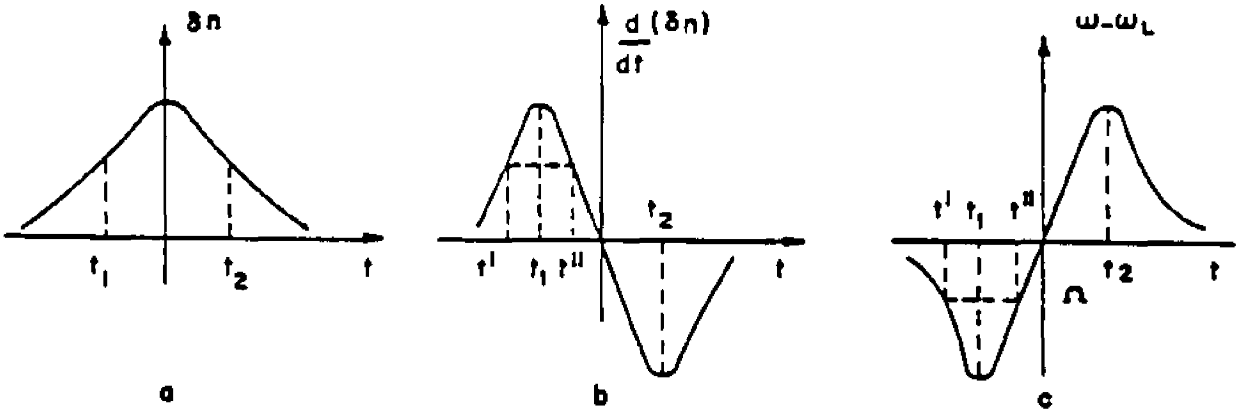

Fig. (5.1): The salient features of the SPM process.

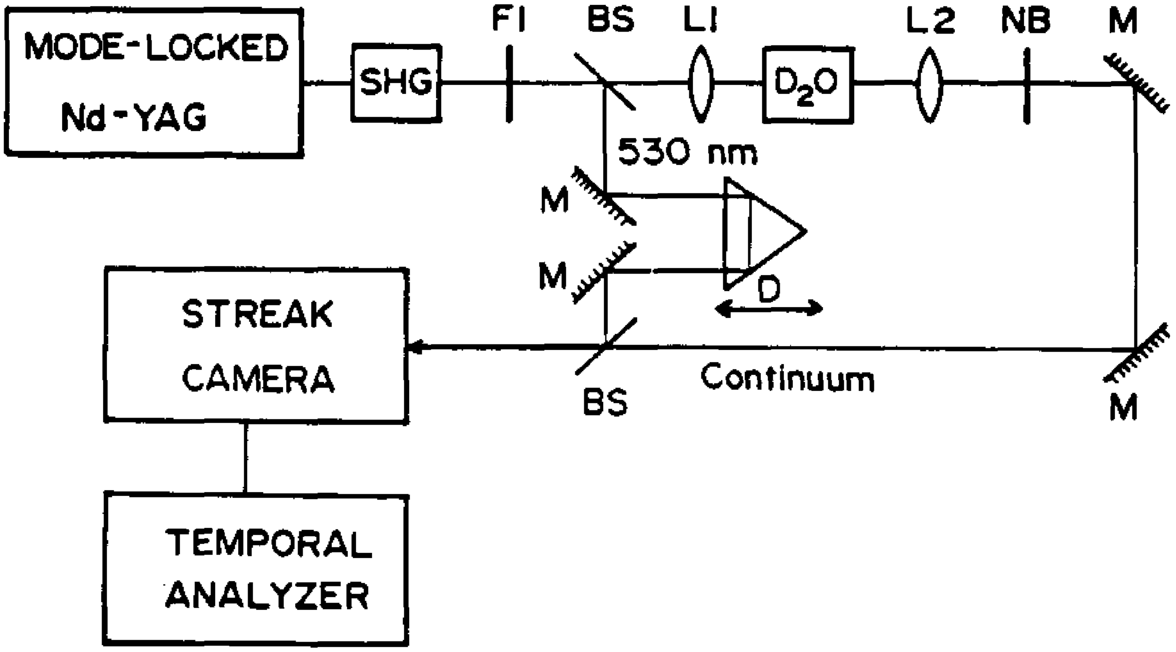

Fig. (5.2): Schematic of the experimental set up used to measure the spectral and temporal properties of the continuum source.

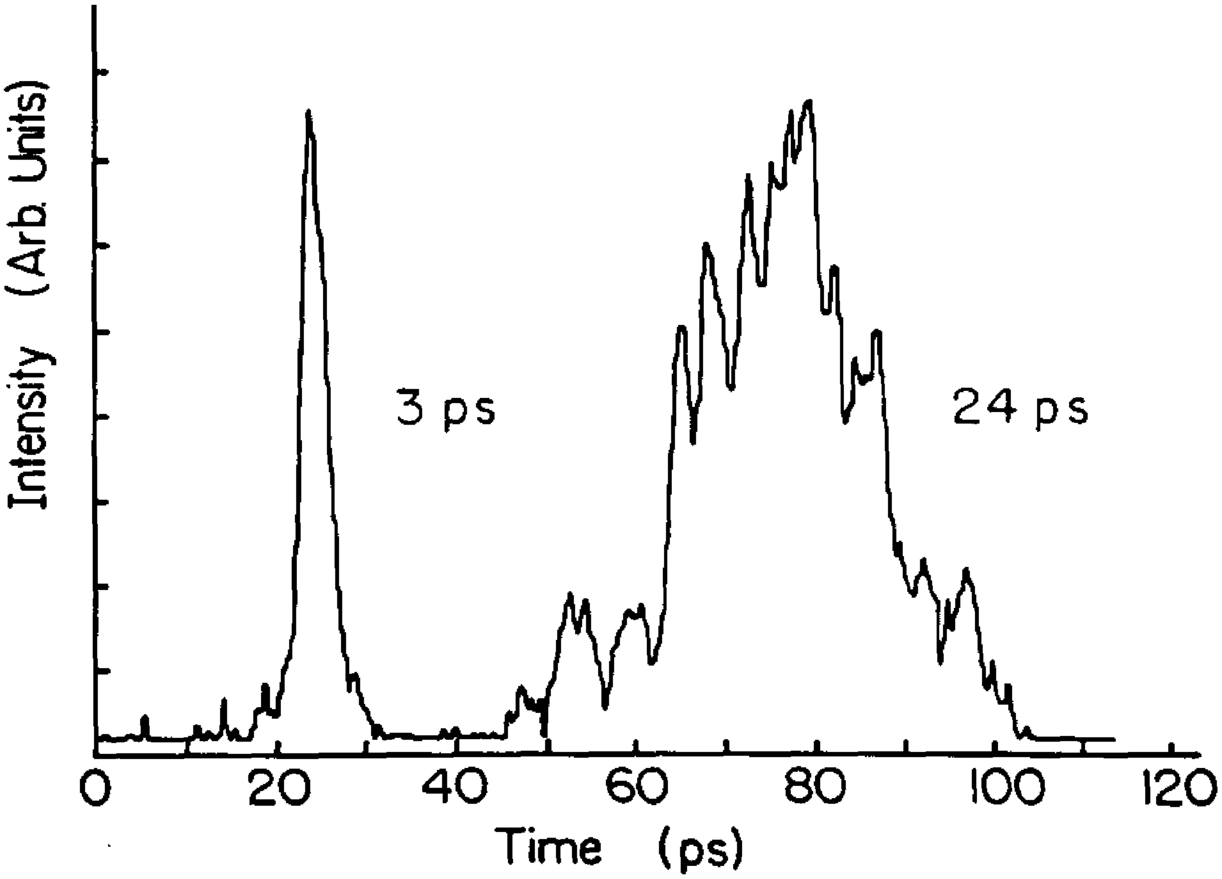

Fig. (5.3): Streak camera output of the input laser pulse and a spectrally selected portion of the continuum at 580 nm.

camera. From this, a minium compression ratio of 8 is achieved.

In Fig. (5.4) the pulse duration of the spectrally selected continuum pulse is plotted as a function of the peak transmission wavelength of different narrowband filters. Each point on the curve is the average of at least six separate measurements. No deconvolution of data for the prompt 2 psec response was performed. The pulse durations were less than 4 psec over the entire spectral range, except close to the pump laser wavelength, where the signal pulse duration was equal to the input pulse duration (25 psec). This is expected since a very small portion of the laser energy is converted into continuum with such long input pulses, and the signal at 530 consisted mainly of the laser pulse.

The temporal distribution of the continuum spectrum was determined by measuring the time delay between the spectrally selected continuum pulse and a reference pulse. The results are displayed in Fig. (5.5). The time delay was ~22 psec for a 140 nm change in wavelength as predicted by the SPM mechanism. The Stokes wavelengths led the anti-Stokes wavelengths [6]. The delay due to group velocity dispersion over a 5 cm $D_2O$ cell for the 140 nm wavelength change is ~4 psec. The remaining 18 psec is well accounted for by the SPM mechanism using a 25 psec (FWHM) pulse and the stationary phase method[6]. Furthermore, a 10 nm change in the temporal distribution curve corresponds to ~2.6 psec width matching the measured pulse duration. **This suggests that by using narrower bandwidth filters the pulse duration can be shortened to the uncertainty limit.**

It should be mentioned than an intensity dependent mechanism was also observed in the continuum generation process. This implies that parametric four wave mixing interactions are simultaneously occuring [12]. The parametric mixing process manifests itself by a temporal broadening of the selected continuum pulse with increasing input pump energy. This is consistant with a parametric mixing

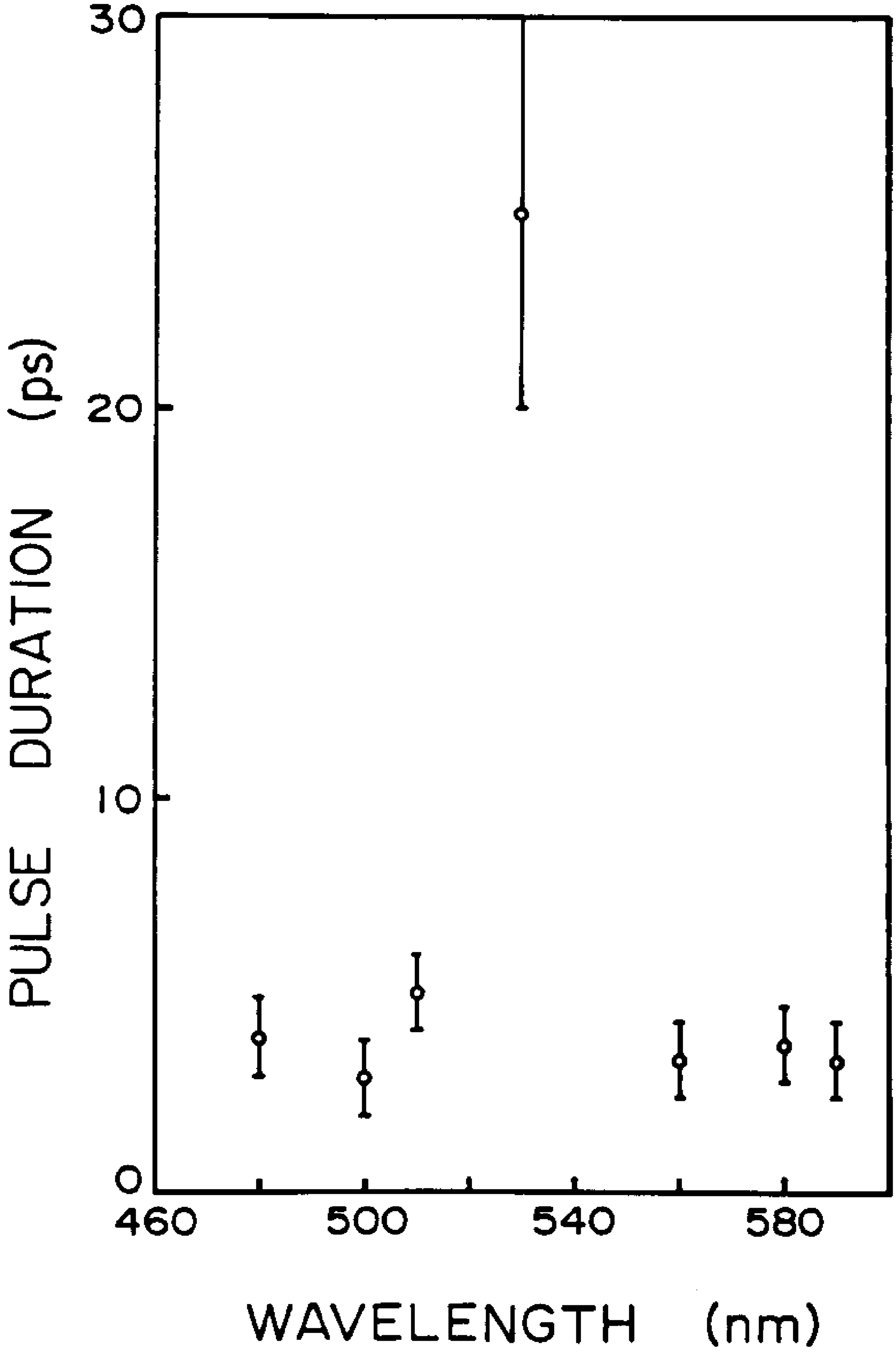

Fig. (5.4): Pulse duration of the continuum pulse plotted versus wavelength.

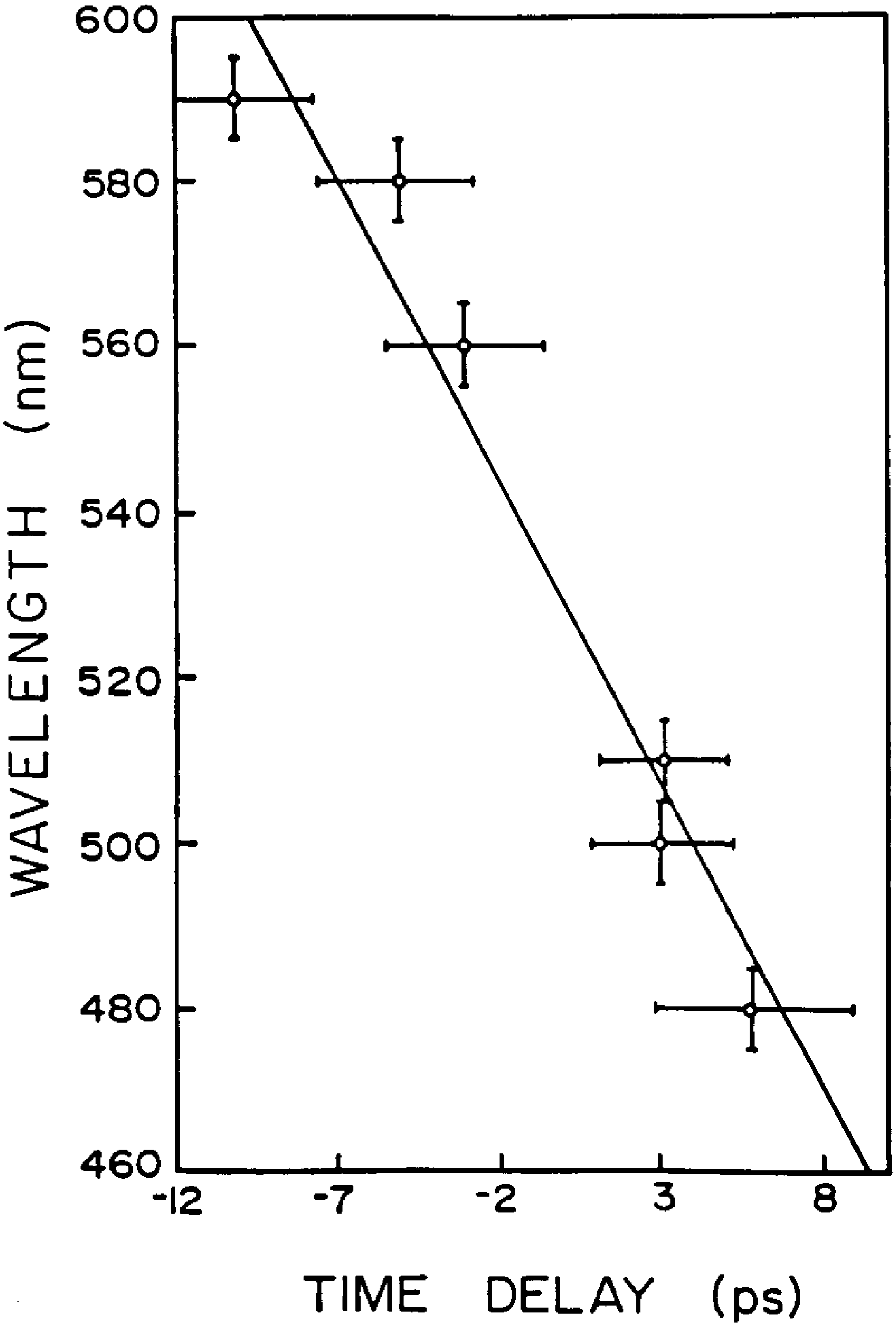

Fig. (5.5): Temporal distribution of the continuum spectrum.

process because there is an input energy threshold to overcome before continuum generation is possible. With very low input pump energy (just above threshold), the parametric mixing process only occurs at the time of peak intensity of the laser pulse. This produces a short burst of continuum because the continuum generation occurs for a fraction of the total laser pulse duration. In the opposite extreme where the input pumping energy is well above threshold, the continuum generation occurs for a longer period of time, since a larger temporal fraction of the laser pulse is above threshold. This produces a temporally broadened continuum pulse, which was consistent with experimental observations.

## [5.4] Future Technological Directions for Continuum Generation

Below are some potential applications for using the ultrashort continuum pulse for photonics technology (patent pending [13]).

- This technique can be used to generate ultrashort optical pulses (fsec) by appropriately filtering the continuum output with narrowband filters.
- Picosecond laser pulses of less than 2 psec can be generated using an initial 30 psec laser pulse.
- Optical pulses approaching the uncertainty limit can be achieved.
- The ultrashort continuum pulses can be amplified using standard laser dyes.
- The ultrashort continuum pulse can be used as a seed pulse for dye laser oscillators
- The continuum pulse can be used to pump ultrashort dye laser cavities, producing even shorter laser pulses.

## [5.5] Summary

In conclusion, a method to generate short pulses using a 5 cm $D_2O$ cell for continuum generation and arrowband filters for spectral selection was demonstrated. The pulse duration was measured by a 2 psec time resolution streak camera. Eight fold pulse shortening was obtained resulting in the generation of 3 psec laser pulses between 460 and 600 nm for 25 psec Nd:YAG second harmonic laser pump pulses. Further amplification of the short pulses using dyes is possible.

Notes

[1] Alfano, R.R., and Shapiro, S.L., Phys. Rev Lett, Vol 24, pgs 584, 592, 1217, (1970)

[2] Stolen, R. H., and Lin, C., Phys. Rev. A, Vol. 17, 1448 (1978)

[3] Yang, G.-Z., and Shen, Y. R., Opt. Lett., Vol. 9, 510, (1984)

[4] Manassah, J. T., Mustafa, M., Ho, P. P., and Alfano, R. R., IEEE J. Quant. Electron. QE-22, 78 (1986)

[5] Fork, R. L., Shank C. V., Hirlimann, C., Yen, R., and Tomlinson, W. J., Opt. Lett. Vol. 8, 1, (1983)

[6] Masuhara, H., Miyasaka, H., Karen, A., Uemiya, T., Mataga, N., Koishi, M., Takeshima, A., and Tsuchiya, Y., Opt. Comm., Vol. 4, 426, (1983)

[7] Li, Q.-X., Jimbo, T., Ho, P. P., and Alfano, R. R., Appl. Opt., Vol. 25, 1869, (1986)

[8] Gomes, A. S. L., Gouviea-Neto, A. S., Taylor, J. R., Avaramopoulos, H., and New, G. H. C., Opt. Comm., Vol. 59, 399 (1986)

[9] Ho, P. P., Li, Q.-X., Jimbo, T., Ku, Y. L., and Alfano R. R., Appl. Opt., Vol. 26, 2700, (1985)

[10] Tomlinson, W. J., Stolen, R. H., and Shank, C. V., J. Pot. Soc. Am. B1, 139, (1984)

[11] Alfano, R. R., Interaction of Picosecond Laser Pulses with Matter, (Ph.D. dissertation, Dept. of Physics, N.Y.U. 1972)

[12] Penzkofer, A., Laubereau, A., and Kaiser, W., Phys. Rev. Lett., Vol. 14, (1973)

[13] Patent # 3,782,828, Jan. 1, 1974, Patent Pending (1987)

# CHAPTER 6

# REAL TIME PHONON DEPHASING MEASUREMENTS USING RAMAN INDUCED PHASE-CONJUGATION SPECTROSCOPY

## [6.1] Introduction

In this chapter, I demonstrate a new technique which measures the vibrational dephasing of optical phonons in crystals in real time with a single laser pulse. This new technique uses RIPS in conjunction with a 2 psec resolution streak camera and a 3 psec continuum pulse. It has been used to measure the vibrational dephasing times of liquid $CS_2$ (656 $cm^{-1}$, calcite (1086 $cm^{-1}$) and $LiNbO_3$ (636 $cm^{-1}$).

## [6.2] History

In the past, researchers have relied on excite and probe techniques to measure ultrafast dynamics and kinetcs in condensed matter. The basis for the optical pump-probe techniques is that the temporal evolution of an event can be obtained by taking samples of the event at different points in time. This is accomplished by exciting a sample with one or more laser pulsed to create an optically induced change in the properties of the sample. A second weak probing pulse is directed into the sample at time delay $\tau$ which sees the change in the optical properties of the sample at that time $\tau$. By performing this experiments for all values of $\tau$ and plotting the values of the sampled optical event versus the optical probing delay time gives a measure of the relaxation rates for the physical processes involved in the light-matter interaction.

The advantage of this technique is that the ultimate temporal resolution of the optical measurement is determined by the temporal duration of the probing laser pulse duration. With the currently available ultrashort optical pulses, phenomena on the order of a few femtoseconds can be monitored.

The drawback in this technique is that thousands of laser shots must be accumulated in order to average intensity fluctuation of the lasers pulses. For performing nonlinear optical measurements, ultrashort high power lasers are necessary. Unfortunately, these lasers have relatively low repetition rates, which makes the pump-probe technique cumbersome.

Since the advent of the streak camera, single optical events can be clocked *in real time*. The main use for the streak camera in spectroscopy has been for performing time resolved fluoresence measurements and optical pulse profile measurements. Because of its ease of operation and fast temporal resolution, ~2 psec, the streak camera became the preferred tool for time resolved fluoresence spectroscopy (as compared to optical Kerr gate). However, if direct temporal measurements of the evolution of nonlinear optical excitations, such as optical phonons and molecular vibrations, are desired, the optical excite and probe technique is the only available spectroscopic tool. In the near future, streak cameras with a temporal resolution of 300 fsec will be available.

In what follows, I will describe a new nonlinear optical technique which measures the temporal evolution of coherent vibrational modes in solids and liquids, with a single laser pulse in real time.

### [6.3] Streak-camera Time-resolved Raman Induced Phase-Conjugation Spectroscopy (STRIPS) Technique

The new real time technique for measuring vibrational dephasing times in solids and liquids relies on RIPS and streak camera technology (STRIPS). The key feature which allows the direct measurement of vibrational dephasing times is the use of two pumping pulses of different temporal duration. The short pulse determines the coherent driving time. A third long probing pulse acts as a continuous probe which scatteres from the creation and relaxation of the excitation in real time. The scattered pulse envelope then contains information about the decay of the excitation. Measuring the scattered pulse shape with a streak camera then captures an image of the temporal profile of the scattered pulse shape and therefore gives information about the decay of the excitations. This situation can be exemplified by examining the schematic diagram of the process in Fig. (6.1).

In Fig. (6.1), three laser pulses are incident on the sample in the phase conjugate geometry, with $\omega_1=\omega_3=\omega_L$, and $\omega_2=\omega_L-\Omega$. In this schematic the pulse duration of beams 1 and 3 are ~30 psec and the pulse duration of beam 2 is ~2 psec.

## [6.4] Time resolution due to finite interaction regions

In the STRIPS technique, one must consider the effects which occur due to finite interaction regions. The effects are detremental for time resolved spectroscopy and complicate the measured RIPS pulse shape. This comes about because different portions of the sample are excited and probed at different times. This leads to a temporal broadening of the scattered pulse. The actual scattered pulse shape is thus a measure of the phonon dephasing time which must also be convolved over the finite interaction region. This can be seen in Fig. (6.2).

The maximum interaction length is related to the input beam diameters and crossing angle. Assuming equal beam diameters for all input beams, the maximum interaction length is given by

$$l=\frac{2d}{sin\,(\theta)}\cos\left[\frac{\theta}{2}\right]$$

Limiting the beam diameters and using large interaction angles reduces the interaction length, thus reducing the temporal broadening of the scattered pulse.

The case when $E_1$ and $E_3$ are c.w. beams and $E_2$ is a delta function illustrates how the length of the interaction region effect the temporal properties of the Raman scattered pulse.

Since both $E_1$ and $E_3$ are c.w. beams, the Raman process begins when $E_2$ enters the interaction region. The Raman light scattered from any point in the

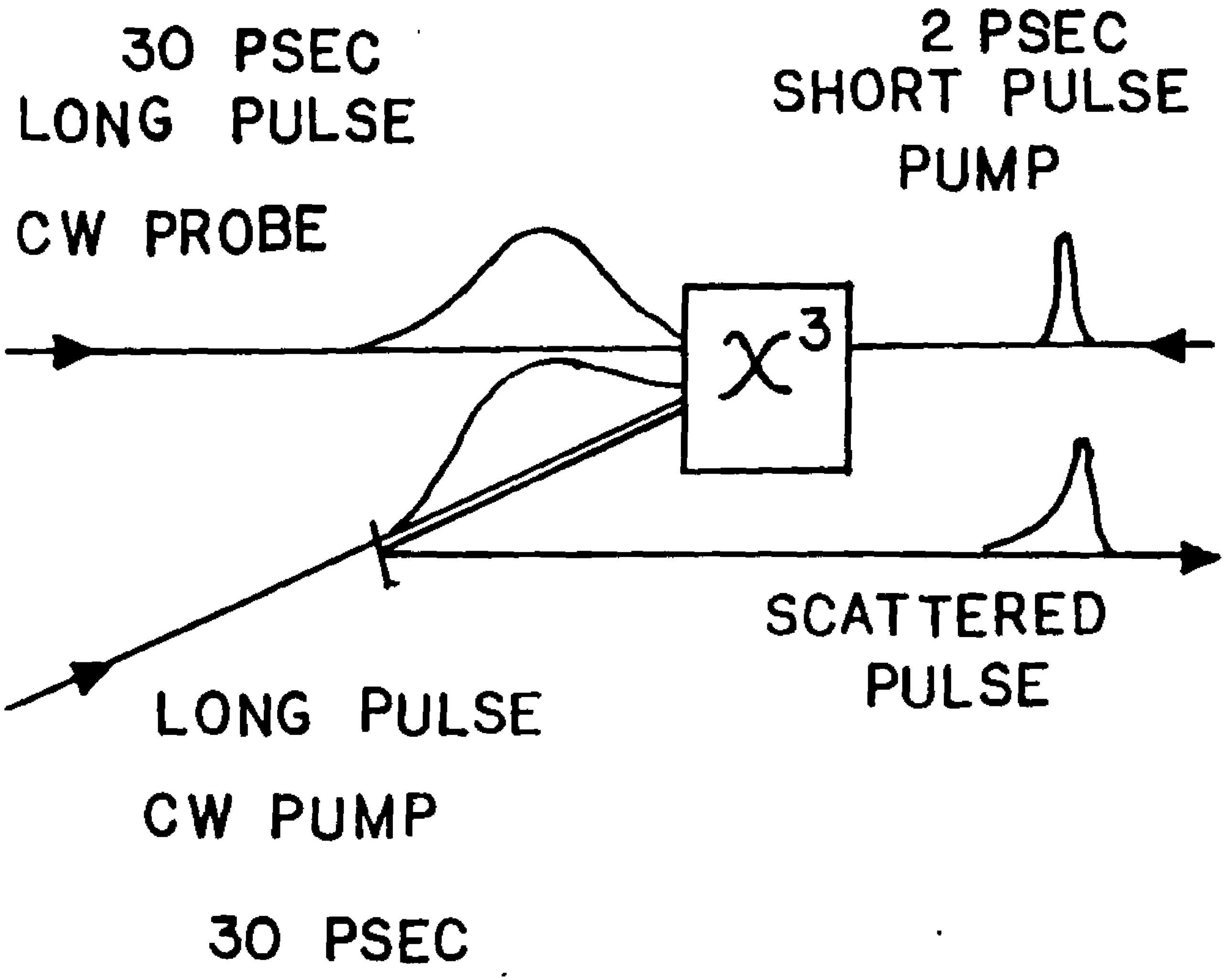

Fig. (6.1): Schematic of the STRIPS technique.

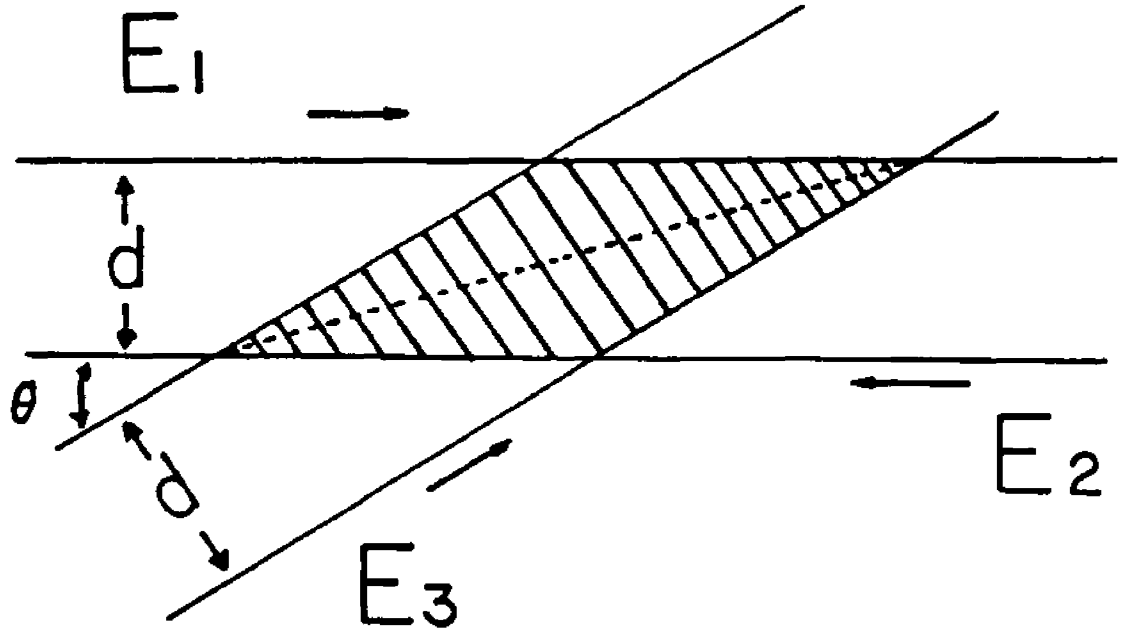

Fig. (6.2): Geometry of the overlap region in STRIPS.

interaction region follows a convolutional integral

$$P(t)=\int_{-\infty}^{t} h(\tau)\delta(t-\tau)d\tau$$

The total scattered light from the sample is obtained by summing the individual contributions. This corresponds to integrating over the interaction volume.

$$P(t)_{TOT}=\int\int_{-\infty}^{t} h(\tau,\vec{r})\delta(t-\tau,\vec{r})d\tau d\vec{r}$$

In the present experiment, the crossing angle is 10 degrees, with focused beam diameters of ~ 100 $\mu$m. This leads to a maximum interaction length of 1.1 mm which corresponds to ~3 psec, which is in good agreement with the experimental results.

Experimentally, the light beams have finite pulse durations. Adjusting their arrival times decreases the volume which contributes to the light scattering process. This reduces the temporal broadening effect. In addition, because the light scattering process is due to a nonlinear optical process proportional to the product of the three interacting pulses, the interaction region is reduced because of the transverse gaussian spatial intensity distribution. This also reduces the temporal broadening effect.

The simplest way to eliminate temporal broadening effects is to use thin samples, ~ 1 mm. This corresponds to a time of ~3 psec.

The instantaneous nonlinear polarization at time t, in the case of an infinitely thin sample, can be written as [1]

$$P(\omega_S,t)=E_1(\omega_L,t)\int_{-\infty}^{t} E_3(\omega_L,\tau)E_2(\omega_S,\tau)A(t-\tau)d\tau \qquad (6.1)$$

where A(t) is the impulse response of the material excitation. The impulse response A(t) can represent the response due nuclear motions, i.e., phonons, the response due a population of free carriers in semiconductors, etc. In our case, the temporal duration of driving term $E_3 \cdot E_2$ will be proportional to the pulse duration of $E_2$ since the pulse duration of $E_3 >> E_2$. The integral then becomes a convolution of the driving term with the impulse response. The nonlinear polarization $P(\omega_S,t)$ results from beam $E_1$scattering from the excitation represented by the integral term in Eq. (6.1). If the duration of the probing pulse is long with respect to the material relaxation time, $P(\omega_S,t)$ can be given as

$$P(\omega_S,t) = \int_{-\infty}^{t} E_2(\omega_S,\tau)A(t-\tau)d\tau \qquad (6.2)$$

In the limiting case in Eq. (6.1) where $E_1$ and $E_3$ are infinitely long, and $E_2$ is a delta function, the time evolution of the nonlinear polarization at the Stokes frequency exactly follows the impulse response of the excitation, i.e.,

$$P(\omega_S,t) = A(t) \qquad (6.3)$$

This says that the Stokes frequency components in the RIPS spectrum decay according to the decay dynamics of the vibrational modes in real time.

Experimentally, the temporal duration of the input laser pulses used as $E_1$ and $E_3$ is ~30 psec. The temporal duration of the continuum Stokes pulse is ~ 2 psec. Thus, the experimental conditions are appropriate for the approximations made in the above analysis.

## [6.5] Real Time versus Pump-Probe Technique

It is interesting to note the difference between the time delayed pump-probe technique and the single shot real time technique. In the case of the pump-probe technique the intensity of the RIPS signal is detected by a slow detector. The resulting signal is represented by

$$I_{PC} = \int_{-\infty}^{\infty} |P(\omega_S,t)|^2 dt$$

In the pump-probe technique, the measured quantity gives $I_{PC}$ versus the optical probing delay $\tau_d$. Thus $I_{PC}(\tau_d)$ can be written as

$$I_{PC}(\tau_d) = \int_{-\infty}^{\infty} \left| E_1(t-\tau_d) \int_{-\infty}^{t} E_2(\tau)E_3(\tau)A(t-\tau)d\tau \right|^2 dt \qquad (6.4)$$

In the present case, the experimental conditions imply that the inner integral approximates A(t). The outer integral convolves the probing laser pulse with the approximated impulse response. If the impulse response lifetime is much shorter than the probing pulse duration, $I_{PC}(\tau_d)$ follows the temporal profile of the probing pulse $E_1$, i.e.,

$$I_{PC}(\tau_d) \sim |E_1(\tau_d)|^2$$

This gives the well known result that the temporal evolution of the material excitation is unresolved in the pump-probe technique when the probing pulse duration is much longer than the material relaxation time.

## [6.6] Measurement of Phonon Lifetimes

In our case, the impulse response for vibrational modes can be modeled as

$$A(t) = Q(t)$$

where

$$Q(t) = Q_0 \exp(-t/T_2), \qquad t \geq 0 \tag{6.5}$$

where $T_2$ is the relaxation time. Assuming a very short continuum pulse ($E_2 \sim \delta(t)$), and very long probing and pumping pulses $E_1$and $E_3$, ($E_1$=$E_3$=a constant), in Eq. (6.1), the intensity of the signal reaching the streak camera at time t is given by

$$I_{PC}(t) = |P(t)|^2 \tag{6.6}$$

$$I_{PC}(t) = E_1^2 E_2^2 E_3^2(t) \exp(-2t/T_2) \tag{6.7}$$

For a long probe pulse of arbitrary shape, the response function of the medium is obtained by dividing the envelope of the phase conjugate signal at the Stokes frequency by the envelope of the probing pulse. The above equations show that when the nonlinear phonon response of a material is studied by using a fast detectorm the temporal shape of the phonon response function of the material can be obtained in real time. For our experimental conditions, phonon lifetimes with a duration between 2 and 25 psec can be measured, according to Eq. (6.1). In order to measure phonon lifetimes outside of this range, longer probing pulses, faster streak cameras and shorter continuum pulses are needed.

## [6.7] Experimental Results

This technique was tested by measuring the vibrational relaxation time of liquid $CS_2$ and calcite. Both of these samples have well studied vibrational modes which have relaxation times that fall within the experimentally accessible regime of the technique [3,4,5,6]. The systems temporal resolution was obtained by measuring the vibrational relaxation of one of the Raman modes of $LiNbO_3$. From linewidth measurements, the relaxation time is inferred to be in the subpicosecond regime, thus yielding the temporal resolution of the technique [7].

Figure (6.3) show a typical single shot real time streak camera measurement of the 656 $cm^{-1}$ vibrational mode of liquid $CS_2$. The dominant features displayed in this measurement is a very fast rise time, with an initial fast decay component. After the fast decay componont, a weaker and slower decay component is observed. Plotting this measurement on a semi-logarithmic scale clearly shows the two distinct components. The rise time of the event is consistant with the typical rise time of the continuum pulse $E_2$. The fast decay component is attributed to the electronic nonlinearity. The slow decay component is clearly resolvable by the straight line decay data in the semi-log plot. Extracting the decay time from the data gives a dephasing time $T_2 = 20 \pm 1$ psec. This time is in excellent agreement with previous measurements which used standard pump-probe techniques [3].

The new technique was also used to measure the dephasing of the 1086 $cm^{-1}$ line in calcite. Figure (6.4) shows a semi-log plot of the calcite phase conjugate pulse envelope at the Raman scattered Stokes frequency along with the $CS_2$ and $LiNbO_3$ Raman pulse envelopes. The features of the calcite pulse envelope are similar to the $CS_2$ with the exception that the nonlinear electronic component in

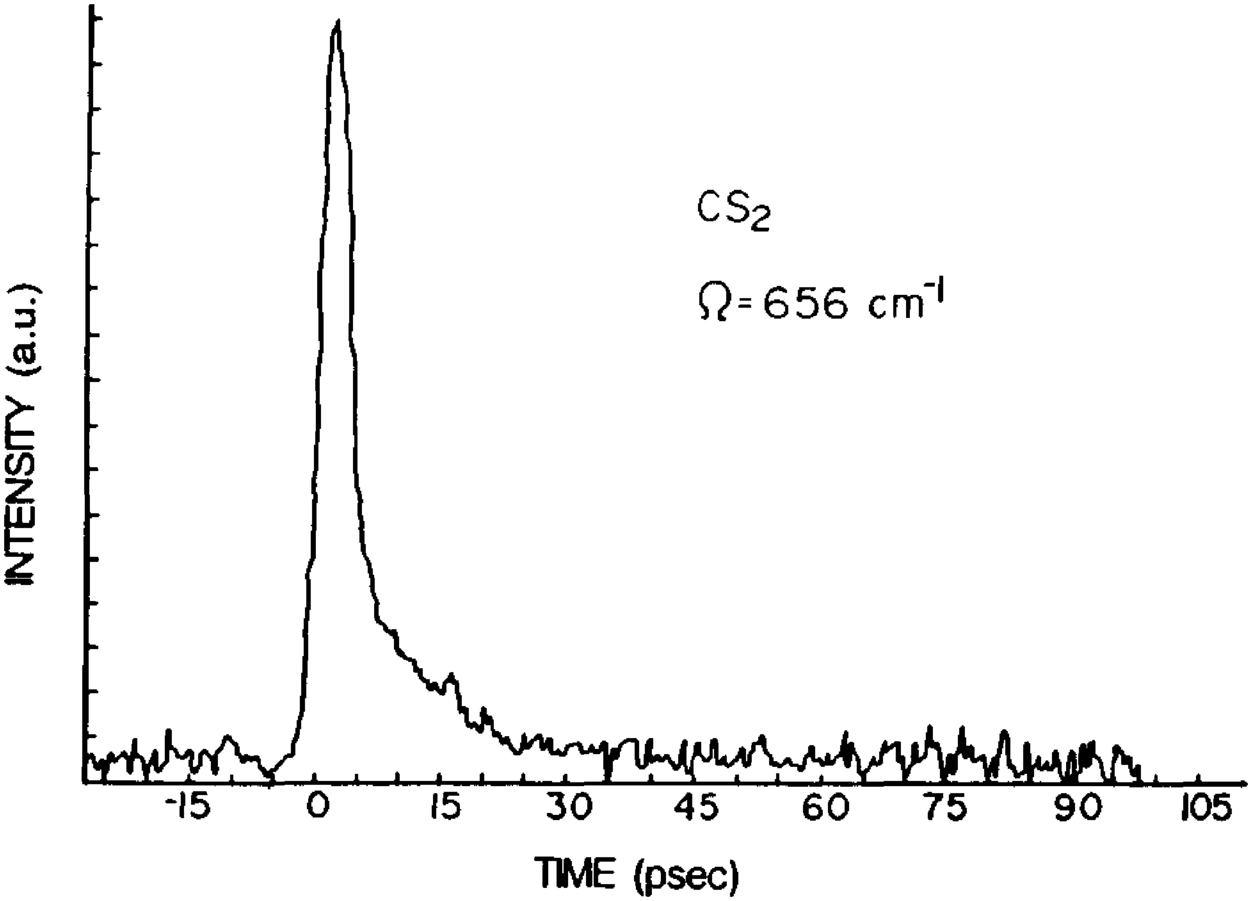

Fig. (6.3): Streak camera output using STRIPS on the 656 cm$^{-1}$ mode of CS$_2$.

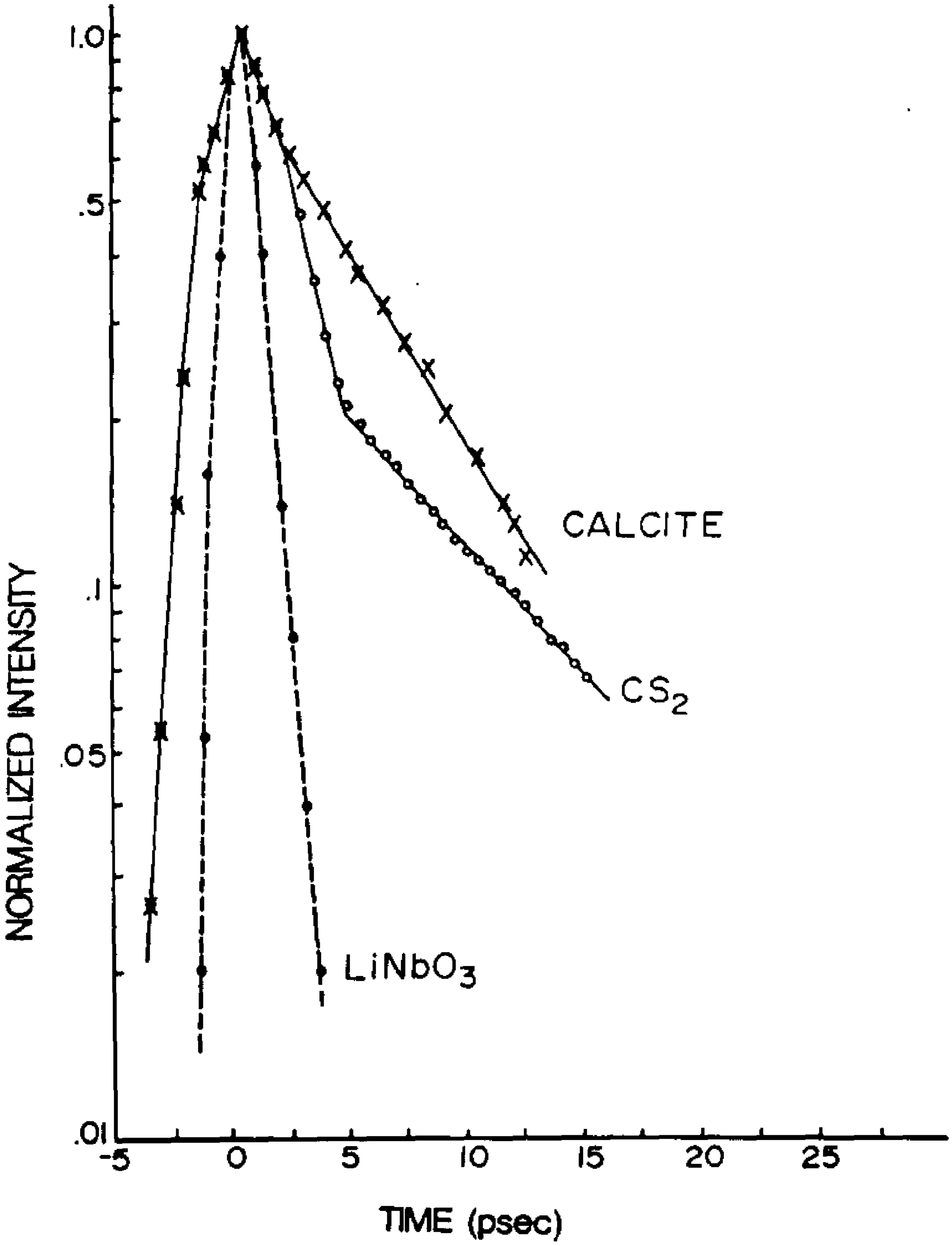

Fig. (6.4): Semi-log plot of the streak camera output from $CS_2$, calcite and lithium niobate.

calcite has a smaller contribution to the scattered pulse shape. The vibrational dephasing time for the 1086 $cm^{-1}$ can readily be extracted from the straight line data in Fig. (6.4) and gives a time of 9±1psec for the vibrational dephasing. For a homogeneously broadened Lorentzian line shape, this value for the vibrational dephasing corresponds to a spontaneous Raman linewidth given by

$$\delta\nu = (\pi c T_2)^{-1} = 1.1 cm^{-1}$$

which is in excellent agreement with the linewidth measurements at room temperature [6].

The system resolution is shown by the measurement of the 636 $cm^{-1}$ vibrational mode in $LiNbO_3$. In Fig. (6.5), the real time streak camera measurement is shown. The pulse shape shows no appreciable asymmetry, yielding an ~~unresolved~~ response. The FWHM temporal duration for this mode is ~ 2 psec, which is the temporal resolution of the streak camera system. This curve is plotted along with the $CS_2$ and calcite pulse shapes for comparison in Fig. (6.4). This single pulse displayed corresponds to a shorter than average continuum pulse, which explains the narrower pulse duration for this mode.

### [6.8] Comparison of Real Time vs. Pump-Probe Technique

It is interesting to compare the real time phonon dephasing measurements with the results which are obtained using RIPS as a pump-probe tool. In Fig. (6.6), and Fig. (6.7), are the measured intensities of the RIPS spectra in $CS_2$ and calcite respectively, plotted as a function of probe delay time. The noted feature in these plots is that the decay time is *faster* than the rise time, implying an unresolved temporal response. This type of behavior is common in nondegenerate four wave mixing (CARS) experiments, when the vibrational lifetime is shorter than the probing pulse duration [8]. This result is expected because the probing pulse duration is greater than the vibrational relaxational times for these two samples, i.e., 30 psec compared to 8 psec and 20 psec for calcite and carbon disulfide, respectively.

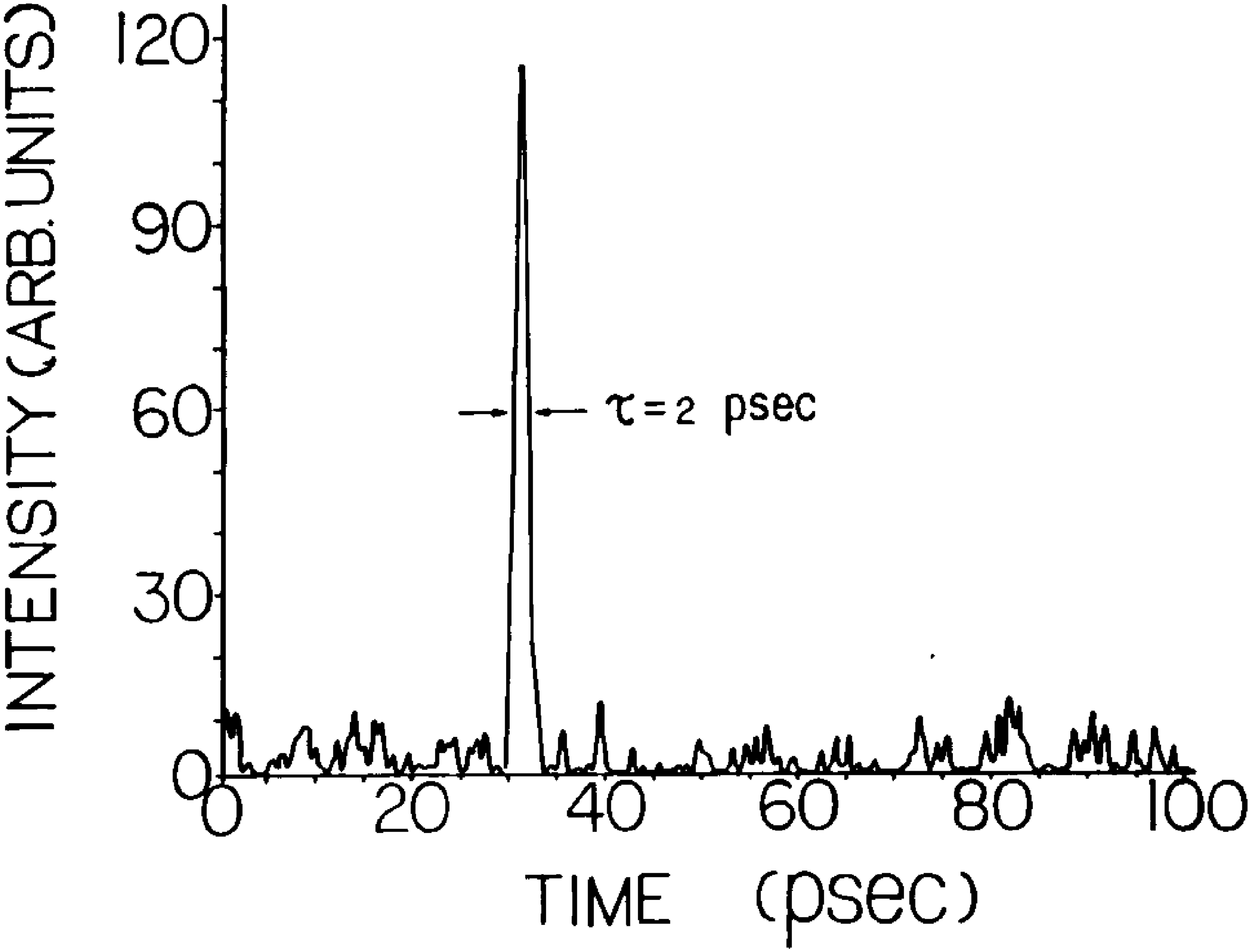

Fig. (6.5): Streak camera output using STRIPS on the 636 cm$^{-1}$ mode of lithium niobate.

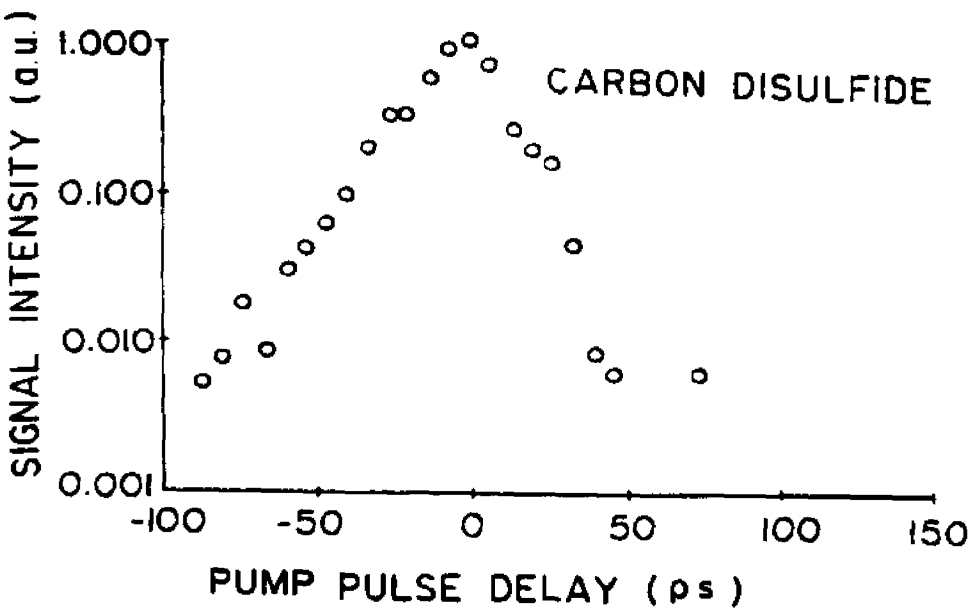

Fig. (6.6): Intensity of the RIPS signal in carbon disulfide versus beam 1 delay time.

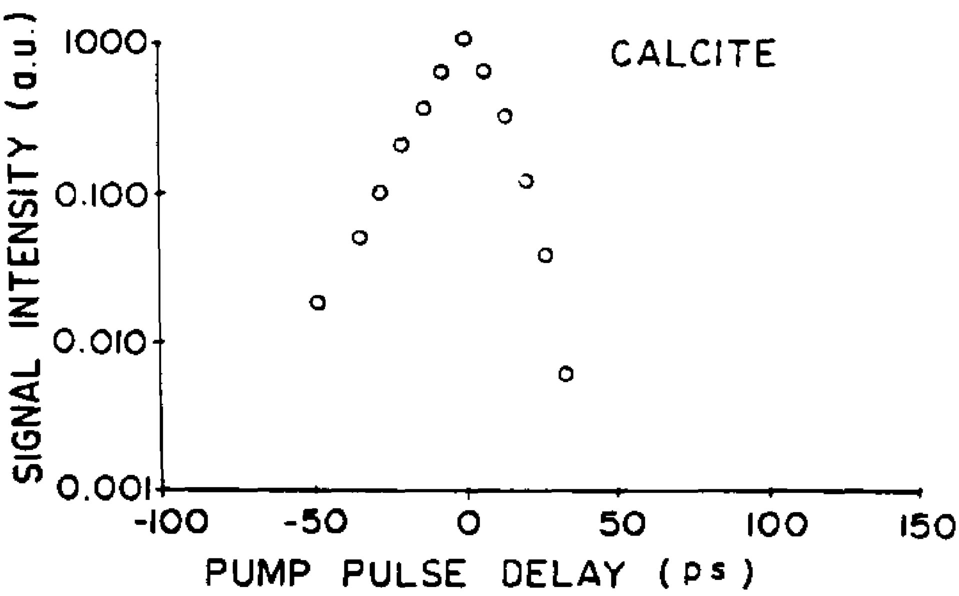

Fig. (6.7): Intensity of the RIPS signal in calcite versus beam 1 delay time.

Despite these negative results, the potential for measuring ultrashort vibrational relaxation times using the RIPS technique with shorter pulses clearly exists.

## [6.9] Summary and Conclusions

The new STRIPS technique has been used to measure the vibrational dephasing times of several different samples with a single laser pulse in real time. This technique has the advantage that both the complete Raman spectra and its corresponding temporal evolution can be studied in real time with a single laser pulse. This is most important for studies which envolve destructive testing, where only one event can be studied at a time.

In addition, since this technique uses the phase conjugate geometry, the standard techniques which are used in Fourier transform holography can now be performed in real time with many different spectral components. This new technique can be used for applications in optical logic, multispectral image processing, optical spread spectrum techniques, and multispectral image deflection.

Notes

[1] Delfyett, P.J., Dorsinville, R., and Alfano, R.R., Real-time Measurements of Phonon Lifetime using a Streak Camera Raman-induced Phase-conjugation Method, Optics Letters, Vol. 12, No. 12, 1002, (1987)

[2] Heritage, J. P., Vibrational Dephasing Measurements with cw Mode-locked Dye Lasers, Appl. Phys Lett., Vol. 34, 470, (1979)

[3] Clements, W. R. L., and Stoicheff, Raman Linewidth for Stimulated Threshold and Gain Calculations, Appl. Phys. Lett., Vol 12, No. 8, 246, (1968) 919, (1983)

[4] Laubereau, A., Wochner, G., and Kaiser, W., Direct Observation of the Relaxation Time of the Symmetric Molecular $CO_3^{-2}$ Vibration of Calcite, Opt. Comm., Vol. 14, 75, (1975)

[5] Alfano, R., and Shapiro, S., Optical Phonon Lifetime Measured Directly with Picosecond Pulses, Phys. Rev. Lett., Vol 20, 1247, (1971)

[6] Kaminow, I. P., and Johnston, W. D., Jr., Quantitative Determination of Sources of the Electro-Optic Effect in $LiNbO_3$ and $LiTaO_3$, Phys. Rev., Vol. 160, No. 3, 519, (1967)

[7] Park, K., Thermal Variation of a Raman Line Width in Calcite, Phys. Lett., Vol 25A, No. 7, 490, (1967)

[8] Laubereau, A., and Kaiser, W., Vibrational Dynamics of Liquids and Solids Investigated by Picosecond Light Pulses, Rev. Mod. Phys., Vol. 50, No. 3, 607, (1978)

# CHAPTER 7

# MULTIPHONON DEPHASING OF THE 1086 $cm^{-1}$ MODE IN CALCITE

## [7.1] Introduction

In this chapter, the dephasing time of the 1086 $cm^{-1}$ mode in calcite has been measured as a function of temperature using the new single shot streak camera technique that measures the phonon dephasing rate in real time. Phonon-phonon interaction models have been proposed and tested to explain the temperature dependence of the experimentally measured dephasing time. It is found that multiphonon splitting and scattering processes involving at least four phonons substantially contribute to the dephasing of the 1086 $cm^{-1}$ mode in calcite.

## [7.2] History

There has been considerable research devoted towards the understanding of optical phonon dynamics because of its importance to future high speed transport devices. Several techniques have been employed, which give information about the phonon linewidth, phonon frequencies, dispersion relations, symmetry type, and phonon dephasing times [1-8]. Alfano and Shapiro [5,9] and Laubereau and coworkers [6,10] were the first to utilize picosecond laser pulses to coherently drive and directly measure the dephasing time of phonons in several solids and liquids. Over the years, several groups have performed similar experiments in GaP [11,12], ZnSe [13], diamond [14], and quartz [15]. In all of the investigations, the experimental technique relied on the picosecond excite and probe method to monitor the temporal evolution of the phonons. The temperature dependence of some of these dephasing processes were also investigated and attributed to three phonon decay processes.

In this chapter, the new real time STRIPS technique is employed to directly measure the phonon dephasing time of the 1086 $cm^{-1}$ mode of calcite in real time as a function of temperature. The purpose of this work is two fold:

1) to show that three phonon anharmonic processes are not sufficient for describing the phonon dynamics of calcite, and
2) to show that depopulation dynamics are mainly responsible for the coherent dephasing of phonons in calcite.

The inclusion of four phonon processes are necessary and have been included to describe the temperature dependence of the experimentally measured dephasing time in calcite.

## [7.3] Experimental Method

The experimental method for measuring coherent optical phonon dephasing rates in real time utilizes Raman Induced Phase-conjugation Spectroscopy (RIPS) [16,17] and streak camera technology. The laser pulses were obtained from a Quantel Nd:YAG laser system. In this technique, two coherent laser pulses of frequency $\omega_1$ and $\omega_2$ are spatially and temporally coincident at 170 degrees in a 1 cm. calcite sample. This creates a coherently driven nonlinear polarization at the difference frequency $\omega_1 - \omega_2 = \Omega$, where $\Omega$ is the 1086 $cm^{-1}$ phonon frequency, and the phonon wavevector $k = 3.66 \times 10^4$ $cm^{-1}$. A third probing pulse at $\omega_1$, traveling opposite to $\omega_2$, interrogates the nonlinear polarization. This probe pulse is scattered from the nonlinear polarization into the phase conjugate direction, and is shifted to $\omega_2$. In practice, a broadband picosecond continuum pulse ~2 psec in duration [18] is used as $\omega_2$ which coherently drives all the Raman active phonon modes that have frequencies which lie within the bandwidth of the continuum, ~2500 $cm^{-1}$. Thus, the complete phase matched Raman spectra can be obtained spanning thousands of wavenumbers, with a single laser pulse [17].

To measure the dephasing rate of the coherently excited phonons, the Raman scattered phase conjugate signal is appropriately filtered to select the desired Stokes frequency and is directed into a 2 psec Hamamatsu streak camera and computer video system. In the limit of a long probing pulse ~30 psec, and a short pumping pulse ~2 psec, the scattered RIPS pulse envelope varies as $\exp(-2t/\tau_\phi)$, where $\tau_\phi$ is the dephasing time of the coherently driven phonons [19]. This technique was successfully tested by measuring the dephasing time of the 656 $cm^{-1}$ mode in $CS_2$, which was measured to be 20 psec., in excellent agreement with previously measured dephasing times [20], and linewidth measurements [21]. The resolution limit of this technique was determined to be ~2 psec by measuring the dephasing time of the 630 $cm^{-1}$ mode in $LiNbO_3$ [19], which is known to have a subpicosecond response, from linewidth measurements [22]. In the current experiment, the 1086 $cm^{-1}$ mode is spectrally selected by inserting a 10 nm. bandpass filter in the beam path of the Raman scattered pulse, before entering the streak camera. In order to determine the temperature dependence of the dephasing time for this mode, the calcite sample was situated in a Janis optical helium dewar with a temperature controller and thermocouple system. The RIPS spectra was simultaneously monitored using a Jarell Ash 1 meter spectrometer and OMA II system. The experiment was carried out by collecting several single shot dephasing events and storing the data for later analysis. The temperatures at which the experiment were performed, varied from 5K to 300K.

## [7.4] Experimental Results

At least twelve single shot RIPS decay events were recorded for each temperature and averaged to eliminate noise fluctuations in the streak camera output. Decay times of the RIPS signals were extracted from the averaged data, using a least squares fit algorithm. A typical RIPS pulse shape from the calcite sample at 10K is shown in Fig. (7.1). The RIPS pulse envelope has been modeled to fit a

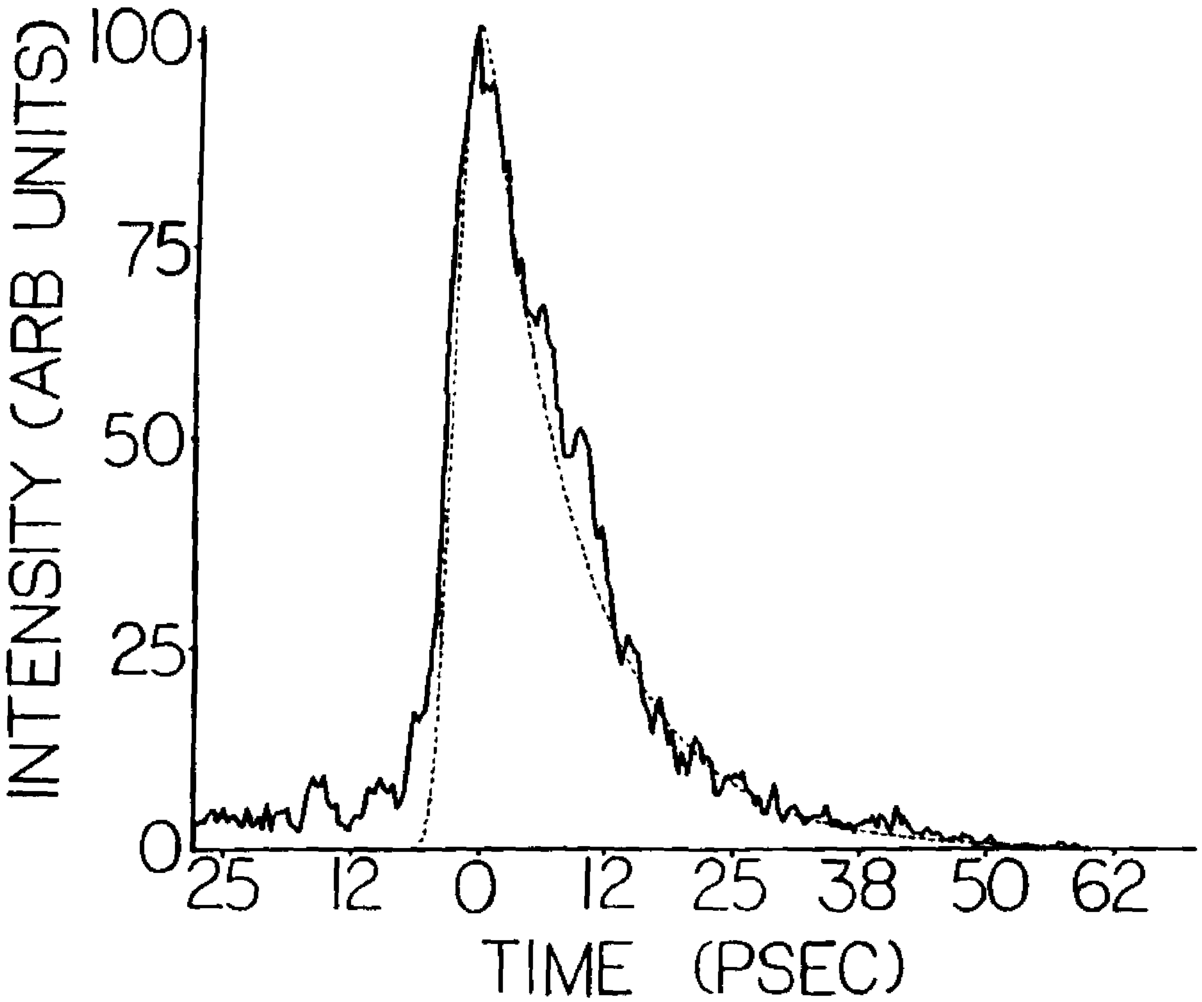

Fig. (7.1): The averaged RIPS pulse shape for the 1086 cm$^{-1}$ mode of calcite at 10 K. The dotted curve corresponds to a FWHM 3.5 psec gaussian pulse convolved with an exponentially decaying impulse response with a dephasing time $\tau_\phi$=20 psec.

single exponential with a dephasing time of 20 psec, which is shown by the dotted line.

The experimentally measured dephasing rates, $\tau_\phi^{-1}$, of the 1086 cm$^{-1}$ $A_{1g}$ mode in calcite are plotted as a function of temperature in Fig. (7.2). The salient feature in our data is a rapid rise in the dephasing rate for high temperatures. At low temperatures, less than 50K, the experimentally measured dephasing time $\tau_\phi$, of the phase conjugate signal is 20 psec. Above 50K, the decay rate of the phase conjugate signal increases, giving a dephasing time $\tau_\phi$ of 9 psec. at room temperature.

## [7.5] Theory

The phonons which are generated in this technique are coherent with a well defined wavevector $\vec{k}$ and frequency $\Omega$ determined by two interacting laser pulses. The excess population in the excited mode $\vec{k}$ greatly exceeds the thermal equilibrium number, leading to a nonequilibrium phonon distribution. The phonon distribution function becomes a sharply peaked function in both momentum and energy space. The nonequilibrium distribution thermalizes to a Boson distribution by dephasing along $\vec{k}$ and depopulation processes, leading to a direct loss of scattered light in the phase matched direction.

The relative number of coherently excited phonons to the thermally excited phonons in a small range $\Delta k$ can be easily estimated. The number of phonons generated is determined by the weaker of the two pumping beams, i.e., the continuum pulse. Assuming a 20 nJ/nm continuum pulse at the Stokes wavelength ($\lambda$=564 nm), a 1 mm$^2$ spot size, a 3 psec pulse duration, a .1% conversion efficiency to the generated phase conjugate Raman signal, and a 1 cm$^{-1}$range of $\Delta k$, which corresponds to the linewidth at room temperature, the number of coherent phonons per cm$^3$, $N_{phonon}$, is $\sim 10^9$. The density of excited optical phonon modes can be obtained from the equation

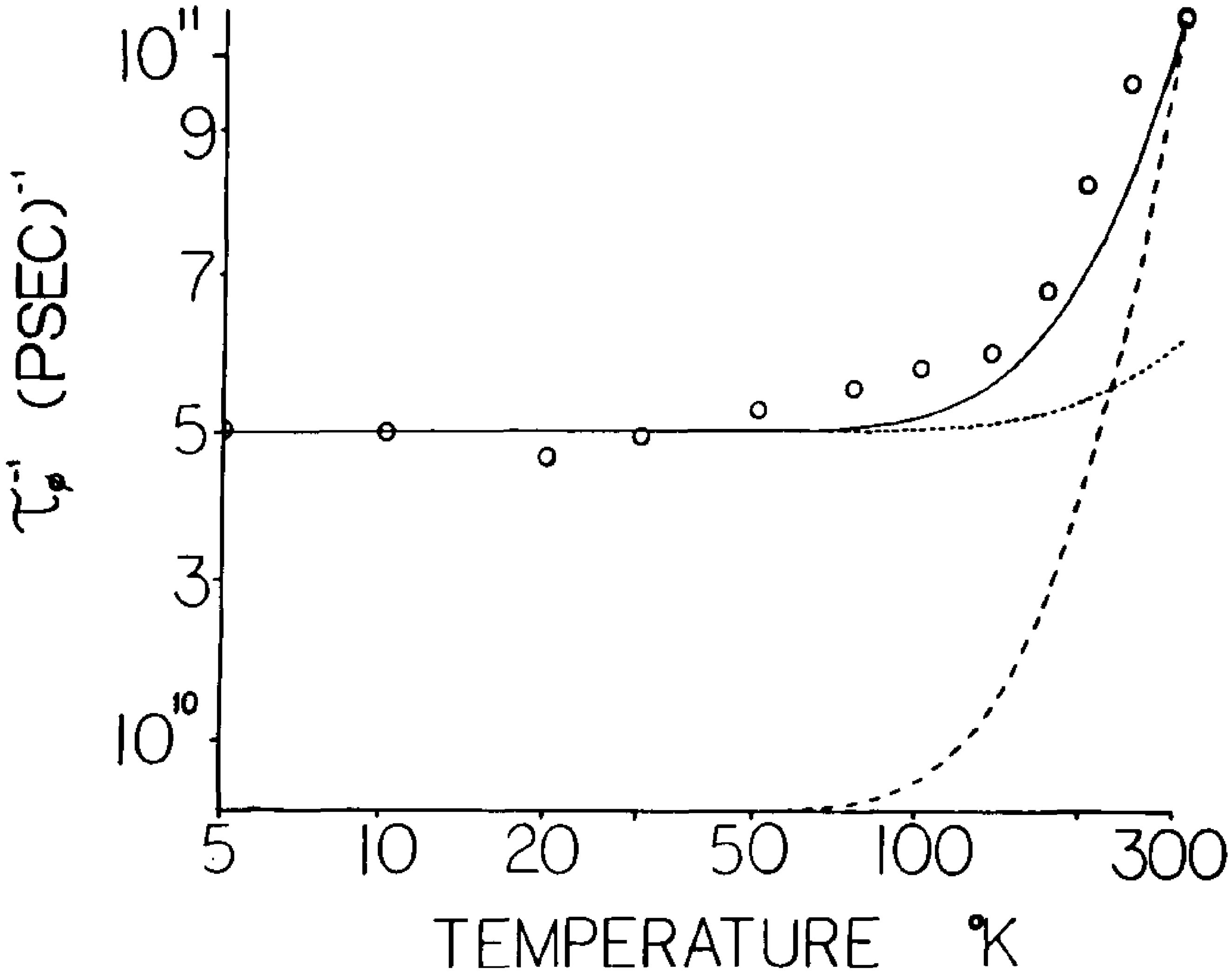

Fig. (7.2): Theoretical and experimentally measured dephasing rates $\tau_\phi$ of the 1086 cm$^{-1}$ mode of calcite plotted versus temperature. The dotted and dashed curves represent the decay rate for the 3 phonon splitting and scattering processes, respectively. The solid curve represents the best fit for a combination of both processes.

$$N_{modes} = \frac{(k_{phonon}^2 \, \Delta k \, \Delta\Psi)}{(2\pi)^3} \tag{7.1}$$

where $k_{phonon}$ ~$2k_{laser}$ ~3.66 x $10^4$, $\Delta k = 1\text{cm}^{-1}$, and $\Psi = 10^{-4}$ sr. This leads to a density of excited modes equal to ~ 100 modes/cm$^3$. For comparison, the approximate total density of modes in the branch is ~ $10^{22}$. The number of coherent optical phonons per mode which have been generated is then $N_{phonon}/N_{modes}$ ~ $10^7$ phonons/mode. Comparing this to the thermal equilibrium number at room temperature gives

$$N_{thermal} = \frac{1}{e^{(\hbar\omega/kT)}-1} = 5\cdot 10^{-3} \, phonons \ / \ mode \tag{7.2}$$

leading to a thermally excited phonon density $N_{thermal}$ x $N_{modes}$ ~ $10^{-1}$ phonons/cm$^3$. This shows that the number of coherent phonons generated by the two interacting laser pulses greatly exceed the thermal phonon number in the mode k ±Δk; the ratio of these two quantities being ~ $10^{10}$. Calculating a temperature for the coherent population using these numbers, yields temperatures on the order of $10^{10}$ K. This shows that the coherent optical phonon distribution is non-Boson like. Information regarding the phonon dynamics in this regime of high excitation can only be obtained with direct time resolved measurements.

Previous workers [6,12,13,15] have used 3 phonon anharmonic processes to account for the observed temperature dependence of optical phonon decay times. Higher order multiphonon processes, involving at least four phonons, are necessary to account for the experimentally observed behavior in calcite. We will show in the following that the temperature dependence of the $A_{1g}$phonon decay rate can be modeled by using three and four phonon decay and scattering processes. These results indicate that other dephasing mechanisms, such as scattering from defects and impurities, do not play a significant role. As a result, the main dephasing mechanisms are attributed to depopulation.

Below, we incorporate the anharmonic processes which involves both the cubic and quartic terms of the interaction Hamiltonian. The quartic terms are mandatory and have been included for two reasons: 1) The Hamiltonian which results when only the cubic terms in the anharmonic interaction are retained, leads to a system without a lowest energy state, or ground state. This is a physically unrealistic situation. The inclusion of the quartic terms, however, circumvents this anomaly, and leads to a system with a ground state [23,24]. 2) The third order processes which are governed by the cubic terms are often restricted by the stringent requirements imposed by the energy and momentum conservation laws. As a result, such a limited number of three phonon processes may be allowed, that the quartic terms can be of comparable importance and significantly contribute to the phonon dephasing rate.

Calcite belongs to the $D_{3d}$ crystal class. The selection rules ~~for cubic~~ (3) and quartic (4) phonon interactions can be determined using standard group theory methods [25]. For three phonon decay events, the $A_{1g}$ mode, being totally symmetric, will decay into two phonons of the same symmetry, i.e., 2 $E_u$, 2 $E_g$, 2 $A_{1u}$, 2 $A_{2u}$, 2 $A_{1g}$, 2 $A_{2g}$. Table (7.1a, 7.1b) shows all of the allowed 3 and 4 phonon processes, which are given by the products of the irreducible representations of the $D_{3d}$ group. There are six possible three phonon decay paths allowed by symmetry, with another six possible three phonon scattering processes, that involve the $A_{1g}$ mode. In order to determine what processes actually exist, energy and momentum conservation must be maintained. A list of the known vibration modes at k=0 and their symmetry and dispersion is given in Table (7.2).

Using the selection rules of Tables (7.1a,b), and the vibrational frequencies listed in Table 2 show that only one 3 phonon decay path exists:

$$A_{1g\,(1086)}=E_{u\,(715)}+E_{u\,(371)} \tag{7.3a}$$

and only one 3 phonon scattering process exists:

$$A_{1g\,(1086)}+E_{u\,(321)}=E_{u\,(1407)}. \tag{7.3b}$$

| * | $A_{1g}$ | $E_g$ | $A_{2u}$ | $E_u$ | $A_{1u}$ | $A_{2g}$ |
|---|---|---|---|---|---|---|
| $A_{1g}$ | $A_{1g}$ | $E_g$ | $A_{2u}$ | $E_u$ | $A_{1u}$ | $A_{2g}$ |
| $E_g$ | | $A_{1g}$,$E_g$,$A_{2g}$ | $E_u$ | $A_{1u}$,$A_{2u}$,$E_u$ | Eu | Eg |
| A2u | | | A1g | Eg | A2g | A1u |
| $E_u$ | | | | A1g,A2g,Eg | Eg | Eu |
| $A_{1u}$ | | | | | A1g | A2u |
| $A_{2g}$ | | | | | | A1g |

Table (7.1a): Direct product table for the interaction of three phonons.

| * | A1g | Eg | A2u | Eu | A1u | A2g |
|---|---|---|---|---|---|---|
| A1g•A1g | A1g | | | | | |
| A1g•Eg | Eg | | | | | |
| A1g•A2u | A2u | | | | | |
| A1g•Eu | Eu | | | | | |
| A1g•A1u | A1u | | | | | |
| A1g•A1u | A2g | | | | | |
| Eg•Eg | A1g,A2g,Eg | Eg,Eg,Eg,A1g,A2g | | | | |
| Eg•A2u | Eu | A1u,A2u,Eu | | | | |
| Eg•Eu | A1u,A2u,Eu | Eu,Eu,Eu,A1u,A2u | | | | |
| Eg•A1u | Eu | A1u,A2u,Eu | | | | |
| Eg•A2g | Eg | A1g,A2g,Eg | | | | |
| A2u•A2u | A1g | Eg | A2u | | | |
| A2u•Eu | Eg | A1g,A2g,Eg | Eu | | | |
| A2u•A1u | A2g | Eg | A1u | | | |
| A2u•A2g | A1u | Eu | A2g | | | |
| Eu•Eu | A1g,A2g,Eg | Eg,Eg,Eg,A1g,A2g | A1u,A2u,Eu | Eu,Eu,Eu,A1u,A2u | | |
| Eu•A1u | Eg | A1g,A2g,Eg | Eu | A1u,A2u,Eu | | |
| Eu•A2g | Eu | A1u,A2u,Eu | Eg | A1g,A2g,Eg | | |
| A1u•A1u | A1g | Eg | A2u | Eu | A1u | |
| A1u•A2g | A2u | Eu | A1g | Eg | A2g | |
| A2g•A2g | A1g | Eg | A2u | Eu | A1u. | A2g |

Table (7.1b): Direct product table for the interaction of four phonons.

| $E_U$ | $E_G$ | $A_{2U}$ | $A_{2G}$ | $A_{1U}$ | $A_{1G}$ |
|---|---|---|---|---|---|
| 102<br>85-130 | 157<br>157-175 | 92<br>90-130 | 210 | 300<br>200-300 | 1086 |
| 123<br>123-150 | 287<br>230-300 | 136<br>136-180 | 277 | | |
| 223<br>180-223 | 1434 | 303 | | | |
| 239 | | 387 | | | |
| 297<br>290-310 | | 875<br>870-890 | | | |
| 381<br>320-381 | | | | | |
| 715 | | | | | |
| 1407 | | | | | |
| 1549 | | | | | |

Table (7.2): List of the symmetry type, vibrational frequencies, and range of dispersion for optical phonons in calcite, after Ref. 2,3,7,8. The value of the vibrational frequencies are given in units of wavenumbers. The centered number in each box gives the value of the vibrational frequency at k=0. The lower numbers give the range of dispersion of the vibrational frequencies in Brillouin zone.

The splitting process described by Eq. (7.3a) will dominate at low temperatures due to the finite probability of a phonon splitting process occurring. The scattering process in Eq. (7.3b) has an infinitely long scattering time at low temperatures because of the requirement that a negligible phonon population exists at low temperatures. Thus, the scattering process will manifest itself only at high temperatures. The values used for the $E_u$ mode above differ slightly from the k=0 values listed in Table (7.2), however, these values fall within the allowed dispersion for this mode as displayed in reference [2]. Conservation of momentum is easily satisfied because of the small dispersion in the 715 and 1407 $cm^{-1}$ modes.

Four phonon processes are needed because of the limited number of three phonon decay and dephasing pathways. As a result, the higher order phonon interactions substantially contribute to the phonon dephasing rate.

There are three types of 4 phonon processes. The symmetry rules for the four phonon processes can be obtained from Table (7.1b). The first type allows the coherent excited state phonon to decay or split into three phonons of lower energy. For the $A_1g$ mode, 13 possible decay paths exist. Of these 13 possibilities, only 5 conserve energy. These processes are:

$$E_{g\,(712)}+E_{g\,(164)}+A_{2g\,(210)}=A_{1g} \tag{7.4a}$$

$$E_{g\,(279)}+E_{u\,(715)}+A_{2u\,(92)}=A_{1g} \tag{7.4b}$$

$$E_{g\,(271)}+E_{u\,(715)}+E_{u\,(102)}=A_{1g} \tag{7.4c}$$

$$E_{g\,(712)}+E_{u\,(102)}+A_{1u\,(272)}=A_{1g} \tag{7.4d}$$

$$E_{u\,(715)}+E_{g\,(94)}+A_{2g\,(277)}=A_{1g} \tag{7.4e}$$

These processes have a finite probability of occurring, because they are of the splitting type, and therefore will dominate at low temperatures.

The second type of 4 phonon process involves the interaction of a coherent excited state phonon $\Omega_1$ and a thermally produced phonon $\Omega_2$. This interaction produces an intermediate state via the direct product table, which then decays into 2 new phonons, $\Omega_3$ and $\Omega_4$, in accordance with the 2 phonon direct product table.

For the $A_{1g}$ mode, there are 27 possible scattering mechanisms of this type allowed by symmetry considerations. The most common interaction of this type which satisfies energy and symmetry considerations is when $\Omega_1 = \Omega_3$ and, $\Omega_2 = \Omega_4$, e.g.,

$$A_{1g\,(1086)} + A_{2u\,(92)} = A_{1g\,(1086)} + A_{2u\,(92)}. \tag{7.5}$$

This can be considered as a pure dephasing process. In this process, the phase of the phonons after the collision becomes interrupted and randomized with respect to the phase of the phonons before the collision. The probability of a phonon having a particular phase will be uniformly distributed between 0 and $2\pi$, with a value $1/2\pi$. Thus there is no net loss in phonon number in the excited state, only a phase change in the vibrational oscillations before and after the collision. The reason for not considering interactions with acoustic phonons with frequencies less than $\sim 75$ cm$^{-1}$ is because of the negligible density of states for these modes [2]. Since this process is a scattering process, it has an infinitely long dephasing rate at 0K,and therefore will contribute only at high temperatures.

The third type of four phonon process corresponds to a coherent excited state phonon colliding with two thermally produced phonons to create a single phonon with a vibrational frequency equal to the sum of the three colliding phonons. A typical process of this type which satisfies energy and symmetry considerations is

$$A_{1g\,(1086)} + E_{g\,(160)} + E_{g\,(160)} = E_{g\,(1406)}. \tag{7.6}$$

The $E_g$ modes at 160 cm$^{-1}$ were chosen because these are the two modes of lowest vibrational frequencies that conserve energy in this process. These modes are more densely populated at lower temperatures than the higher vibrational modes, and as a result should have the greatest effect on the dephasing as the temperature is increased. As we can see, there are many four phonon pathways. Only a few are needed to fit the data.

The above processes account for the depopulation of the coherent excited phonon state. The exact reverse of these processes also occurs, and contributes to additional dephasing. For example, two thermally produced phonons can collide to produce a phonon in the excited state. This new phonon will not have the same phase as the coherent excited state. Thus, the loss of a coherent excited state phonon via decay or scattering along with the simultaneous production of an incoherent excited state phonon from the reverse process, leaves the net population unchanged but introduces a phonon with a phase different from the coherent excited state. The overall effect reduces the coherency of the excite phonon state and thus can be considered as a dephasing process.

The dephasing time of the coherent phonons can be calculated from the inverse linewidth arising from multiphonon processes. The interaction Hamiltonian for the anharmonic processes is given by [26]

$$H_{ANH} = \frac{1}{3!}\sum_{abc}^{ll'l''} \Phi_{abc}^{ll'l''} u_a^l u_b^{l'} u_c^{l''} + \frac{1}{4!}\sum_{abcd}^{ll'l''l'''} \Phi_{abcd}^{ll'l''l'''} u_a^l u_b^{l'} u_c^{l''} u_d^{l'''} + \cdots \tag{7.7}$$

where the summation is over all atoms and their corresponding displacements from the equilibrium position. Transforming to the normal coordinate representation to eliminate cross terms in the products of the displacement using

$$u_a^l = \epsilon(\vec{l}a ; \vec{k} j)\, q(\vec{k} j) \tag{7.8}$$

gives

$$\begin{aligned} H_{ANH} = {} & \frac{1}{(3!(mN)^{3/2})} \sum_{abc}^{ll'l''} \Phi_{abc}^{ll'l''} e_a(\vec{k}_1, j_1) e_b(\vec{k}_2, j_2) e_c(\vec{k}_3, j_3) \\ & q(\vec{k}_1, j_1) q(\vec{k}_2, j_2) q(\vec{k}_3, j_3) e^{-i(\vec{k}_1 \vec{r}^{l} + \vec{k}_2 \vec{r}^{l'} + \vec{k}_3 \vec{r}^{l''})} \\ & + \frac{1}{(4!(mN)^{2})} \sum_{abcd}^{ll'l''l'''} \Phi_{abcd}^{ll'l''l'''} e_a(\vec{k}_1, j_1) e_b(\vec{k}_2, j_2) e_c(\vec{k}_3, j_3) e_d(\vec{k}_4, j_4) \\ & q(\vec{k}_1, j_1) q(\vec{k}_2, j_2) q(\vec{k}_3, j_3) q(\vec{k}_4, j_4) e^{-i(\vec{k}_1 \cdot \vec{r}^{l} + \vec{k}_2 \vec{r}^{l'} + \vec{k}_3 \vec{r}^{l''} + \vec{k}_4 \vec{r}^{l'''})} + \ldots \end{aligned} \tag{7.9}$$

In the above equations, $\epsilon(\vec{l}\alpha, \vec{k}j)$ is the transformation matrix given by

$$\frac{1}{(mN)^{1/2}} e_a(k\, j)\, e^{-i\vec{k}\cdot r} \tag{7.10}$$

and $e(\vec{k}j)$ is the polarization vector corresponding to a particular phonon with a wavevector $\vec{k}$ and mode j. The $q(\vec{k},j)$ terms can be given by the creation and annihilation operators $a^{\dagger}$ and a;

$$q(\vec{k}_i\ j_i)=\left(\frac{\hbar}{2\Omega(\vec{k}_i\ j_i)}\right)^{1/2}\left(a^{\dagger}(-\vec{k}_i\ j_i)+a(\vec{k}_i\ j_i)\right) \tag{7.11}$$

The anharmonic Hamiltonian is then written as

$$\begin{aligned} H_{ANH} &= \frac{1}{3!}\sum_{abc}^{ll'l''}\Phi_{abc}^{ll'l''}e(\vec{k}_1 j_1)e(\vec{k}_2 j_2)e(\vec{k}_3 j_3) \\ &\quad [a_1^{\dagger}+a_1][a_2^{\dagger}+a_2][a_3^{\dagger}+a_3] \\ &\quad \exp(-i(\vec{k}_1\vec{r}^{\,l}+\vec{k}_2\vec{r}^{\,l'}+\vec{k}_3\vec{r}^{\,l''}) \\ &+ \frac{1}{4!}\sum_{abcd}^{ll'l''l'''}\Phi_{abcd}^{ll'l''l'''}e(\vec{k}_1 j_1)e(\vec{k}_2 j_2)e(\vec{k}_3 j_3)e(\vec{k}_4 j_4) \\ &\quad [a_1^{\dagger}+a_1][a_2^{\dagger}+a_2][a_3^{\dagger}+a_3][a_4^{\dagger}+a_4] \\ &\quad \exp(-i(\vec{k}_1\vec{r}^{\,l}+\vec{k}_2\vec{r}^{\,l'}+\vec{k}_3\vec{r}^{\,l''}+\vec{k}_4\vec{r}^{\,l'''})+\ldots \end{aligned} \tag{7.12}$$

The calculation of the linewidth based on standard perturbation methods are often complicated and tedious. It is more convenient to make this calculation using Green's function techniques [27] or by Klemens' analysis [28,29]. For three phonon processes of the type discussed, the linewidth is given by [26,27,30]

$$\begin{aligned} \Gamma_{(3)}(\vec{k}_1, j_1;\Omega_1,T) &= 18\frac{\pi}{\hbar^2} \\ &\sum_{\vec{k}_2, j_2}\sum_{\vec{k}_3, j_3} |V(\vec{k}_1, j_1;\vec{k}_2, j_2;\vec{k}_3, j_3)|^2\times\Delta(\vec{k}_1+\vec{k}_2+\vec{k}_3) \\ &[(1+\bar{n}_2+\bar{n}_3)[\delta(\Omega_1-\Omega_2-\Omega_3)-\delta(\Omega_1+\Omega_2+\Omega_3)]+(\bar{n}_2-\bar{n}_3)[\delta(\Omega_1+\Omega_2-\Omega_3)-\delta(\Omega_1-\Omega_2+\Omega_3)]] \end{aligned} \tag{7.13}$$

The quartic contribution to the linewidth can be calculated using similar techniques. It is given by

$$\begin{aligned} \Gamma_{(4)}(\vec{k}_1, j_1;\Omega_1,T) &= 96\frac{\pi}{\hbar^2}\sum_{\vec{k}_2, j_2}\sum_{\vec{k}_3, j_3}\sum_{\vec{k}_4, j_4} \\ &|V(\vec{k}_1, j_1,\vec{k}_2, j_2,\vec{k}_3, j_3,\vec{k}_4, j_4|^2\Delta(\vec{k}_1+\vec{k}_2+\vec{k}_3+\vec{k}_4)\times \\ &[(1+\bar{n}_2+\bar{n}_3+\bar{n}_4+\bar{n}_2\bar{n}_3+\bar{n}_2\bar{n}_4+\bar{n}_3\bar{n}_4)[\delta(\Omega_1-\Omega_2-\Omega_3-\Omega_4)-\delta(\Omega_1+\Omega_2+\Omega_3+\Omega_4)]+ \\ &(\bar{n}_2(1+\bar{n}_3+\bar{n}_4)-\bar{n}_3\bar{n}_4)[\delta(\Omega_1+\Omega_2-\Omega_3-\Omega_4)-\delta(\Omega_1-\Omega_2+\Omega_3+\Omega_4)] \\ &+(\bar{n}_2\bar{n}_3-\bar{n}_4(1+\bar{n}_2+\bar{n}_3))[\delta(\Omega_1+\Omega_2+\Omega_3-\Omega_4)-\delta(\Omega_1-\Omega_2-\Omega_3+\Omega_4)]] \end{aligned} \tag{7.14}$$

where $\overline{n}_i$ is the mean occupation number of phonons of the type $\vec{k}_i, j_i$ and phonon frequency $\Omega_i$. The $\Delta(\cdot)$ allows for phase matching of the phonons, or momentum conservation. In the above equations, the V's are complicated functions which contain the information about the anharmonmic coupling coefficients, phonon polarization vectors, atomic masses and normal mode frequencies.

## [7.6] Discussion

The temperature dependence of the dephasing time due to three phonon processes can be obtained from Eq. (7.13). The first two terms in Eq. (7.13) yields,

$$\tau^{-1}{}_{\phi_3}(T)=\gamma_1(\bar{n}_2+\bar{n}_3+1) \qquad (7.15)$$

for the splitting process, and

$$\tau^{-1}{}_{\phi_3}(T)=\gamma_2(\bar{n}_2-\bar{n}_3) \qquad (7.16)$$

for the scattering process, where $n_i$ is the thermal equilibrium population of the ith phonon vibration $\bar{n}_i=\{\exp(\hbar\Omega/kT)-1\}^{-1}$ and T is the temperature of the lattice.

In Fig (7.2), the phonon decay rate of these processes are plotted versus temperature along with the experimental data, for comparison. The vibrational frequencies which were used in Eqs. (7.15) & (7.16) correspond to those given in Eqs. (7.3a) & (7.3b), respectively From this figure, we see that the 3 phonon splitting process is nearly independent of temperature and can only fit the low temperature data by properly adjusting $\gamma$, while the 3 phonon scattering process is highly dependent on temperature and can only fit the high temperature data. A combination of these processes is more realistic since it includes additional depopulation and dephasing mechanisms. This gives a reasonable fit to the experimental data at high temperatures. The fitting parameters in this case were .528 and 1.77 $cm^{-1}$ for the splitting and scattering processes, respectively.

The contribution to the temperature dependence of the dephasing time arising from the 4 phonon splitting process is given by the first term in Eq. (7.14). Using the procedures mentioned above, yields

$$\tau^{-1}{}_{\phi_4}(T)=\gamma_3(1+\bar{n}_2+\bar{n}_3+\bar{n}_4+\bar{n}_2\bar{n}_4+\bar{n}_3\bar{n}_4+\bar{n}_2\bar{n}_3) \qquad (7.17)$$

where $\bar{n}_i$, i=2,3,4, are the three phonon states produced by the decay of the $A_1g$ mode. The decay rate for these processes are plotted as a function of temperature in Fig. (7.3a-d). These processes all have the same salient features of a constant decay rate at low temperatures and a rapidly increasing decay rate going towards

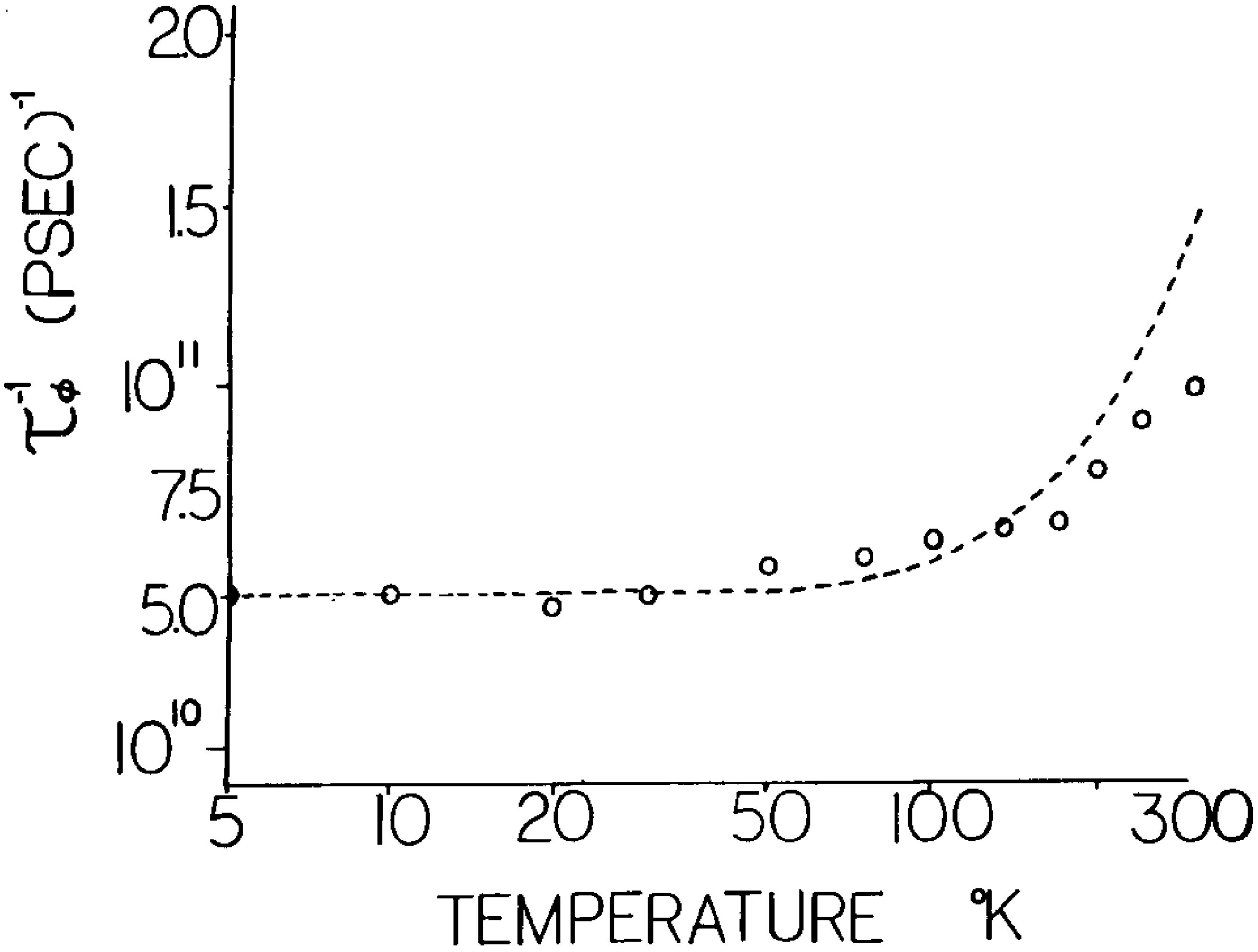

Fig. (7.3a): Theoretical contribution to the 4 phonon dephasing rate $\tau_\phi^{-1}$ due to splitting. The experimental data is also shown for comparison. Figs. (7.3a-d) correspond to Eqs. (7.4a-d), respectiively. The fitting parameter $\gamma$ was chosen to be .528 cm$^{-1}$ for these four interactions.

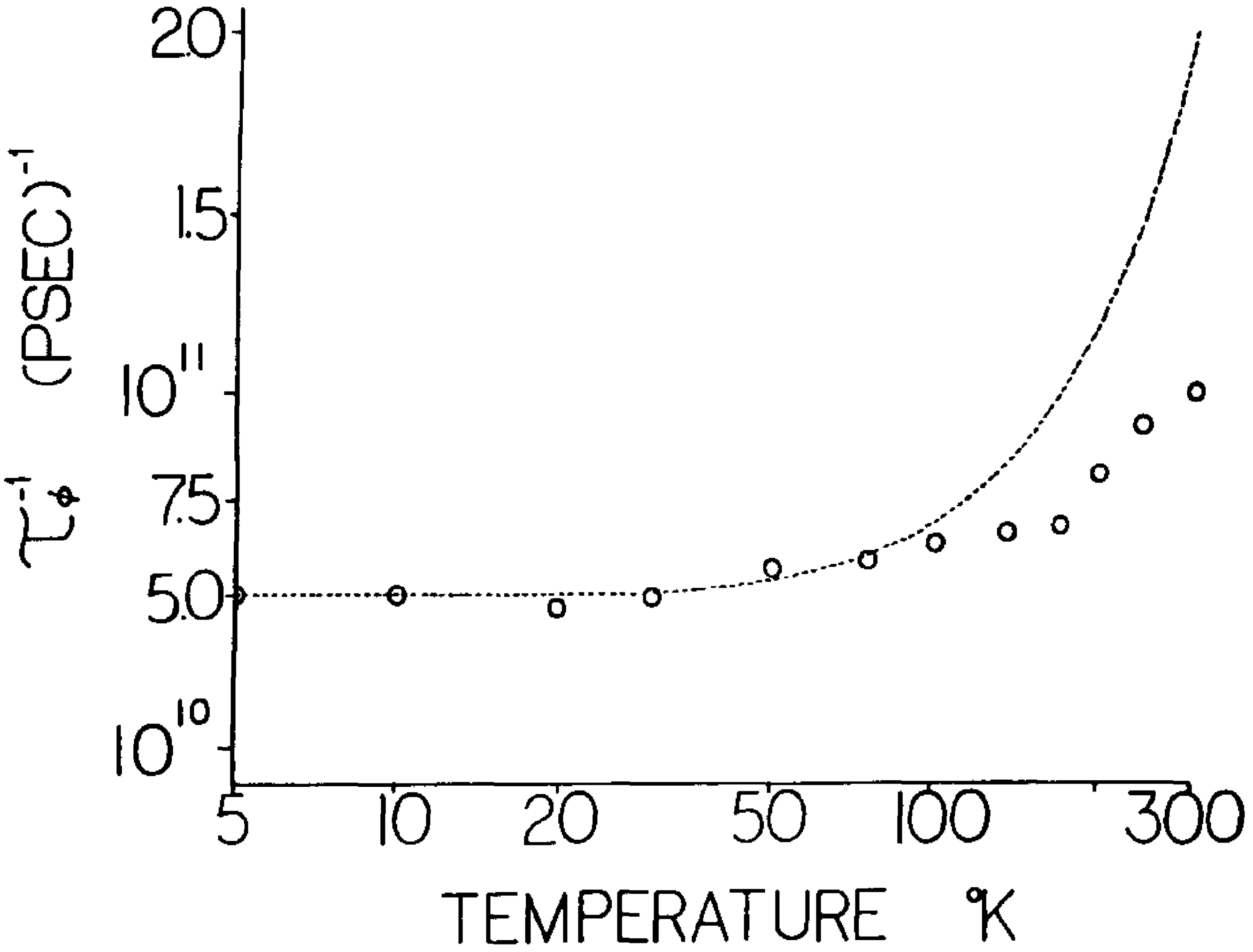

Fig. (7.3b): Theoretical contribution to the 4 phonon dephasing rate $\tau_\phi^{-1}$ due to splitting (Eq. (7.3b)).

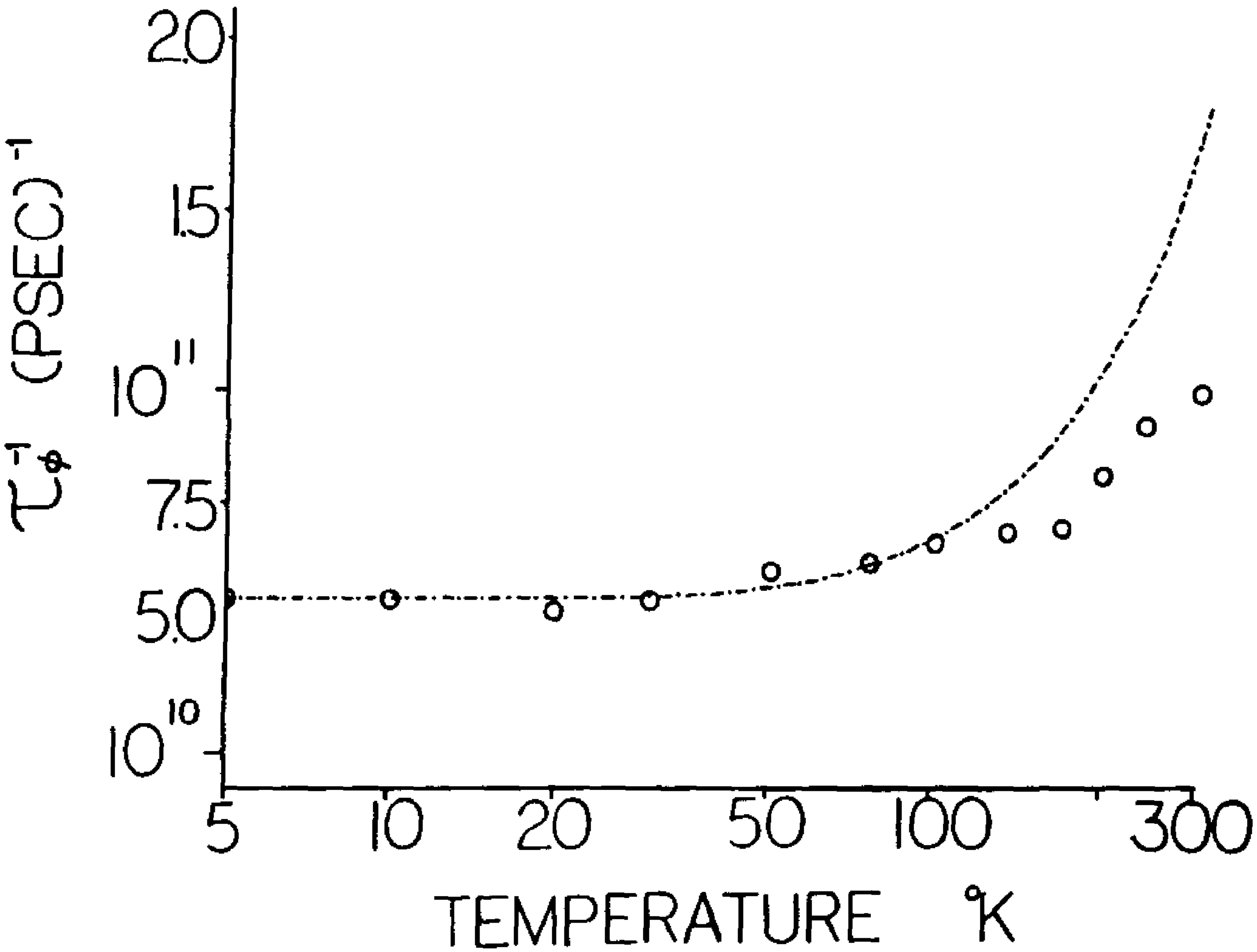

Fig. (7.3c): Theoretical contribution to the 4 phonon dephasing rate $\tau_\phi^{-1}$ due to splitting (Eq. (7.3c)).

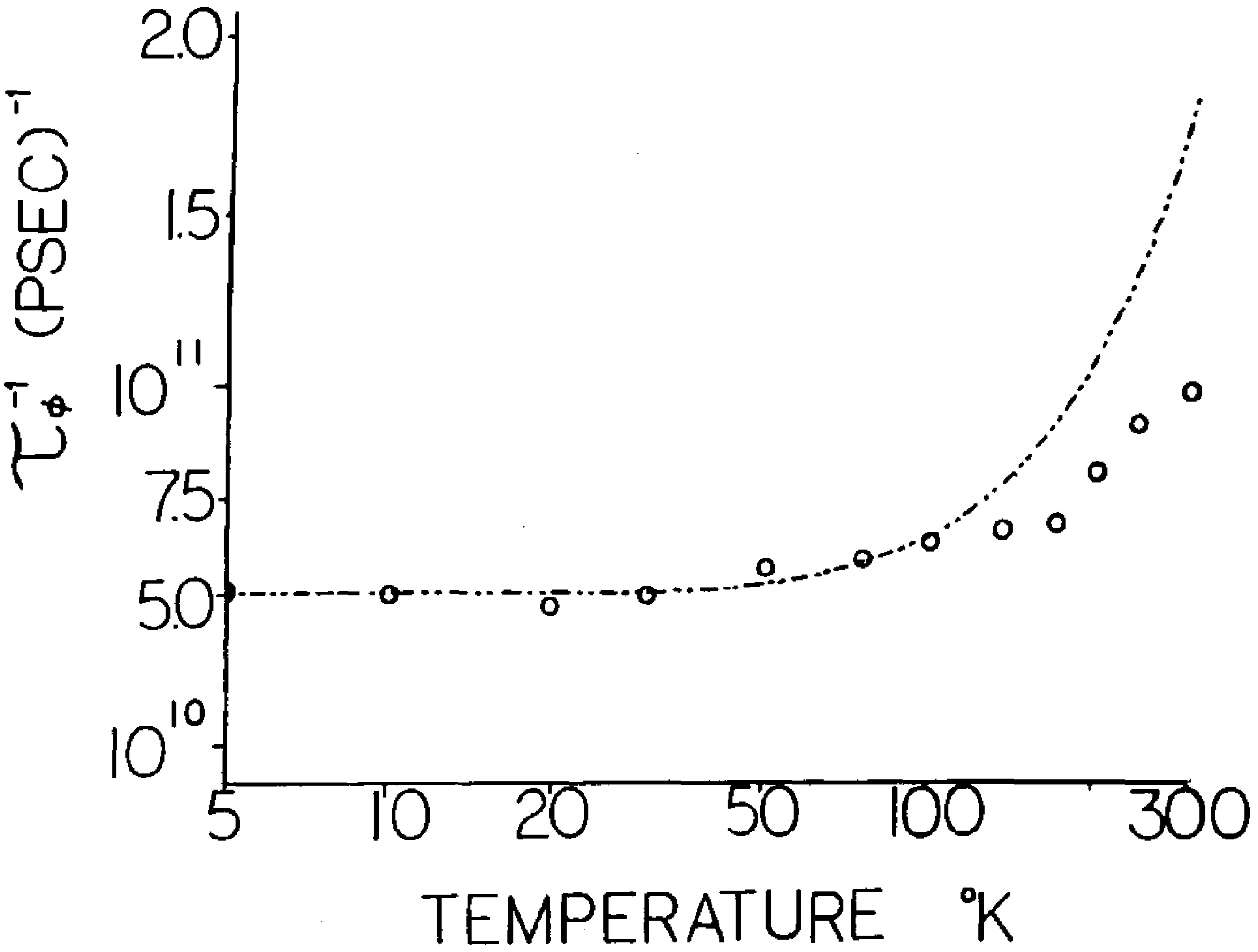

Fig. (7.3d): Theoretical contribution to the 4 phonon dephasing rate $\tau_\phi^{-1}$ due to splittng (Eq. (7.3d)).

higher temperatures. The four phonon splitting process clearly shows the same type of temperature dependence which is observed in the data. The vibrational frequencies used in Eq. (7.17) and displayed in Fig. (7.3a-d) correspond to Eqs. (7.4a-d) respectively. The fitting parameter for theses curves are .528 cm$^{-1}$.

The temperature dependence of the dephasing time for the 4 phonon scattering process described by Eq. (7.5) is given by considering the second term of Eq. (7.14), which leads to a dephasing rate of

$$\tau^{-1}{}_{\phi_4}(T)=\gamma_4(\bar{n}_2(1+\bar{n}_3+\bar{n}_4)-\bar{n}_3\bar{n}_4) \tag{7.18}$$

In this equation $n_2$ is one of the incoming phonons, and $n_3$ and $n_4$ are the outgoing phonons. For pure dephasing, $\Omega_1 = \Omega_3$, and $\Omega_2 = \Omega_4$. The temperature dependence for this process is plotted in Fig. (7.4). The coherent excited state phonon and the thermally produced phonon used in this calculation have vibrational frequencies of 1086 an 92 cm$^{-1}$, respectively. The fitting parameter used for this calculation is .217 cm$^{-1}$. The plot in Fig. (7.7) shows that for these phonons, this type of four phonon interaction can model the high temperature data, but not the low temperature data.

The temperature dependence of the dephasing time due to the third type of four phonon interaction described by Eq. (7.6) is given by

$$\tau^{-1}{}_{\phi_4}(T)=\gamma_5(\bar{n}_2\bar{n}_3-\bar{n}_4(1+\bar{n}_2+\bar{n}_3)) \tag{7.19}$$

In this equation, $n_2$ and $n_3$ are the population of incoming phonons, and $n_4$ is the population of the outgoing phonon. Plotting the decay rate versus temperature for this type of 4 phonon scattering process in Fig. (7.4) shows that this mechanism can account for the high temperature regime of the experimental data, but cannot explain the low temperature data. The vibrational frequencies of the two thermally produced incoming phonons were 160 cm$^{-1}$ each, with a fitting parameter of 1.5 cm$^{-1}$. From the five types of models proposed, the process which most closely resembles the experimental data is that of 4 phonon decay.

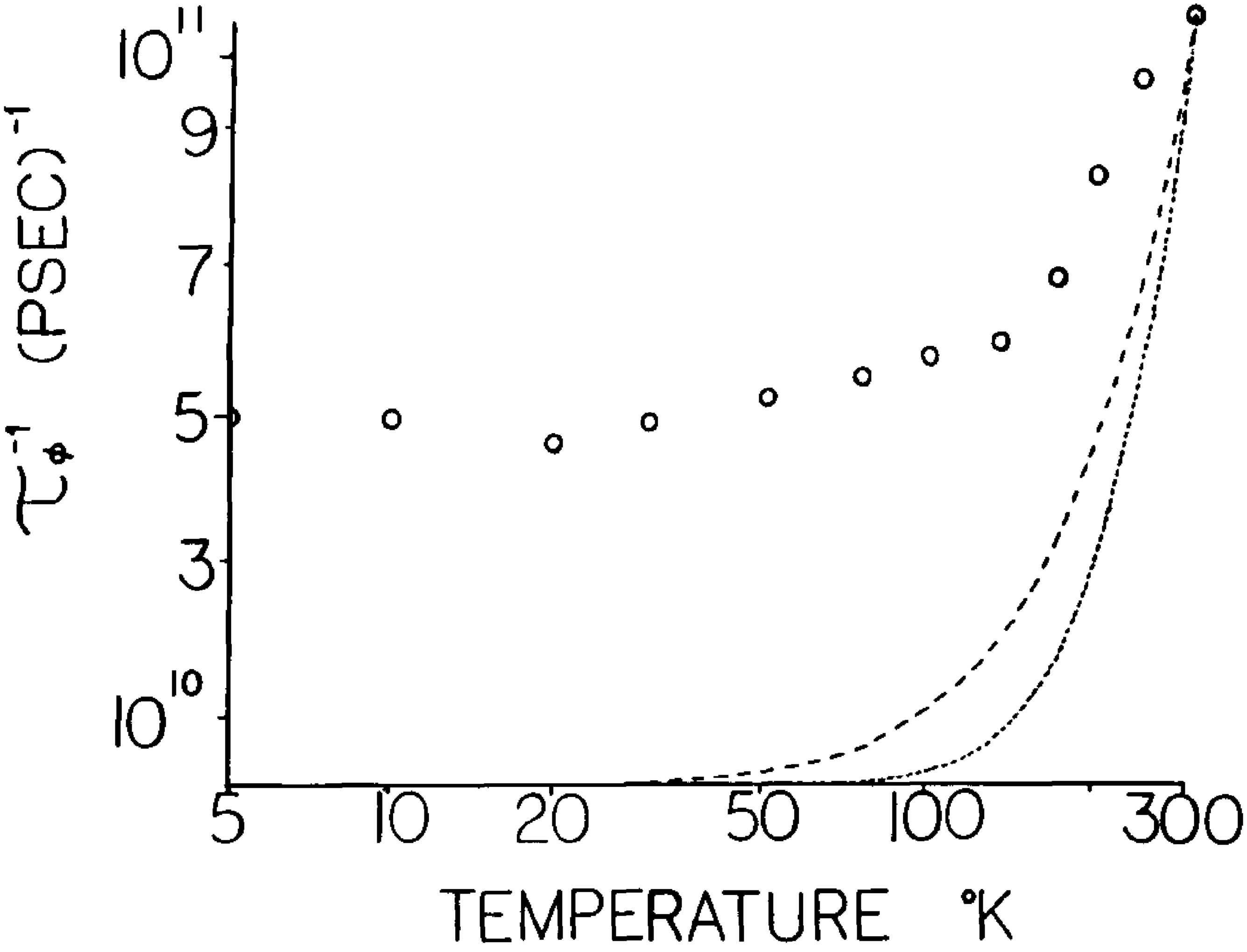

Fig. (7.4): Experimental results with the theoretical contribution to the 4 phonon dephasing rate $\tau_\phi^{-1}$ due to scattering.

The phonon decay dynamics combine all 3 and 4 phonon processes discussed above, because the total dephasing is given by the inverse linewidth in Eqs. (7.13) & (7.14), which is a sum of all the allowed processes. It is apparent that a combination of a three phonon decay process with any of the other processes discussed will in fact give a qualitative fit to the experimental data. With this in mind, a combination of the different types of decay and scattering models were investigated. The combination of processes which gives the best fit to the experimental data is a combination of a three phonon splitting process and a four phonon splitting process. In Fig (7.5), we show a combination of the 3 and 4 phonon decay mechanisms, which gives an excellent fit to the experimentally measured dephasing times. The vibrational frequencies which were used in this calculation correspond to Eq. (7.3a) and (7.4a). The fitting parameters which give the best fit are 0.268 and 0.260 $cm^{-1}$, for the three phonon and four phonon splitting processes respectively. In addition, this model accurately predicts the dephasing time for temperatures beyond the range investigated in our work. Our model predicts a dephasing time of ~ 3 psec. at 700K, which is in excellent agreement with the measured linewidth, ~ 3.5 $cm^{-1}$ [1]. Using the model depicted in Fig. (7.2), which uses only 3 phonon processes, predicts a dephasing time of ~4 psec. at 700K.

An important feature is obtained from this analysis. The four phonon contribution contributes equally, with respect to the three phonon contribution. However, since there are five allowed four phonon splitting paths with roughly the same size coupling coefficient with the same qualitative temperature behavior which occur simultaneously, the total four phonon splitting contribution is divided up among the five pathways. The four phonon fitting parameter therefore represents a lumped anharmonic coefficient. The three phonon splitting contribution is due to only one path, so its fitting parameter represents the anharmonic

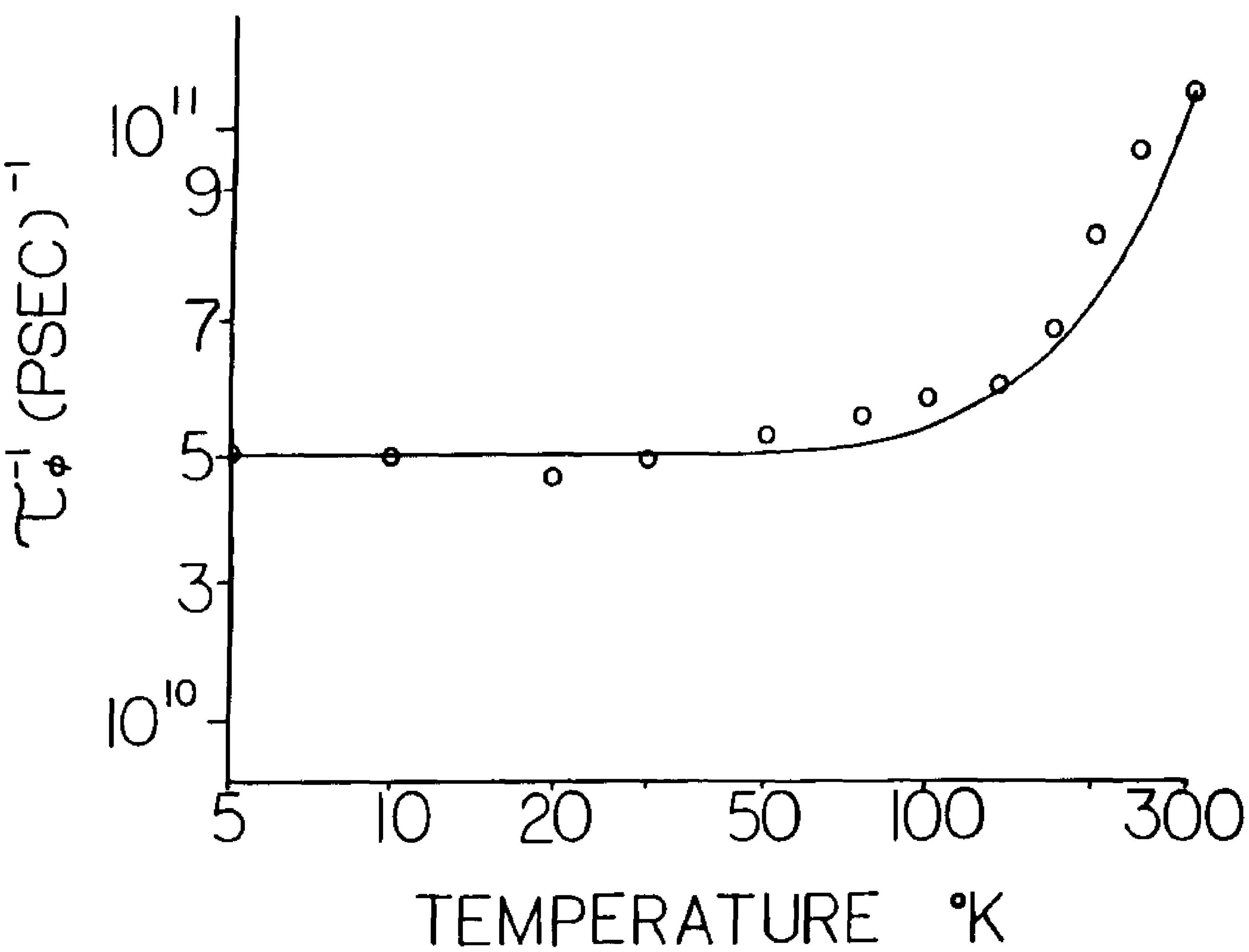

Fig. (7.5): The solid curve represents the phonon dephasing rate $\tau_\phi^{-1}$ due to a combination of the 3 phonon splitting processes and a 4 phonon splitting processes.

coefficient directly. With this in mind, the ratio of the quartic anharmonic coefficient to the cubic coefficient is $\gamma_3/5\gamma_1 = 0.19$, showing that the quartic terms are significant.

Our work shows that 1) depopulation dynamics are mainly responsible for the coherent dephasing of the 1086 $cm^{-1}$ optical phonon mode in calcite. At low temperatures, the dephasing is dominated by splitting processes, due to the finite dephasing rate at low temperatures, while at high temperatures, the scattering processes become significant. 2) The combination of the three phonon splitting process with any other process gives a qualitative agreement with the experimental data. This implies that the three phonon splitting process is the most dominant process. 3) A combination of both three and four phonon splitting processes were found to give the best fit to the data. This combination of processes involves only splitting processes, which implies that splitting contributes more to the dephasing, as compared to the scattering, for the temperature range investigated. 4) In addition, the different combinations of three and four phonon processes show that the addition of a four phonon splitting mechanism to the three phonon splitting process gives a better account of the system than the addition of the three phonon scattering mechanism. This shows that four phonon processes are necessary to explain the experimental data. The total quartic anharmonic coefficient is significant for the dephasing of optical phonons. This coupling coefficient is as large as the three phonon process, and as a result, both processes have similar transition rates and contribute equally to the relaxation processes. 5) The model depicted in Fig. (7.4) accurately predicts the dephasing rate at temperatures higher than what was investigated in this work.

### [7.7] Conclusion

In conclusion, we have measured the temperature dependence of the dephasing time of the 1086 $cm^{-1}$ mode of calcite, in real time, using a single laser pulse.

The temperature dependence of the dephasing time has been fit to a theory involving both three and four phonon interactions. We have found that the four phonon contribution must be included to explain the temperature dependence of the dephasing time. This mechanism also contributes as much as the three phonon terms. As a result, the four phonon interactions which arise from the quartic terms in the expression for the anharmonic Hamiltonian should not be neglected when the phonon dynamics of the 1086 $cm^{-1}$ mode of calcite are being considered.

## Notes

[1] Park, K., Thermal Variation of a Raman Line Width in Calcite, Phys. Lett., Vol 25A, No. 7, 490, (1967)

[2] Plihal, M., and Schaack, G., Lattice Dynamics of Crystals of the Calcite Structure, Phys. Stat. Sol., Vol 42, 485, (1970)

[3] Plihal, M., Lattice Dynamics of Crystals of the Calcite Structure, Phys. Stat. Sol. (b), Vol 56, 495, (1973)

[4] Porto, S. P. S., Giordmaine, J. A., and Damen, T. C., Depolarization of Raman Scattering in Calcite, Phys. Rev., Vol. 147, No. 2, 147, (1966)

[5] Alfano, R., and Shapiro, S., Optical Phonon Lifetime Measured Directly with Picosecond Pulses, Phys. Rev. Lett., Vol 20, 1247, (1971)

[6] Laubereau, A., Wochner, G., and Kaiser, W., Direct Observation of the Relaxation Time of the Symmetric Molecular $CO_3^{-2}$ Vibration of Calcite, Opt. Comm., Vol. 14, 75, (1975)

[7] Cowley, E. R., and Pant, A. K., Lattice Dynamics of Calcite, Phys. Rev. B, Vol. 8, No. 10, 4795, (1973)

[8] Hellwege, K. H., Lesch, W., Plihal, M., and Schaack, G., Zwei-Phononen-Absorptionsspektren und Dispersion der Schwingungszweige in Kristallen der Kalkspatstruktur Z. Physik, Vol. 232, 61, (1970)

[9] Alfano, R. R., and Shapiro, S. L., Establishment of a Molecular Vibrational Decay Route in a Liquid, Phys. Rev. Lett., Vol. 29, No. 25, 1655, (1972)

[10] Laubereau, A., and Kaiser, W., Vibrational Dynamics of Liquids and Solids Investigated by Picosecond Light Pulses, Rev. Mod. Phys., Vol. 50, No. 3, 607, (1978)

[11] Laubereau, A., von der Linde, D., and Kaiser, W., Direct Observation of the Lifetime of a Polariton Mode in Gallium Phosphide, Opt. Comm., Vol. 7, No. 3,

173, (1973)

[12] Kuhl, J., and Bron, W., Temperature Dependence of Longitudinal Optical Phonon Lifetimes in GaP, Sol. Sta. Comm., Vol. 49, No. 10, 935, (1984)

[13] Bron, W. E., in "Nonequilibrium Phonon Dynamics", Series B:Physics, Vol. 124, Chapter 1,NATO ASI Series, Plenum NY (1985)

[14] Laubereau, A., von der Linde, D., and Kaiser, W., Decay Time of Hot TO Phonons in Diamond, Phys. Rev. Lett., Vol. 27, 802, (1971)

[15] Gale, G., and Laubereau, A., Direct Measurement of Picosecond and Sub-Picosecond Phonon Lifetimes in $\alpha$ - Quartz, Opt. Comm., Vol 44, No. 4, 273, (1983)

[16] Saha, S. K., and Hellwarth, R. W., Raman Induced Phase Conjugation Spectroscopy, Phys. Rev. A, Vol. 27, No. 2, 919, (1983)

[17] Dorsinville, R., Delfyett, P. J., and Alfano, R. R., Picosecond Raman-induced Phase-conjugation in Liquids and Solids, Appl. Optics, Vol. 26, No. 17, 3655, (1987)

[18] Dorsinville, R., Delfyett, P. J., and Alfano, R. R., Generation of 3 Picosecond Pulses by Spectral Selection of the Continuum Generated by a 25 psec Second Harmonic Nd:YAG Laser Pulse in a Liquid, Appl. Opt., Vol. 27, No. 1, 16, (1988)

[19] Delfyett, P.J., Dorsinville, R., and Alfano, R.R., Real-time Measurements of Phonon Lifetime using a Streak Camera Raman-induced Phase-conjugation Method, Optics Letters, Vol. 12, No. 12, 1002, (1987)

[20] Heritage, J. P., Vibrational Dephasing Measurements with cw Mode-locked Dye Lasers, Appl. Phys Lett., Vol. 34, 470, (1979)

[21] Clements, W. R. L., and Stoicheff, Raman Linewidth for Stimulated Threshold and Gain Calculations, Appl. Phys. Lett., Vol 12, No. 8, 246, (1968)

[22] Barker, A. S., and Loudon, R., Dielectric Properties of Optical Phonons in $LiNbO_3$, Phys. Rev., Vol. 158, No. 2, 433, (1961)

[23] Solid State Physics', Ashcroft and Merrmin, Holt Rinheart Winston, (1976)

[24] Baym, G., Inconsistency of Cubic Boson-Boson Interactions, Phys. Rev., Vol. 117, No. 3, 886, (1960)

[25] Herzberg, G., 'Molecular Spectra And Molecular Structure', Vol. II, D. Van Nostrand Co., NY, (1945)

[26] Reissland, J. A., 'The Physics of Phonons', Wiley Interscience, (1973)

[27] Balkanski, M., Wallis, R.F., and Haro, E., Anharmonic effects in light scattering due to optical phonons in silicon, Phys. Rev. B, Vol. 28, No. 4, 1928, (1983)

[28] Klemens, P. G., Anharmonic decay of Optical Phonons, Phys. Rev., Vol. 148, No. 2, (1966)

[29] Klemens, P. G., Anharmonic Attenuation of Localized Lattice Vibrations, Phys. Rev. Vol. 122, No. 2, 443, (1961)

[30] Bruesch, I. P., Phonons: Theory and Experiment, Springer-Verlag, (1982)

# CHAPTER 8

# FUTURE TRENDS AND DIRECTIONS

## [8.1] Future Directions for RIPS

In this chapter, several potential directions are suggested for utilizing RIPS in fundamental material research and also in device and optical systems applications.

### Real Time Multi-Spectral Optical Processors

RIPS can be used for real time multispectral optical processing. Because the RIPS technique, and phase conjugation in general, is related to real time holography, the standard optical holographic techniques utilizing Fourier optics can now be performed in real time at several different frequencies.

As an example, an ultrafast multispectral image deflector can be realized using RIPS. A color image can be inserted into the optical path of the continuum beam $E_2$. The color image is chosen to have major spectral components at $\omega_L$, $\omega_L - \Omega_1$ and $\omega_L - \Omega_2$. In particular, $\omega_L$ = blue, $\omega_L - \Omega_1$ = green, and $\omega_L - \Omega_2$ = red. The nonlinear material is chosen such that it contains vibrational frequencies at $\Omega_1$ and $\Omega_2$. The multispectral image can be deflected into the RIPS direction with the proper application of the other two input pulses at $\omega_L$. Since the vibrational excitation are responsible for the grating mechanism, the gratings will dissipate at the vibrational relaxation time, which is on the order of a few picoseconds. Thus fast repetition rates can be obtained on the order of the inverse lifetime, ~1 THz.

### Oblique Raman Induced Quasi Phase Conjugation

One disadvantage to the RIPS technique is that only a small amount of the total scattered signal can be detected ~4%. It would be highly desirable to increase the amount of detected signal, and hence the signal to noise ratio. Another problem with RIPS is that when the sample is pumped extremely hard, stimulated

Raman backscattering from beam $E_2$ can occur. This can complicate the desired RIPS spectrum and give erroneous information when the vibrational relaxation time is being measured.

To over come these problems, the RIPS technique can be modified to a new oblique RIPS geometry which alienates the need for a wedge beam splitter to reflect a portion of the scattered signal. In the new geometry, the phase matching requirements dictate that the scattered signal emerge from the sample in a direction which is significantly different from the normal RIPS direction such that complete spatial seperation between the input and output signals is obtained. A schematic of the interaction is shown in Fig. (8.1). With this geometry an increase of 25 times the normal RIPS scattered spectrum is obtained. Preliminary result utilizing this technique in $LiNbO_3$ is shown in Fig. (8.2).

In this figure, the increased strenght of the scattered signal now allows for the observation of weak vibrational spectra. Comparing this spectra to the spectra displayed in chapter 3 shows the difference. The additional peaked observed in the new spectra is due to an A(z) mode and has been observed using standard spontaneous Raman scattering techniques.

## Dark Pulse Generation

Real time phonon dephasing measurements were obtained using RIPS by selecting the Stokes frequency component of the spectrum and measuring its temporal profile. The new oblique geometry can be used in a similar manner.

In the new oblique geometry, an interesting effect occurs in the Raman scattered spectrum. On the anti Stokes side of the scattered spectrum, absorption dips appear at the vibrational frequencies instead of enhanced spectral peaks (inverse Raman Effect [1,2]). This is shown in Fig. (8.3). This effect is not new and is attributed to a coupling between the Stokes and anti Stokes waves. As a point of

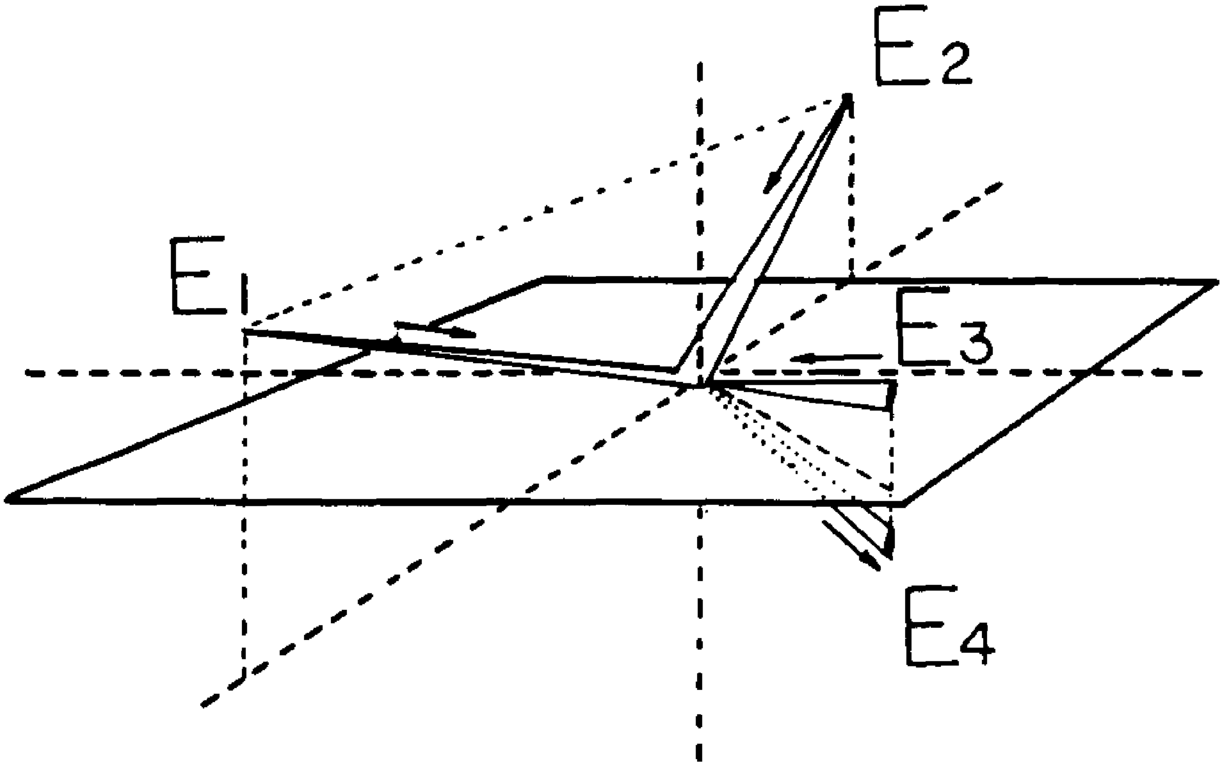

Fig. (8.1): Schematic of the 3-dimensional nondegenerate four wave mixing technique.

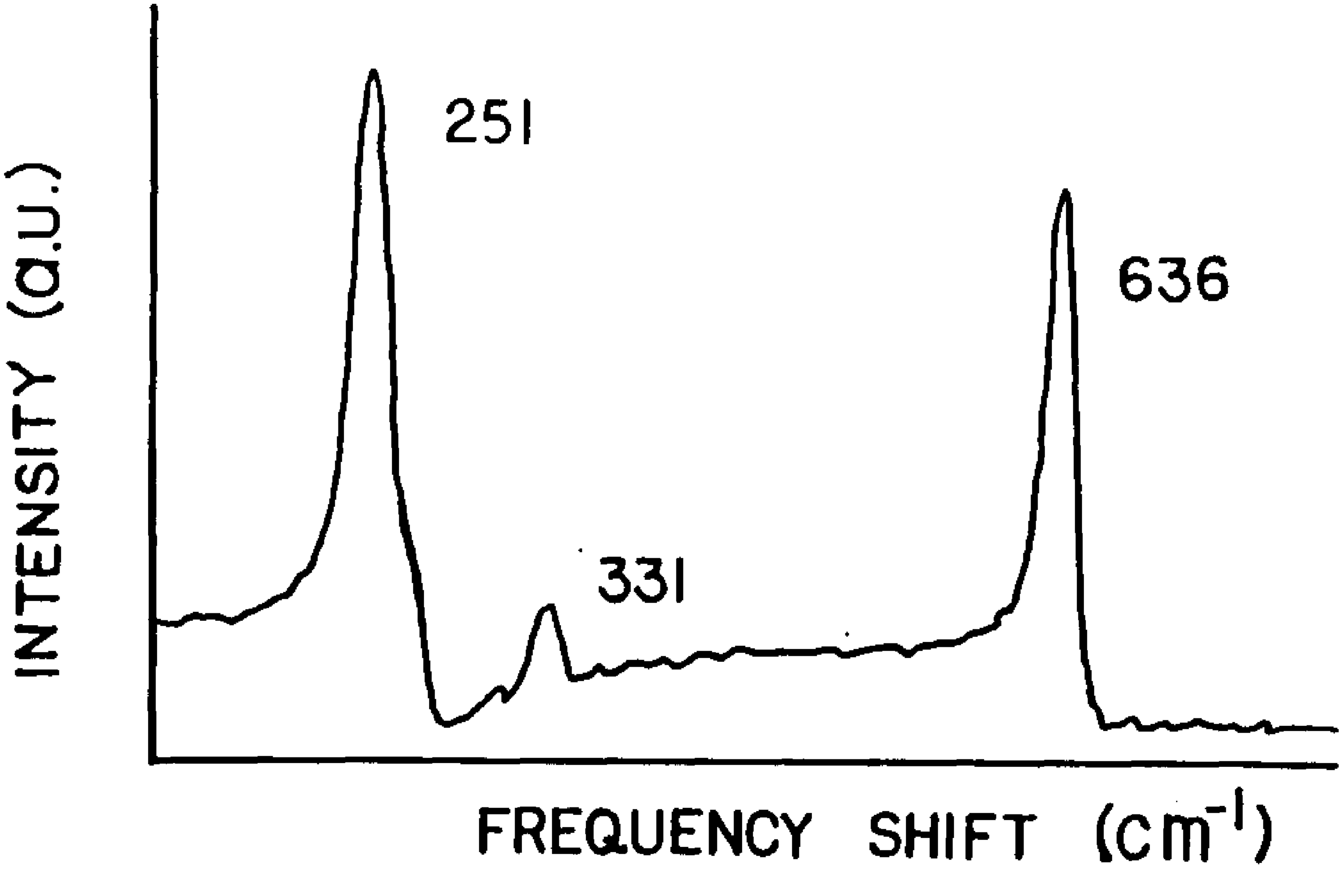

Fig. (8.2): Output spectra using the 3-D technique in lithium niobate.

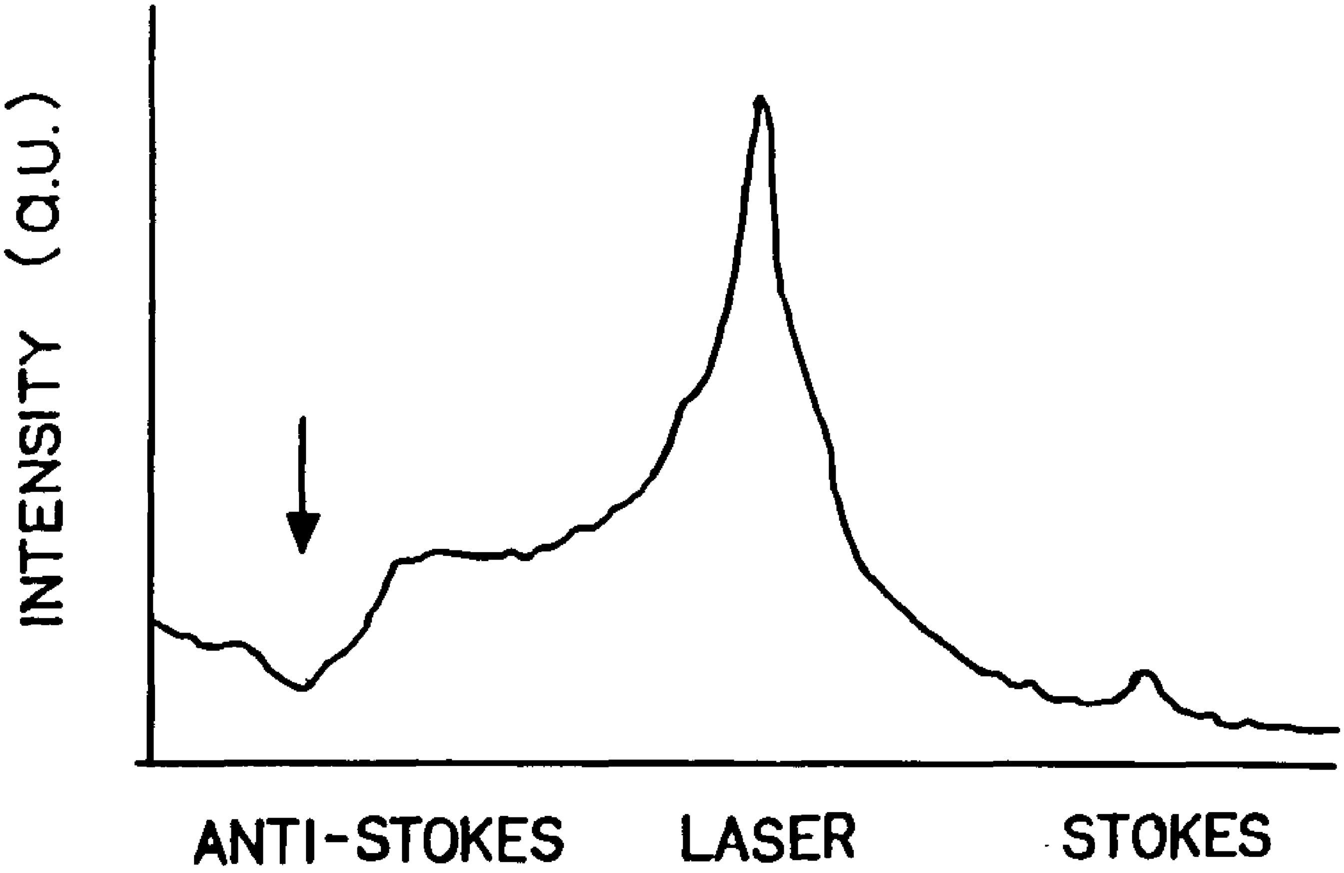

Fig. (8.3): Output spectra using the 3-D technique in $LiNbO_3$ showing both the Stokes and anti-Stokes regions.

historical interest. Alfano and Shapiro were the first to observe the inverse Raman effect in the continuum generated by picosecond laser pulses [2].

The interesting point is to examine the temporal envelope of the absorption dip. The temporal evolution of the anti- Stokes absorption dip should be related to the temporal envelope of the Stokes wave, except that the anti Stokes wave will be absorbing while the Stokes wave will be emitting. Thus the temporal envelope of the anti Stokes wave should look like a dark pulse.

Other possible applications are in ultrafast absorbing filters, i.e. picosecond active filters. For example, a multispectral image which is incident on the active medium can have specific spectral components removed which are determined by the input wavelenghts and the vibrational frequencies of the sample. Since the temporal properties of the absorption are governed by the vibrational lifetimes (~a few psec), the filter can be turned on and off in a few picoseconds.

## Phonon Assisted Transport

It has been shown that RIPS can be used as a method for generating a coherent population of phonons in crystals. Other fundamental excitations, such as electrons, can be studied to determine what effect the coherent phonon population has on the dynamics of electronic excitations.

As an example, effects on the electron transport can be studied using this technique. One possible effect which could be observed is an 'increase' in electrical conduction when a coherent phonon population is present. This could occur because the phonon oscillation is periodic in space and time. Electrons with the proper speed and direction could pass through the crystal without the normal collisions which give rise to the normal resistivity. This would be like a *laser induced superconductivity.*

### Phase Conjugation for Colliding Pulse Mode Locking

The main concept is to use two sets of counterpropagating pulses acting as a phase conjugate colliding pulse mode locker. The four pulses would oscillate in a modified figure '8' pattern, such that all four pulses would collide in the mode locking dye simultaneously. The idea is that if one set of counterpropagating pulses is good for mode locking, then two sets of counterpropagating pulses should be better. When the four pulses overlap, the resulting coherence in the dye is less than it would be for two pulses. The ejected pulses would then be shorter in time.

### Multi-Spectral Optical Logic; Spread Spectrum Communications

By varying the input polarizations in a noncentrosymmetric crystal, different RIPS spectra can be obtained due to the Raman Selection rules. Encoding informating on the input polarizations will transfer the information to different Raman scattered vibrational frequencies, thus the output information will be 'hopping' in the frequency domain. This has immediate applications in multispectral parallel processing and spread spectrum optical communications.

### Static and Transient Electric Field Effects on Coherent Optical Phonons

Applying strong electric fields on a sample can perturb the atomic structure, which in turn will effect the Raman Spectrum. This effect can be studied using the RIPS technique. For example, the change in the Raman spectrum and its temporal dynamics can be studied in real time when the sample is subjuect to 1) an ultrafast rise time step voltage, 2) RF frequency modulation, and 3) an ultrashort electrical pulse ( delta function ).

### RIPS as a Probe

A more generalized concept is to use RIPS as a probe to study the change in the Raman optical properties of a sample under study. As an example, strong IR pulses can be used to directly pump vibrational levels. The RIPS technique can be used to probe the changes in the vibrational properties of the sample in real time.

Another example is to perform RIPS in a semiconductor using wavelengths of light which have energies well below the band gap energy. Another pumping pulse with a photon energy above the band gap creates a large population of free carriers. The effect of the free carriers on the coherent phonon population can then be studied.

It is easier for those who see the light!

[R.R.A., P.J.D., 1988]

Notes

[1] Shen, Y. R., in 'Principles of Nonlinear Optics', Wiley Interscience, N.Y., (1985)

[2] Alfano, R. R., and Shapiro, S. L., Picosecond Spectroscopy Using the Inverse Raman Effect, Chemical Physics Letters, Vol. 8, 631, (1971)

# APPENDIX

In this section, the software which was utilized in the curve fitting procedures are listed.

## Computer Code for Calculating Gaussian Pulse Shapes

```
      real a(256)
      pw=5
      z=((pw/2)**2)/(.6931471806)
      do 10 i=1,256
      x=.390625*(i-128)
      a(i)=exp(-((x)**2)/z)
      write (6,*) i,a(i)
10    continue
      stop
      end
```

This program is used to compute a gaussian pulse shape. The total length of time of the pulse shape is contained in 256 pixels. The pulse duration (FWHM) is determined by the quantity 'pw'. The calibration of the pixel number is calculated by the quantity 'x', where the decimal coefficient is the number of picoseconds per pixel.

## Computer Code for Calculating an Exponential Curve

```
      real a(512)
      tau=20
      do 10 i=1,512
      a(i)=exp(-.390625*i/tau)
      write (6,*) i,a(i)
```

```
10    continue
      stop
      end
```

This program is used to compute an exponential curve. The total length of time of the pulse shape is contained in 512 pixels. The decay constant is determined by the quantity 'tau'. The calibration of the pixel number is calculated in the quantity 'a(i)', where the decimal coefficient is the number of picoseconds per pixel.

### Program for Convolutions

```
      real f(768)
      real k(512)
      real h(768)
      real g(768)
      real c(256)
      real b(512)
      real a(256)
      do 1 i=768
      f(i)=0.0
      g(i)=0.0
      k(i)=0.0
      h(i)=0.0
1     continue
      read (7,*) (z,b(i),i=1,512)
      read (7,*) (z,c(i),i=1,256)
      do 101 i=1,512
      f(i+256)=b(i)
101   continue
```

```
      do 2 i=1,256
      g(i+256)=c(i)
      h(i+256)=(c(i)**.5)
2     continue
      do 4 i=1,512
      s=0.0
      do 3 j=1,256
      a(j)=f(512-i+j)*g(256+j)
      s=s+a(j)
3     continue
      k(i)=s**2
4     continue
      do 102 i=1,256
      write(6,*)i,32.59*k(447-i)
102   continue
      stop
      end
```

This program is used to compute the convolution integral between two arbitrary waveforms. The two digitized waveforms reside in two column vectors f(i) and g(i). The temporal window of each of the waveforms is determined by the length of the column vectors. The resulting convolved output has a length equal to the sum of the lengths of the two input column vectors.

### Program for Averaging Single Shot Streak Camera Pulse Profiles

```
      real a(3072)
      real b(256)
      real c(256)
      real d(11)
```

```
      l=64
      n=11
      read (7,*) (d(i),i=1,n)
      read (7,*) (a(i),i=1,3072)
      do 9 i=1,256
      b(i)=0.0
9     continue
      do 7 m=1,n
      j=d(m)
      do 8 i=1,256
      c(i)=a(i+(j-1)*256)
8     continue
      mv=0.0
      do 13 i=1,256
      if (c(i).gt. mv) go to 14
      go to 13
14    mv=c(i)
      k=i
13    continue
      mvh=mv/2
      do 20 i=1,256
      if (c(i).gt.mvh) go to 21
20    continue
21    k=i
      do 10 i=1,256
      if (i+k-1.lt.0.0) go to 16
      b(i)=c(i+k-1)+b(i)
```

```
16    continue
10    continue
7     continue
      do 12 i=1,256
      write(6,*) i,b(i)
12    continue
      stop
      end
```

This program is designed to average several single shot events measured with a streak camera. This eliminates noise fluctuations in the streak camera output. The curves are averaged with a reference point at the half height of the rising portion of the pulse shape.

### Program for Calculating the Temperature Dependence of the Decay Rate

```
      real n1,n2,n3,n4,n5,n6,n7,n8
      c=3.0E+10
      v1=321
      v2=164
      v3=210
      v4=712
      v41=715
      v5=1407
      v6=371
      v7=1086
      v8=160
      z=.72
      a=.260
      b=.528
```

```
c=4.25
d=2.0*.264
e=3*.176
f=1.77
g=.217
h=.219
p=1.475
q=1.5
do 1 i=1,150
t=5*i
x1=z*v1/t
x2=z*v2/t
x3=z*v3/t
x4=z*v4/t
x41=z*v41/t
x5=z*v5/t
x6=z*v6/t
x7=z*v7/t
x8=z*v8/t
y1=tanh(x1)
y2=tanh(x2)
y3=tanh(x3)
y4=tanh(x4)
y41=tanh(x41)
y5=tanh(x5)
y6=tanh(x6)
y7=tanh(x7)
```

```
y8=tanh(x8)

z1=1/y1

z2=1/y2

z3=1/y3

z4=1/y4

z41=1/y41

z5=1/y5

z6=1/y6

z7=1/y7

z8=1/y8

z24=(z2*z4-z2-z4+1)/2

z34=(z3*z4-z3-z4+1)/2

z23=(z2*z3-z2-z3+1)/2

n1=(z1-1)/2

n2=(z2-1)/2

n3=(z3-1)/2

n4=(z4-1)/2

n41=(z41-1)/2

n5=(z5-1)/2

n6=(z6-1)/2

n7=(z7-1)/2

n8=(z8-1)/2

dk3net=b*(z41+z6)

dk3netn=b*(1+n41+n6)

dk3out=d*((z41-1)/2+1)*((z6-1)/2+1)

dk3outn=d*(n41+1)*(n6+1)

scat3net=f*((z1-1)/2-(z5-1)/2)
```

```
      scat3netn=f*(n1-n5)
      scat3out=c*((z1-1)/2)*((z5-1)/2+1)
      scat3outn=c*(n1)*(n5+1)
      dk4net=a*(z2+z3+z4+z24+z34+z23-1)/2
      dk4netn=a*(1+n2+n3+n4+n2*n3+n2*n4+n3*n4)
      dk4out=e*((z2-1)/2+1)*((z3-1)/2+1)*((z4-1)/2+1)
      dk4outn=e*(n2+1)*(n3+1)*(n4+1)
      scat4net1=h*(((z2-1)/2)*(1+(z7-1)/2+(z2-1)/2)-((z2-1)/2)*((z7-1)/2))
      scat4net1n=h*(n2*(1+n7+n2)-n2*n7)
      scat4out1=g*((z2-1)/2)*((z7-1)/2+1)*((z2-1)/2+1)
      scat4out1n=g*n2*(n7+1)*(n2+1)
      scat4net2=p*(-((z5-1)/2)*(1+(z8-1)/2+(z8-1)/2)+((z8-1)/2*(z8-1)/2))
      scat4net2n=p*(n8*n8-n5*(1+n8+n8))
      scat4out2=q*((z8-1)/2)*((z8-1)/2)*((z5-1)/2+1)
      scat4out2n=q*n8*n8*(n5+1)
      tf=2*3.14159*c
      t2=1.0/tf
      write(6,*) t,dk3netn+scat3netn
 1    continue
      stop
      end
```

This program is used to calculate the decay rate of an excited state phonon due to three and four phonon anharmonic interactions as a function of temperature. The calculation requires the input frequencies of the phonons which are interacting, and a weighting factor which corresponds to the strength of the interaction.

### Program for Calculating the Grating Spacing, Velocity, Dispersion Realtions, and Phase Matching Characteristics of the Moving Grating Model.

```
real l
real lpc
real lp
real kphonon
l=530.0
z=(3.14159/180.0)*10.0
do 10 i=1,100
dl=i
x1=(dl**2)/(4*(sin(z)**2))
x2=(l**2)/(4*(sin(z/2)**2))
x3=(l*dl)/(2*sin(z)*tan(z/2))
x4=((x1+x2+x3)**.5)*2*sin(z)
x5=dl*sin(z/2)/x4
dphi=asin(x5)
y=dphi*180.0/3.14159
g=((l/2/cos(z/2))+(l*tan(dphi))/(2*sin(z/2)))*cos(dphi)
v=(2*sin(dphi)*3.0*cos(z/2))/sin(z)
x6=(3.0/l)*(1-(v/3.0)*cos(z/2 + dphi))
lp=3.0/x6
x8=x6*(1-(v/3.0)*cos(z/2 + dphi))
lpc=3.0/x8
x7=2*g*cos(z/2 + dphi)
win=(1.0/(530+dl))*1.0e7
wout=(x8/3.0)*1.0e7
DW=win-wout
```

```
      W=(1.0/530)*1.0e7-win
      kphonon=(1.0/g)*1.0e7
ccccc 530+dl,dl,y,g,v,lp,x7,x8,win,wout,DW,W,kphonon
      write (6,*) W,DW
10    continue
      stop
      end
```

This program calculates the parameters which are derived in the moving grating model in c Chapter 3. The calculations require the input laser wavelength, the input crossing angle, and the desired frequency range to be investigated. The computed output gives the grating spacing, velocity, angular tilt, and output scattered wavelength for a given input Stokes wavelength.

**Program for Calculating the RIPS Spectrum**

```
      s0=6.72
      s1=1.4
      a=-14.0
      b=-12.0
      c=-5.0
      d=-0.0
      g1=5.0
      g2=5.0
      g3=4.0
      g4=5.0
      w1=18797
      w2=18773
      v1=153.0
      v2=237
```

```
      v3=321
      v4=450
      do 1 i=1,678
      y=i*1.0
      w=w2-y
      s=s1+s0*exp(-.00588*(w2-w))
      z1=(w1-w-v1)
      z2=(w1-w-v2)
      z3=(w1-w-v3)
      z4=(w1-w-v4)
      x1=(a**2)/(z1**2+g1**2)
      x2=(b**2)/(z2**2+g2**2)
      x3=(c**2)/(z3**2+g3**2)
      x4=(d**2)/(z4**2+g4**2)
      x11=s*2*a*z1/(z1**2+g1**2)
      x22=s*2*b*z2/(z2**2+g2**2)
      x33=s*2*c*z3/(z3**2+g3**2)
      x44=s*2*d*z4/(z4**2+g4**2)
      xab=2*a*b*(z1*z2+g1*g2)/((z1**2+g1**2)*(z2**2+g2**2))
      xac=2*a*c*(z1*z3+g1*g3)/((z1**2+g1**2)*(z3**2+g3**2))
      xad=2*a*d*(z1*z4+g1*g4)/((z1**2+g1**2)*(z4**2+g4**2))
      xbc=2*b*c*(z2*z3+g2*g3)/((z2**2+g2**2)*(z3**2+g3**2))
      xbd=2*b*d*(z2*z4+g2*g4)/((z2**2+g2**2)*(z4**2+g4**2))
      xcd=2*c*d*(z3*z4+g3*g4)/((z3**2+g3**2)*(z4**2+g4**2))
      write                         (6,*)                         w1-
w,x1+x2+xab+x3+x4+xad+xbd+xcd+xac+xbc+x11+x22+x33+s**2+x44+1.8
1     continue
```

```
      stop
      end
```

This program calculates the RIPS spectrum in $LiNbO_3$. The calculation requires the values of the vibrational frequencies, the linewidths, and the oscillator strengths. In addition, a nonresonant background component is added in the form of an exponential. The strength of the nonresonant background and its frequency variation must also be specified. The range of the computation must also be supplied to the program, i.e., frequency extent. The computed output gives the RIPS spectrum over a specific frequency range. This program has been designed to compute the spectrum for a material with not more than 4 vibrational modes.

## PUBLICATIONS

[1] "Determination of Temporal Correlation of Ultrafast Laser Pulses Using Phase Conjugation", J. Buchert, R. Dorsinville, P. Delfyett, S. Krimchansky and R. R. Alfano, Optics Comm., Vol. 52, 433-437, (1985)

[2] "Single Shot Autocorrelator Based on Degenerate Four Wave Mixing", J. Buchert, R. Dorsinville, P.J. Delfyett, and R.R. Alfano, Proceedings of the International Conference on Lasers '85, STS Press, McLean VA., 780-781, (1985)

[3] "Determination of Single and Collective Particle Correlation Kinetics using Time Resolved Picosecond Phase Conjugation", J.M. Buchert, R. Dorsinville, P.J. Delfyett, and R.R. Alfano, Proceedings of the International Conference on Lasers, '85, STS Press, McLean, VA., 340-343, (1985)

[4] "Time Resolved Picosecond Raman Induced Phase Conjugation in Liquid and Solids", P.J. Delfyett, R. Dorsinville, and R.R. Alfano, Proceeding of the International Laser Science Conference, American Institute of Physics Conference Proceedings No. 146, 590-591, Dallas, Texas, (1985)

[5] "Picosecond Raman Induced Phase Conjugation Spectroscopy", R. Dorsinville, P.J. Delfyett, and R.R. Alfano, in Ultrafast Phenomena V, Springer Verlag, 521-523, (1986)

[6] "Transient Gratings in Wide Band Gap Semiconductors, -Impurities and Optical Phonon Dynamics-", P.J. Delfyett, R. Dorsinville, and R.R. Alfano, Proceeding of SPIE, Vol. 793, 139-146, (1987)

[7] "Picosecond Raman Induced Phase Conjugation in Liquids and Solids", R. Dorsinville, P. Delfyett, and R. R. Alfano, Applied Optics, Vol. 26, 3655-3658, (1987)

[8] "Real Time Phonon Dephasing Measurements Using a Raman Induced Phase-conjugtion and Streak Camera Method", P.J. Delfyett, R. Dorsinville, and R.R. Alfano, Optics Letters, Vol 12, 1002-1004, (1987)

[9] "Ultrafast Laser Technology", Peter J. Delfyett, S.K. Gayen and R.R. Alfano, Encyclopedia of Science and Technology, Vol. 14, 169-190, Academic Press, (1987)

[10] "Generation of 3 psec Pulses from the Spectral Selection of a Supercontinuum Pulse generated in a Liquid", R. Dorsinville, P. Delfyett, and R.R. Alfano, Applied Optics, Vol. 27, 16-18, (1988)

## SUBMITTED PUBLICATIONS

[1] "Multiphonon Dehasing of the 1086 $cm^{-1}$ Mode in Calcite", P.J. Delfyett, R. Dorsinville, and R.R. Alfano, Phys. Rev. B15, submitted (1988)

[2] "Spectral and Temporal Measurement of the Nonlinear Third Order Susceptibility in $LiNbO_3$ ;, P.J. Delfyett, R. Dorsinville, and R.R. Alfano, JOSA B, submitted. (1988)

## ABSTRACTS AND PRESENTATIONS

[1] "Time Resolved Picosecond Raman Induced Phase Conjugation in Liquids and Solids", R. Dorsinville, P.J. Delfyett, and R.R. Alfano, in Bulletin of the American Physical Society, Vol. 30, No. 10, 1798, (1985)

[2] "Time Resolved Raman Induced Phase Conjugation in Polymers and Semiconductors", R. Dorsinville, P.J. Delfyett, and R.R. Alfano, Topical Meeting on Ultrafast Phenomena, Optical Society of America, Technical Digest, pg. 297 (1986)

[3] "Picosecond Time Resolved Transient Gratings in ZnSe", P.J. Delfyett, R. Dorsinville, and R.R. Alfano, Bulletin of the American Physical Society, Vol. 32, No. 3,609, (1987)

[4] "Real Time Phonon Dephasing Measurements using Raman Induced Phase Conjugation Spectroscopy and Streak Camera Technology", P.J. Delfyett, R. Dorsinville and R.R. Alfano, Optical Society of America Technical Digest, pg. 114, OSA Annual Meeting, Rochester, New York, (1987)

[5] "Real Time Vibrational Kinetics in Wide Band Gap Crystals and Liquids", R. Dorsinville, P.J. Delfyett, and R.R. Alfano, Bulletin of the American Physical Society, Vo. 32, No. 8, 1632, (1987)

[6] "Transient Gratings in Wide Band Gap Semiconductors", P.J. Delfyett, R. Dorsinville, and R.R. Alfano SPIE Bay Point, Florida, (1987)

[7] "Single Shot Real Time Resolved Phonon Dephasing Measurements in Calcite Using Phase Conjugation", P.J. Delfyett, R. Dorsinville, and R.R. Alfano, Bulletin of the American Physical Society, Vol. 33, No. 3, 350, (1988)

[8] "Real Time Phonon Dephasing Kinetics in Liquids and Solids", R. Dorsinville, P.J. Delfyett, and R.R. Alfano, SPIE Newport Beach, California, (1988)

[9] "Ultrafast Transient Dynamical Gratings Using Phase Conjugation", P.J. Delfyett, R. Dorsinville, and R.R. Alfano, Edward Bouchet Conference on Science and Technology, Trieste, Italy, (1988)

# BIBLIOGRAPHY

Alfano, R., and Shapiro, S., Optical Phonon Lifetime Measured Directly with Picosecond Pulses, Phys. Rev. Lett., Vol 20, 1247, (1971)

Alfano, R. R., and Shapiro, S. L., Establishment of a Molecular Vibrational Decay Route in a Liquid, Phys. Rev. Lett., Vol. 29, No. 25, 1655, (1972)

Ashcroft and Merrmin, in 'Solid State Physics', Holt Rinheart Winston, (1976)

Balkanski, M., Wallis, R.F., and Haro, E., Anharmonic effects in light scattering due to optical phonons in silicon, Phys. Rev. B, Vol. 28, No. 4, 1928, (1983)

Barker, A. S., and Loudon, R., Dielectric Properties of Optical Phonons in LiNbO$_3$, Phys. Rev., Vol. 158, No. 2, 433, (1967)

Baym, G., Inconsistency of Cubic Boson-Boson Interactions, Phys. Rev., Vol. 117, No. 3, 886, (1960)

Bron, W. E., in "Nonequilibrium Phonon Dynamics", Series B:Physics, Vol. 124, Chapter 1,NATO ASI Series, Plenum NY (1985)

Bruesch, I. P., in 'Phonons: Theory and Experiment', Springer-Verlag, (1982)

Clements, W. R. L., and Stoicheff, Raman Linewidth for Stimulated Threshold and Gain Calculations, Appl. Phys. Lett., Vol 12, No. 8, 246, (1968)

Cowley, E. R., and Pant, A. K., Lattice Dynamics of Calcite, Phys. Rev. B, Vol. 8, No. 10, 4795, (1973)

Delfyett, P.J., Dorsinville, R., and Alfano, R.R., Real-time Measurements of Phonon Lifetime using a Streak Camera Raman-induced Phase-conjugation Method, Optics Letters, Vol. 12, No. 12, 1002, (1987)

Dorsinville, R., Delfyett, P. J., and Alfano, R. R., Picosecond Raman-induced Phase-conjugation in Liquids and Solids, Appl. Optics, Vol. 26, No. 17, 3655, (1987)

Dorsinville, R., Delfyett, P. J., and Alfano, R. R., Generation of 3 Picosecond Pulses by Spectral Selection of the Continuum Generated by a 25 psec Second Harmonic Nd:YAG Laser Pulse in a Liquid, Appl. Opt., Vol. 27, No. 1, 16, (1988)

Fisher, R. A., in 'Optical Phase Conjugation', Academic Press, N.Y., (1983)

Gale, G., and Laubereau, A., Direct Measurement of Picosecond and Sub-Picosecond Phonon Lifetimes in $\alpha$ - Quartz, Opt. Comm., Vol 44, No. 4, 273, (1983)

Hellwarth, R. W., Third Order Optical Susceptibilities of Liquids and Solids, Prog. Quant. Electr., Vol 5, (1977)

Hellwege, K. H., Lesch, W., Plihal, M., and Schaack, G., Zwei-Phononen-Absorptionsspektren und Dispersion der Schwingungszweige in Kristallen der Kalkspatstruktur Z. Physik, Vol. 232, 61, (1970)

Heritage, J. P., Vibrational Dephasing Measurements with cw Mode-locked Dye Lasers, Appl. Phys Lett., Vol. 34, 470, (1979)

Herzberg, G., 'Molecular Spectra And Molecular Structure', Vol. II, D. Van Nostrand Co., NY, (1945)

Kaminow, I. P., and Johnston. W. D., Jr., Quantitative Determination of Sources of the Electro-Optic Effect in LiNbO$_3$ and LiTaO$_3$, Phys. Rev., Vol. 160, No. 3, 519, (1967) Klemens, P. G., Anharmonic Attenuation of Localized Lattice Vibrations, Phys. Rev. Vol. 122, No. 2, 443, (1961)

Klemens, P. G., Anharmonic decay of Optical Phonons, Phys. Rev., Vol. 148, No. 2, (1966)

Kuhl, J., and Bron, W., Temperature Dependence of Longitudinal Optical Phonon Lifetimes in GaP, Sol. Sta. Comm., Vol. 49, No. 10, 935, (1984)

Laubereau, A., Wochner, G., and Kaiser, W., Direct Observation of the Relaxation Time of the Symmetric Molecular $CO_3^{-2}$ Vibration of Calcite, Opt. Comm., Vol. 14, 75, (1975)

Laubereau, A., and Kaiser, W., Vibrational Dynamics of Liquids and Solids Investigated by Picosecond Light Pulses, Rev. Mod. Phys., Vol. 50, No. 3, 607, (1978)

Laubereau, A., von der Linde, D., and Kaiser, W., Direct Observation of the Lifetime of a Polariton Mode in Gallium Phosphide, Opt. Comm., Vol. 7, No. 3, 173, (1973)

Laubereau, A., von der Linde, D., and Kaiser, W., Decay Time of Hot TO Phonons in Diamond, Phys. Rev. Lett., Vol. 27, 802, (1971)

Loudon, R., The Raman Effect in Crystals, Adv in Phys.,Vol 13, 423, (1964)

Park, K., Thermal Variation of a Raman Line Width in Calcite, Phys. Lett., Vol 25A, No. 7, 490, (1967)

Plihal, M., and Schaack, G., Lattice Dynamics of Crystals of the Calcite Structure, Phys. Stat. Sol., Vol 42, 485, (1970)

Plihal, M., Lattice Dynamics of Crystals of the Calcite Structure, Phys. Stat. Sol. (b), Vol 56, 495, (1973)

Porto, S. P. S., Giordmaine, J. A., and Damen, T. C., Depolarization of Raman Scattering in Calcite, Phys. Rev., Vol. 147, No. 2, 147, (1966)

Reissland, J. A., 'The Physics of Phonons', Wiley Interscience, (1973)

Saha, S. K., and Hellwarth, R. W., Raman Induced Phase Conjugation Spectroscopy, Phys. Rev. A, Vol. 27, No. 2, 919, (1983)

Shen, Y. R., 'Principles of Nonlinear Optics', Wiley Interscience, N.Y., (1985)

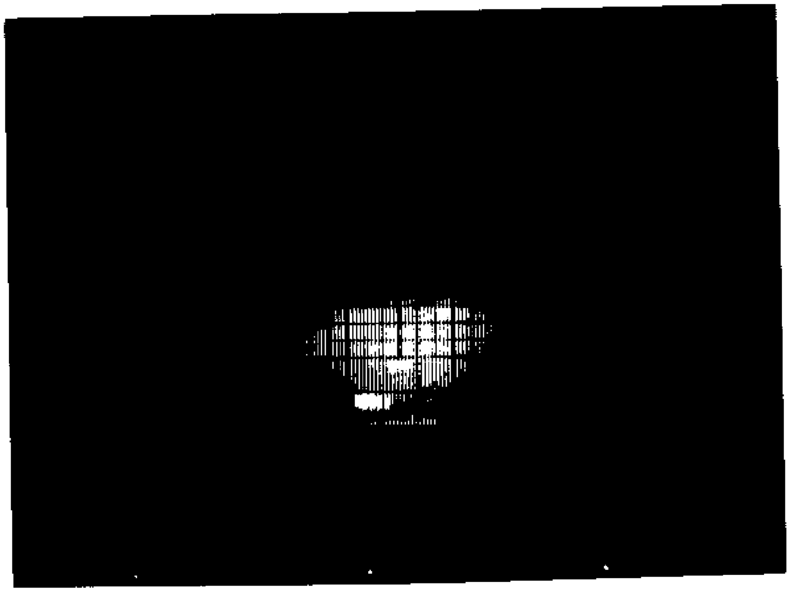

Fig. (2.2): Oscilloscope trace showing the long term stability of the Nd:YAG pulse train.

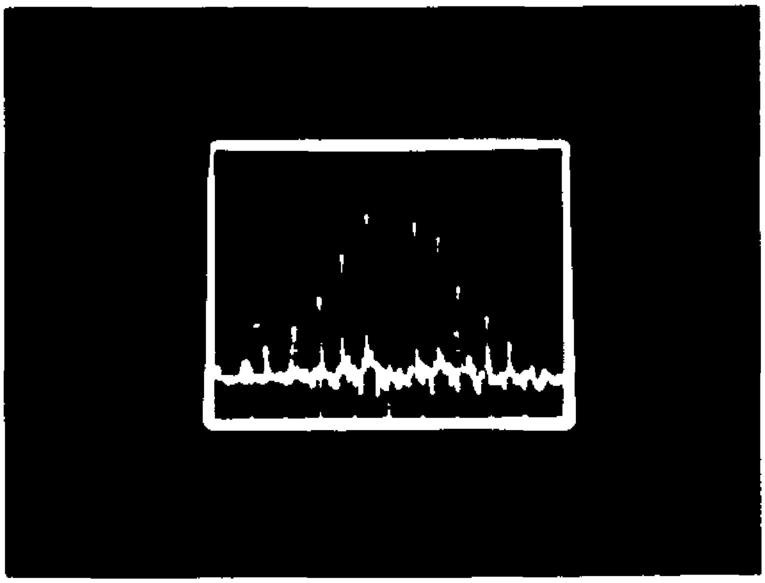

Fig. (2.3): Oscilloscope trace of the pulse train emitted from the Nd:YAG laser.

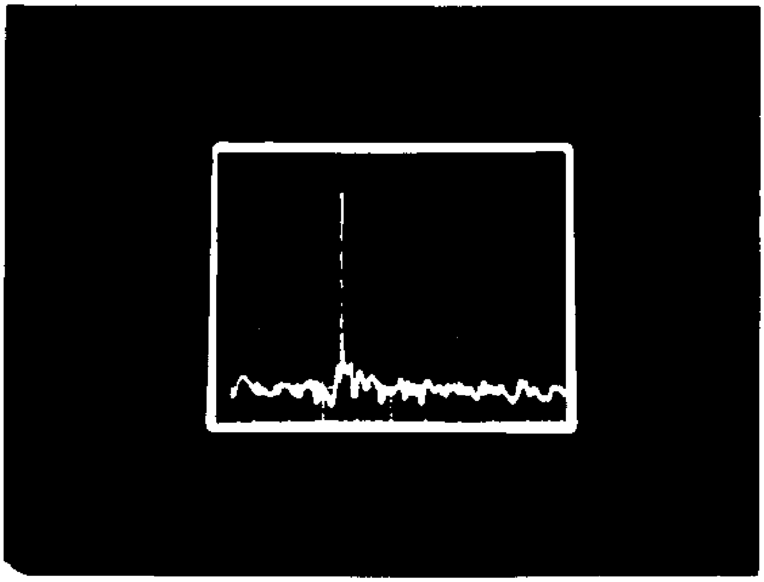

Fig. (2.4): Oscilloscope trace of a single laser pulse.